Electronic Supplementary Information for

Amino-Imidazolin-2-imine Cu(I) Complexes: Ligand Screening and Tuning of Photophysical Properties

Leo Wessel,[#a] Oliver Lange,[#b] Lars E. Burmeister,[b] Lars Denker,[a]
Michael Karnahl,[*b] Stefanie Tschierlei,[*b] Matthias Tamm,[*a] René Frank[*a]

AUTHOR ADDRESSES

[a] Institute of Inorganic and Analytical Chemistry, Technische Universität Braunschweig, Hagenring 30, 38106 Braunschweig, Germany
[b] Department of Energy Conversion, Institute of Physical and Theoretical Chemistry, Technische Universität Braunschweig, Rebenring 31, Braunschweig, Germany

* PD Dr. Michael Karnahl (michael.karnahl@tu-bs.de), Prof. Stefanie Tschierlei (s.tschierlei@tu-bs.de), Prof. Matthias Tamm (m.tamm@tu-bs.de), Dr. René Frank (r.frank@tu-bs.de).

Table of contents

1. General Information

All procedures were performed under argon atmosphere in a glove box (MBraun 200B) or using Schlenk techniques unless stated otherwise. Solvents were purified and dried using a Solvent Purification System (MBraun) and stored over sodium or potassium, except for halogenated solvents, which were stored over molecular sieves (3-4 Å). C_6D_6 and THF-D_8 were dried over sodium potassium alloy, filtered and stored under nitrogen. CD_2Cl_2 and $CDCl_3$ were dried over CaH_2, distilled and stored under nitrogen. All commercially available compounds (Sigma Aldrich, deutero, abcr, TCI) were used without further purification. The compounds S=C(N*i*PrCMe)$_2$, :C(N*i*PrCMe)$_2$[1], [Cl−C(N*i*PrCMe)$_2$][BF_4],[2] *N*-(2,6-diisopropylphenyl)-phenylene-1,2-diamine,[3] ligand HAmIm,[4] ligand **L4**, [5,6] ligand **L3**,[6] ligand **L2**[7] and ligand **L5**[6] were prepared according to literature methods.

Elemental analysis

Elemental analyses were accomplished by combustion and gas chromatographic analysis using a VarioMICRO Tube and HW detection. Values are reported in weight-%.

Nuclear magnetic resonance spectroscopy

NMR spectra were recorded on Bruker Avance III-HD-300, Avance III-400 and AVII-600 spectrometers. The chemical shifts (δ) are reported in parts per million (ppm). The residual solvents peak (C_6D_5H, δ = 7.16 ppm; C_7D_7H, δ = 7.00 ppm, THF-D_7H, δ = 3.58, 1.72 ppm; $CHCl_3$, δ = 7.16 ppm; $CDHCl_2$, δ = 5.32 ppm) is used for referencing of the ^1H spectra. The ^{13}C spectra are internally calibrated by using the ^{13}C resonances of the solvent peaks (C_6D_6, δ = 128.06 ppm; THF-D_8, δ = 67.21, 25.31 ppm; $CDCl_3$, δ = 77.16 ppm; CD_2Cl_2, δ = 53.84 ppm). Coupling constants are stated in Hertz (Hz), multiplicities are defined as broad (br), singlet (s), doublet (d), triplet (t), septet (sept), multiplet (m), doublet of doublets (dd), doublet of doublet of doublets (ddd) or triplet of doublets (td).

If necessary, 2D-NMR experiments (H,H COSY, H,C HSQC, HC HMBC, H,N HMBC) were used to aid the assignment of the signals.

Infrared absorption spectroscopy

FT-IR spectra were recorded on a Bruker Vertex 70 IR spectrometer. Samples were prepared in argon atmosphere in a glove box (MBraun 200B) as a 13 mm KBr pellet (0.2-1.4 weight%). The pellet was pressed with a 10 t press using a 13 mm Specac pellet die.

UV/vis absorption spectroscopy

UV/vis absorption spectra in inert tetrahydrofuran solution were recorded with an AvaLight-DH-S-BAL (Halogen and D_2) light source and a StarLine AvaSpec-ULS2048CL-EVO spectrometer (25 µm replaceable slit). Two fiber optic cables (Avantes FC-UVIR200-1-ME) outfitted with collimating lenses (Avantes COL-UV/VIS) were used to detect the transmission of light in 10 mm quartz cuvettes (Starna Spectrosil®). A full absorption spectrum was recorded every 10 s for 30 minutes unless otherwise denoted.

UV/vis absorption spectra of solid 13 mm KBr pellet samples (0.4-1.4 weight%) were recorded in diffuse reflectance mode with a JASCO V-770 spectrophotometer outfitted with a 60 mm UV-Visible/NIR integrating sphere and a ISN923 detector. A pure 13 mm KBr pellet (411.5 mg) was used as the baseline reference. The spectra were scanned in absorption mode from 2000 to 250 nm with a continuous scan speed of 200 nm/min, 1 data point per nanometre, a UV/vis bandwidth of 5 nm, a NIR bandwidth of 20 nm and a response time of 0.06 s.

Emission spectroscopy

Emission spectra of solid 13 mm KBr pellet samples (0.4-1.4 weight%) were recorded with a HORIBA Scientific FluoroMax Plus spectrofluorometer using the FluorEssence software. The pellets were placed between two rectangular quartz glass windows (Hellma® quartz glass high performance) and were set up with a 60° angle of incidence to the excitation light source to maximise the emission light and minimise excitation light reflection. The monochromator bandpass was set to 4 nm for all measurements. Integration times were left at 0.1 s with an increment of 1 data point per nm. Two measurements were averaged. Liquid samples were measured in transmission mode.

Time-resolved emission spectroscopy

Time-resolved emission spectra of solid samples as 13 mm KBr pellets (0.4-1.4 weight%) were recorded with a spectrograph (Kymera 328i-A) coupled to a streak camera (HAMAMATSU Universal Streak Camera C10910-01). The solid KBr sample pellet was held inbetween rectangular quartz glass windows (Hellma® quartz glass high performance). The excitation (λ = 400 nm, 550 nW, 550.0 pJ/pulse) was carried out in a 60° angle of incidence to the pulsed fs-laser beam of a Ti:Sapphire laser (Solstice ACE, Spectra Physics, 1 kHz, 70 fs) which is coupled to a TOPAS-PRIME-NIRUVis (Light Conversion) optical parametric amplifier. Two plano convex lenses (2”, f = 60mm) paired with a 420 nm longpass filter were used to collect and focus emission light into the spectrograph slit (500 µm) and block scattered laser light. The emission decay data was analysed in R *via* singular value decomposition and subsequently analysed *via* global lifetime analysis with an *n*-exponential function of the following form:

$$I(\lambda,t) = A_0 + \sum_{i=1}^{n} A_i e^{-\frac{t}{\tau_i}}$$

There is a background factor A_0 and n unique components with each component i having an amplitude A_i and lifetime τ_i.

Global lifetime analysis means that the amplitudes A_0 and A_i are locally fitted with a fixed parameter set of lifetimes τ_i that are the same across the fitted wavelengths. The fit has been constrained to only yield positive amplitudes. The residual sum of squares of the fits are stored in an n-dimensional array with one matrix per wavelength, indices correspond to the lifetime. Once all lifetime parameter sets are fitted to all wavelengths, the list of residual sum of squares arrays is flattened by forming the sum at every index resulting in a map of summed residual sum of squares value and the set with the lowest residual sum of squares is highlighted. The resulting decay-associated spectra are then generated by extracting the fitted amplitude parameters per wavelength of the lifetime combination with the lowest residual sum of squares. The decay-associated spectra show the spectral distribution of the lifetime, but are not contribution %. Those are obtained by calculating $A_i\tau_i/\Sigma A_i\tau_i$. The peak wavelengths of the decay-associated spectra were obtained through Gaussian fits.

The temperature-dependent measurements of **9** with 400 nm fs-laser pulses (550 nW, ~550 pJ/pulse) were carried out with the same setup described above using an Oxford Instruments Optistat DN-X cryostat with an Oxford Instruments MercuryiTC temperature controller. Liquid Nitrogen was used as the cryogen gas and helium as the exchange gas. The KBr pellet was placed in the cryostats sample holder and rotated to a 60° angle of incidence to the 400 nm pulsed fs-laser. The fit model above was directly applied.

Electrochemistry

Cyclic voltammetry was performed utilising an Autolab potentiostat PGSTAT204 from Metrohm with a three-electrode configuration consisting of a glassy carbon disc ($\varnothing = 3$ mm) as the working electrode, a platinum wire as the counter electrode and a non-aqueous Ag/Ag^+ reference electrode. All measurements were acquired in inert tetrahydrofuran solution containing $[Bu_4N][PF_6]$ (0.1 M) as the supporting electrolyte. The scan rate was set to 100 mV/s unless otherwise stated. All data are referenced against the ferrocene/ferrocenium (Fc/Fc^+) couple, by adding ferrocene to the solution after each measurement. For each measurement two reduction-oxidation-cycles were recorded and the second one is shown.

Computational Details

Density functional theory (DFT) and time-dependent DFT (TDDFT) computations were carried out in ORCA (version 5.0.4) parallelised with OpenMPI (version 4.1.1).[8] The PBE0 hybrid functional was used together with the def2-TZVP basis set.[9,10] Dispersion effects were accounted for by applying the D3BJ correction.[11,12] Furthermore, the RIJCOSX approximation was applied with the respective auxiliary def2/J basis set.[13–17] Tetrahydrofuran was implicitly implemented *via* the CPCM model.[18] SCF convergence criteria were set to 'TightSCF'.

Crystal structures served as the initial structure guess and were optimised. A subsequent analytical frequency computation on the same theoretical level showed no imaginary modes for **4**-**10**. Molecular orbitals (MOs) were acquired in a single-point energy run. 150 excitation energies were considered within the Tamm-Dancoff-approximated TDDFT (TDA-TDDFT).[19,20]

The orca_mapspc program was used to generate excitation spectra with Gaussians (FWHM = 3500 cm^{-1}). The excitation spectra were then plotted using the program language R. ChimeraX with the SEQCROW plugin was used to render MOs with a resolution of 0.15 Å and an isosurface of ±0.035 in blue (-) and red (+).[21–25] The difference density plots (ddps) were first generated as cube files in the orca_plot program with a resolution of Ngrid = 150 and subsequently plotted in ChimeraX (+SEQCROW) with an isosurface of ±0.001 in gray (-) and green (+).

2. Syntheses

2.1 Compound **1** - [Cu(HAmIm)Cl]

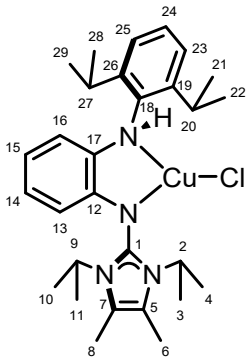

Copper(I)-chloride (0.57 g, 5.82 mmol, 1.0 eq.) and HAmIm ligand **C** (2.60 g, 5.82 mmol, 1.0 eq.) were suspended in THF (50 mL) and stirred for 3 h at 10 °C, forming a white precipitate. The reaction mixture was filtered, and the residue was washed with *n*-hexane (2 × 10 mL) and dried *in vacuo*. The residue was dissolved in toluene (60 mL) and stored at −40 °C to afford the product (2.83 g, 5.19 mmol, 89 %) as white crystals suitable for X-ray crystallography.

^{1}H NMR (400 MHz, CD_2Cl_2): δ (ppm) = 7.25-7.19 (m, 3 H, C23─*H*, C24─*H*, C25─*H*), 6.63 (td, *J* = 7.6, 1.5 Hz, 1 H, C14─*H*), 6.52 (td, *J* = 7.6, 1.4 Hz, 1 H, C15─*H*), 6.27 (dd, *J* = 7.8, 1.1 Hz, 1 H, C16─*H*), 6.09 (dd, *J* = 7.8, 1.1 Hz, 1 H, C13─*H*), 5.70 (s, 1 H, N─*H*), 4.97 (sept, *J* = 7.1 Hz, 2 H, NC*H*$(CH_3)_2$), 3.21 (sept, *J* = 6.9 Hz, 2 H, C*H*$(CH_3)_2$), 2.28 (s, 6 H, CH_3), 1.47 (d, *J* = 7.1 Hz, 12 H, CH(C$H_3)_2$), 1.26 (d, *J* = 6.8 Hz, 6 H, C4─H_3, C3─H_3), 1.08 (d, *J* = 6.8 Hz, 6 H, C10─H_3, C11─H_3).

^{13}C{^{1}H} NMR (101 MHz, CD_2Cl_2): δ (ppm) = 150.4 (s, *C*1), 145.1 (s, *C*19, *C*26), 143.43(s, *C*18), 137.9 (s, *C*12), 137.5 (s, *C*17), 126.0 (s, *C*24), 124.2 (s, *C*23, C*25*), 121.3 (s, *C*14), 119.0 (s, *C*15), 117.8 (s, *C*16), 117.1 (s, *C*13), 48.9 (s, N*C*H$(CH_3)_2$), 28.8 (s, *C*H$(CH_3)_2$), 25.1 (s, CH(*C*$H_3)_2$), 23.4 (s, *C*10, *C*11), 21.4 (s, *C*3, *C*4), 10.4 (s, *C*7, *C*8).

Elemental Analysis: Calcd. for $C_{29}H_{42}ClCuN_4$: C 63.83, H 7.76, N 10.27.
Found: C 63.78, H 7.68, N 10.14.

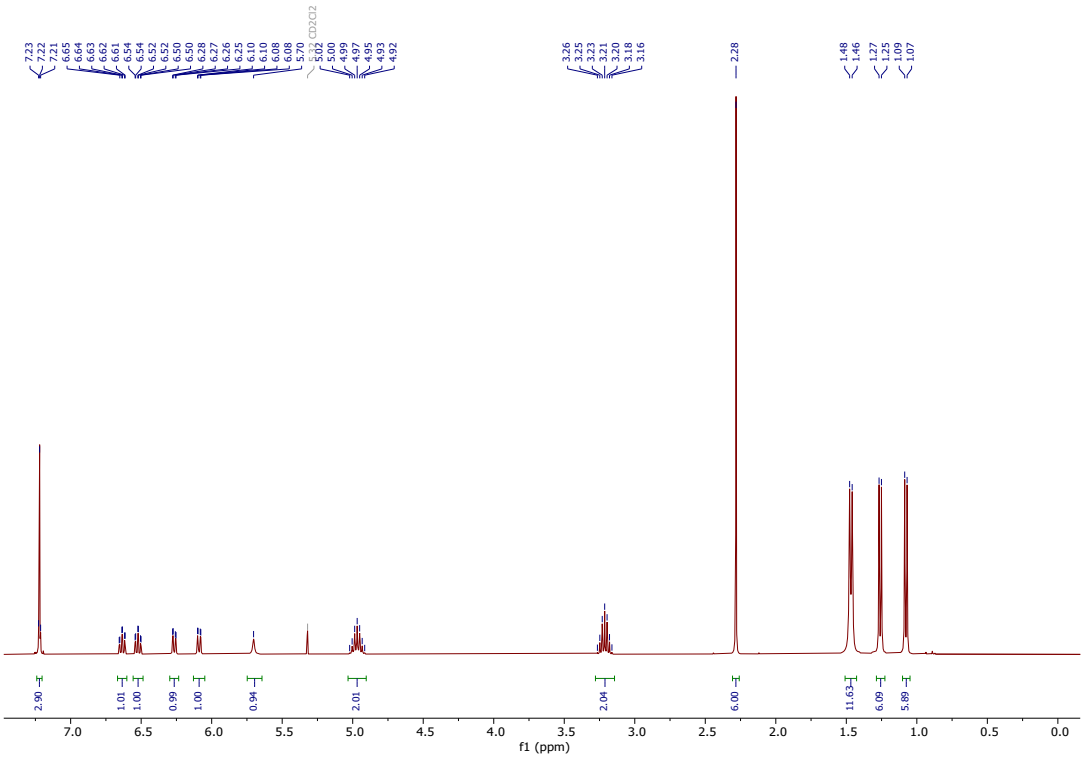

Figure S1: ^{1}H NMR spectrum of compound **1**, (400 MHz, CD_2Cl_2).

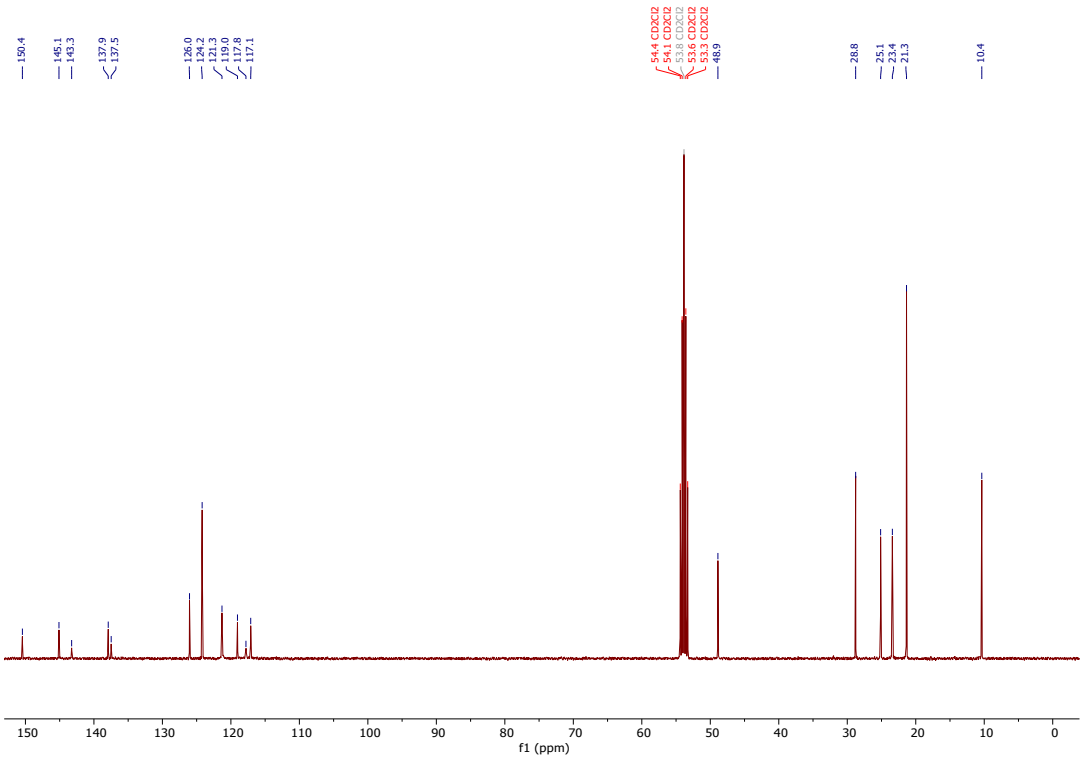

Figure S2: $^{13}C\{^{1}H\}$ NMR spectrum of compound **1**, (101 MHz, CD_2Cl_2).

2.2 Compound **2** - $[Cu_2(\mu\text{-AmIm})_2]$

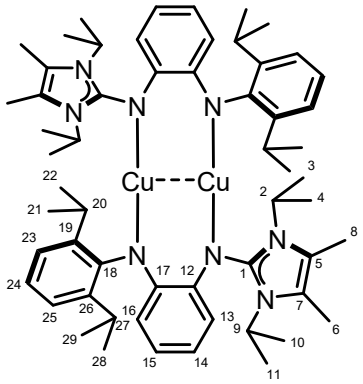

Compound **1** (0.90 g, 1.65 mmol, 1.0 eq.) and KHMDS (0.33 g, 1.65 mmol, 1.0 eq.) were dissolved in THF (50 mL) and stirred for 30 h at 10 °C. The solution was filtered over Celite® and the solvent was evaporated. The crude product was washed with *n*-hexane (2 × 100 mL) and dried *in vacuo*. The residue was dissolved in benzene (10 mL) and layered with *n*-pentane (30 mL). The product (0.72 g, 1.45 mmol, 88 %) was obtained as colorless crystals suitable for X-ray crystallography.

^{1}H NMR (400 MHz, THF-D8): δ (ppm) = 7.17-7.15 (m, 3 H, C23─*H*, C24─*H*, C25─*H*), 6.46 (dd, *J* = 7.6, 1.5 Hz, 1 H, C13─*H*), 6.37-6.35 (m, 1 H, C14─*H*), 6.30 (td, *J* = 7.5, 1.6 Hz, 1 H, C15─*H*), 5.94 (dd, *J* = 7.0, 1.9 Hz, 1 H, C16─*H*), 4.55 (sept, *J* = 7.0 Hz, 2 H, NC*H*$(CH_3)_2$), 3.32 (sept, *J* = 6.9 Hz, 2 H, C*H*$(CH_3)_2$), 2.12 (s, 6 H, C*H*$_3$), 1.36 (d, *J* = 6.9 Hz, 12 H, NCH(C*H*$_3)_2$), 1.13 (d, *J* = 6.9 Hz, 12 H, CH(C*H*$_3)_2$).

^{13}C{^{1}H} NMR (101 MHz, THF-D8): δ (ppm) = 150.7 (s, *C*1), 148.3 (s, *C*19, *C*26), 141.2 (s, *C*12), 140.2 (s, *C*17), 139.3 (s, *C*18), 127.1 (s, *C*24), 124.2 (s, *C*23, *C*25), 118.1 (s, *C*5, *C*7), 117.9 (s, *C*14), 117.8 (s, *C*15), 116.0 (s, *C*13), 110.4 (s, *C*16), 47.5 (s, N*C*H$(CH_3)_2$), 29.2 (s, *C*H$(CH_3)_2$), 26.0, 25.8, 25.6, 25.4 (br, *C*21, *C*22, *C*28, *C*29) 21.2 (s. NCH(*C*H$_3)_2$), 10.5 (s, *C*7, *C*8).

Elemental Analysis: Calcd. for $C_{29}H_{41}CuN_4$: C 68.40, H 8.12, N 11.00.
Found: C 68.23, H 9.09, N 10.80.

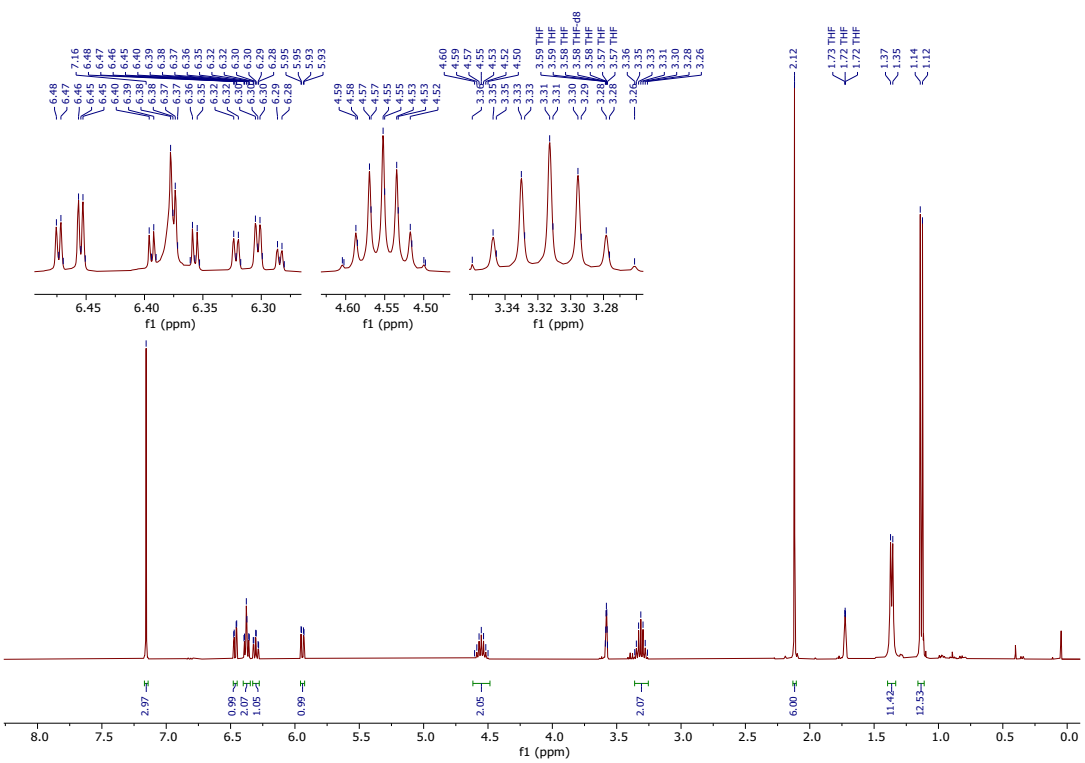

Figure S3: ^{1}H NMR spectrum of compound **2**, (400 MHz, THF-D8).

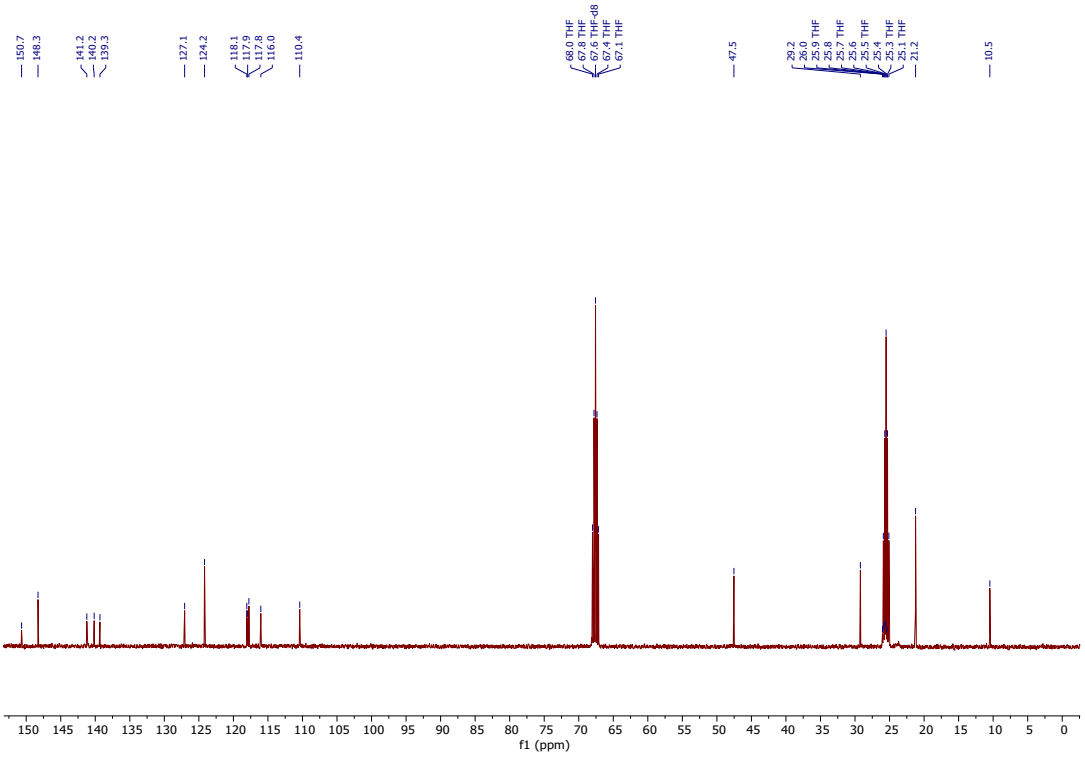

Figure S4: $^{13}C\{^{1}H\}$ spectrum of compound **2**, (101 MHz, THF-D8).

2.3 Compound **3** - $[Cu_2(AmIm)_2(\mu\text{-}OH)_2]$

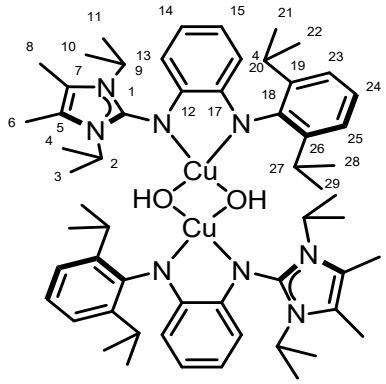

Compound **2** (150 mg, 0.10 mmol, 0.5 eq.) was dissolved in THF (10 mL). A solution of THF (10 mL) with water (micro syringe, 3.64 mg, 0.20 mmol, 3.65 µL, 1.0 eq.) was added. The solution was stirred overnight. All volatile components were removed *in vacuo*. The crude product was dissolved in benzene (5 mL) and then layered with *n*-hexane (50 mL), which afforded the product (72 mg, 0.14 mmol, 68 %) as dark red crystals suitable for X-ray crystallography.

^{1}H NMR (300 MHz, THF-D8) δ (ppm) = 7.16 (s, 3 H, C23—*H*, C24—*H*, C25—*H*), 6.46 (dd, *J* = 7.5, 1.3 Hz, 1 H, C14—*H*), 6.38 (s, 1 H, O*H*), 6.37 (td, 1 H, C15—*H*), 6.31 (td, 1 H, C16—*H*), 5.94 (dd, *J* = 7.5, 1.2 Hz, 1 H, C13—*H*), 4.55 (sept, *J* = 6.9 Hz, 2 H, NC*H*$(CH_3)_2$), 3.31 (sept, *J* = 6.8 Hz, 2 H, C*H*$(CH_3)_2$), 2.12 (s, 6 H, CH_3), 1.36 (d, *J* = 6.9 Hz, 12 H, NCH(C$H_3)_2$), 1.13 (d, *J* = 6.9 Hz, 12 H, CH(C$H_3)_2$).

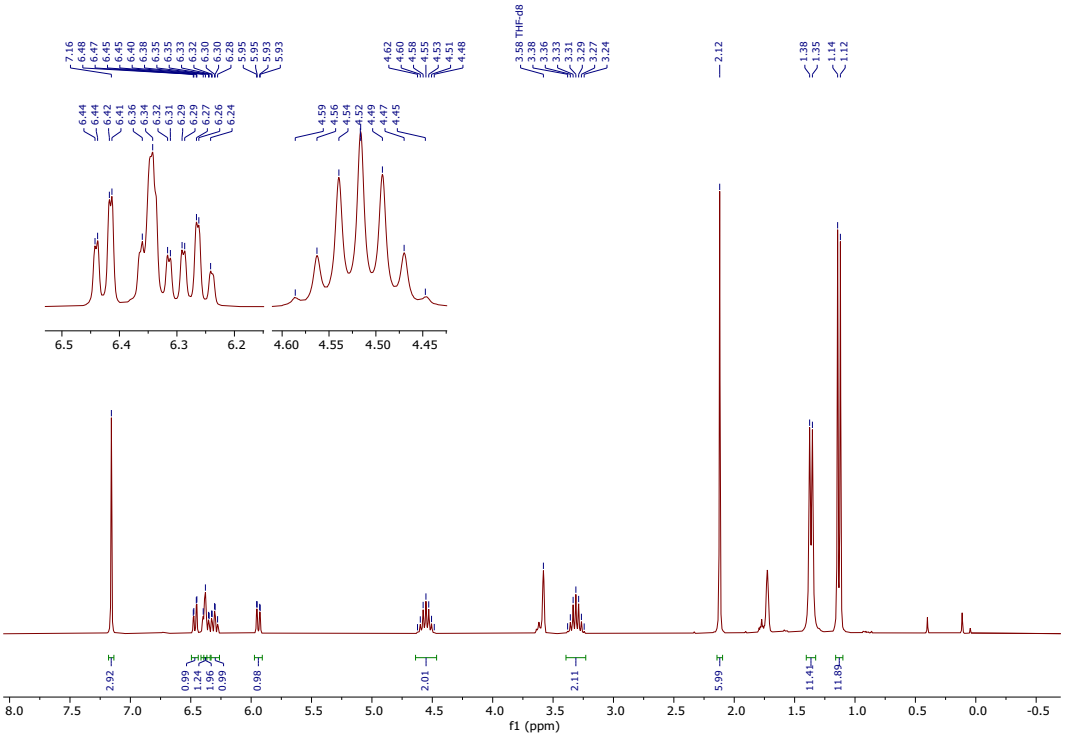

Figure S5: ^{1}H NMR spectrum of compound **3**, (300 MHz, THF-D8).

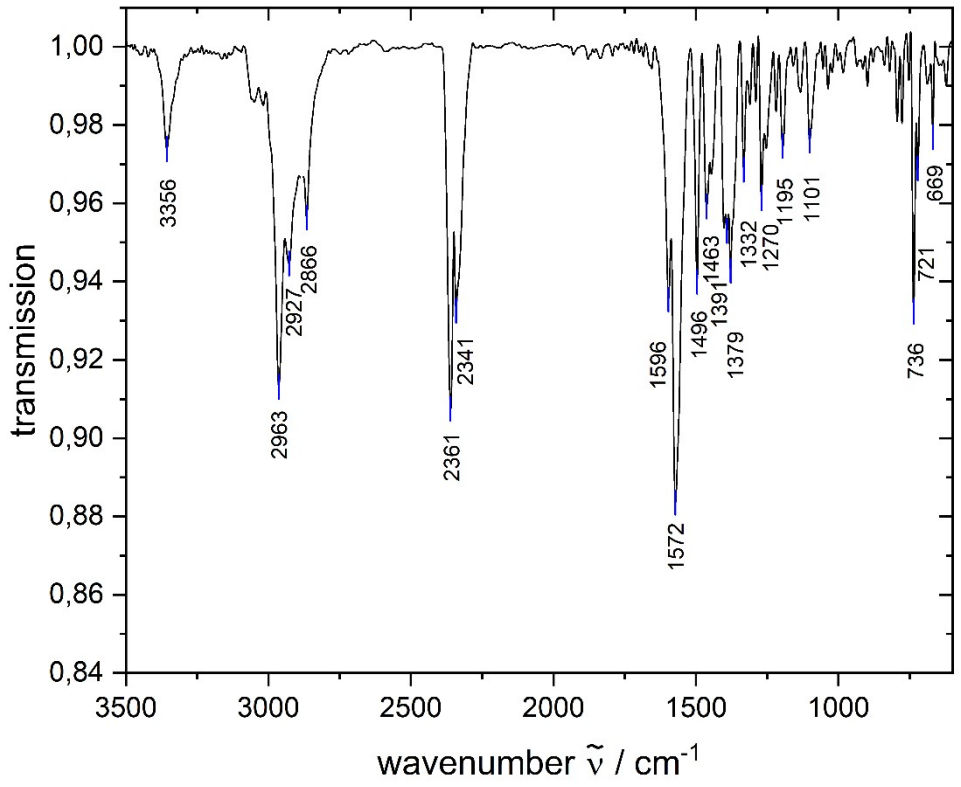

Figure S6: FTIR spectrum of compound **3**.[26]

$\tilde{\nu}$

2.4 Compound **4** - [Cu(AmIm)(phen)]

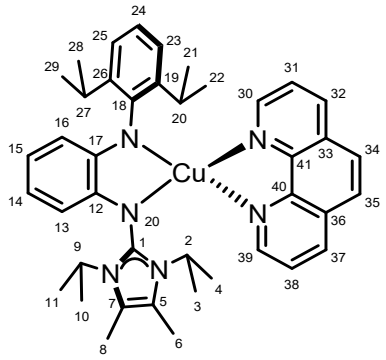

Compound **2** (150 mg, 0.15 mmol, 0.5 eq.) and dried 1,10-phenanthroline (phen, 55 mg, 0.30 mmol, 1.0 eq.) were dissolved in THF (10 mL) and stirred for 48 h at 10 °C. The solvent was removed *in vacuo* and the residue was dissolved in toluene (5 mL). Layering with *n*-pentane (40 mL) afforded the product (132 mg, 0.19 mmol, 63 %) as intensive green crystals, which were suitable for X-ray crystallography.

^{1}H NMR (400 MHz, THF-D8): *δ* (ppm) = 9.31 (d, *J* = 3.9 Hz, 2 H, C30–*H*, C39–*H*), 8.39 (dd, *J* = 7.9, 1.1 Hz, 2 H, C32–*H*, C37-*H*), 7.86 – 7.82 (m, 3 H, C23–*H*, C24–*H*, C25–*H*), 7.79 (dd, *J* = 7.9, 4.8 Hz, 2 H, C31–*H*, C38–*H*), 6.82 (d, *J* = 7.1 Hz, 2 H, C34–*H*, C35–*H*), 6.59 (t, *J* = 7.5 Hz, 1 H, C14–*H*), 6.28 – 6.18 (m, 2 H, C13–*H*, C15–*H*), 5.69 – 5.41 (br, 1H, C16–*H*), 4.96 (sept, *J* = 7.1 Hz, 2 H, NC*H*$(CH_3)_2$), 4.10 (sept, J = 6.9 Hz, 2 H, C*H*$(CH_3)_2$), 1.99 (s, 6 H, CH_3), 1.17 (d, *J* = 7.0 Hz, 6 H, CH(C$H_3)_2$), 1.10 (d, *J* = 6.9 Hz, 6 H, CH(C$H_3)_2$), 0.84 (d, *J* = 6.9 Hz, 6 H, NCH(C$H_3)_2$), 0.67 (d, J = 7.1 Hz, 6 H, NCH(C$H_3)_2$).

^{13}C{^{1}H} NMR (101 MHz, THF-D8): *δ* (ppm) = 150.7 (s, *C*1), 148.3 (s, *C*30*, C*39), 148.2 (s, *C*41, *C*40), 144.5 (s, *C*33, *C*36), 134.4 (s, *C*32, *C*37), 130.3 (s, *C*19, *C*26), 129.8 (s, *C*18), 129.1 (s, *C*12, *C*17), 127.5 (s, *C*23, *C*24, *C*25), 125.8 (s, *C*31, *C*38), 123.2 (s, *C*16), 120.7 (s, *C*14, *C*15), 118.5 (s, *C*5, C7), 117.6 (s, C13), 47.5 (s, N*C*H$(CH_3)_2$), 27.9 (s, *C*H$(CH_3)_2$), 26.0, 25.8, 25.6, 25.4 (s, *C*21, *C*22, *C*28, *C*29), 21.9 (s, NCH(*C*$H_3)_2$), 10.4 (s, *C*6, *C*8).

Elemental Analysis: Calcd. for $C_{41}H_{50}CuN_6$: C 71.32, H 7.30, N 12.17.
Found: C 70.48, H 7.33, N 12.11.

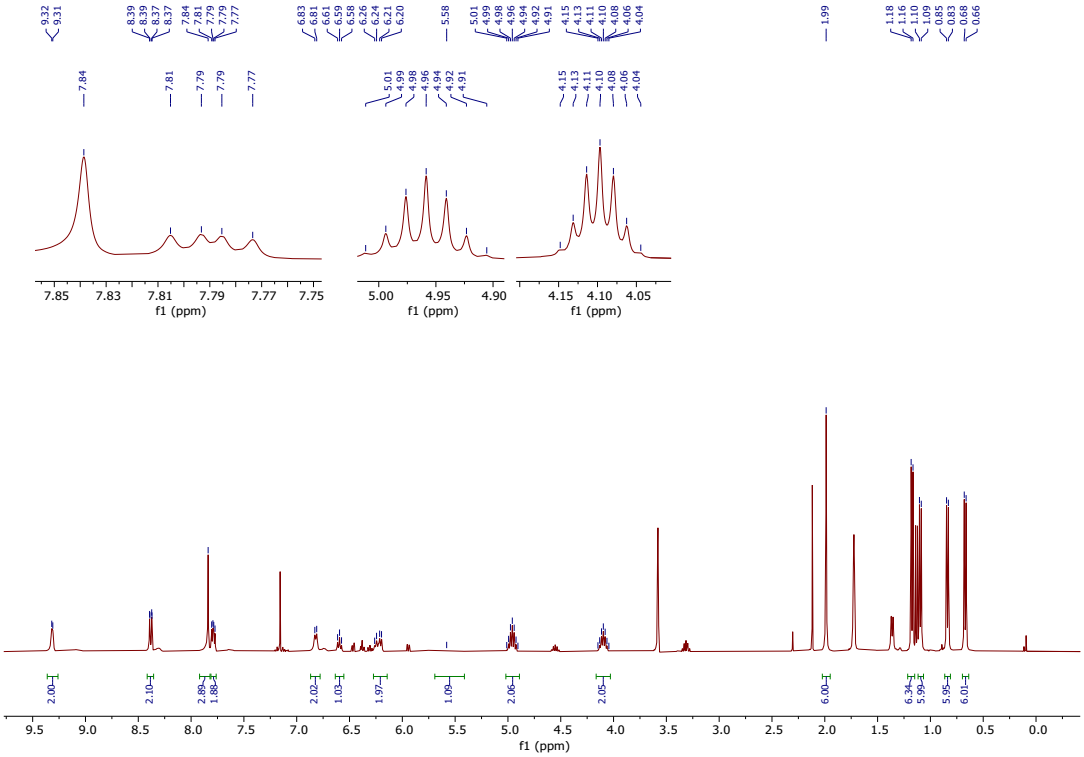

Figure S7: ^{1}H NMR spectrum of compound **4**, (400 MHz, THF-D8).

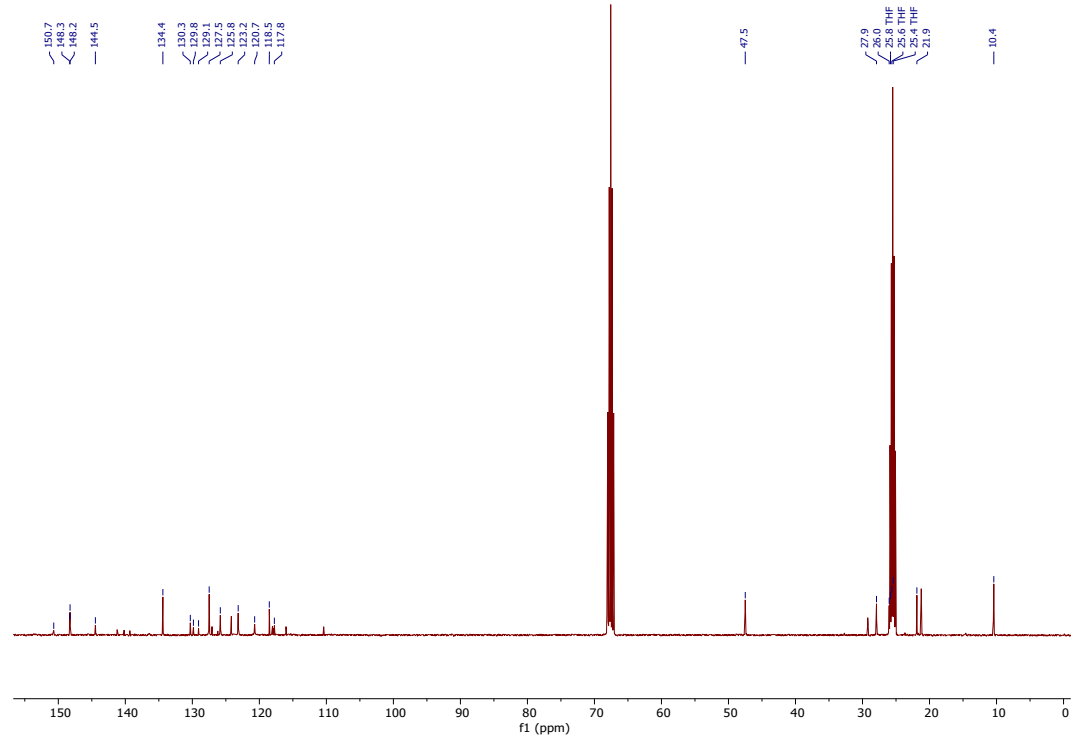

Figure S8: $^{13}C\{^{1}H\}$ NMR spectrum of compound **4**, (101 MHz, THF-D8).

2.5 Compound **5** - [Cu(AmIm)(neo)]

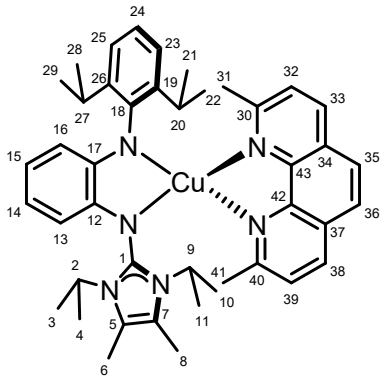

Compound **2** (100 mg, 0.10 mmol, 0.5 eq.) and dried neocuproine (42 mg, 0.20 mmol, 1.0 eq.) were dissolved in THF (10 mL) and stirred for 48 h at 10 °C. The solvent was removed *in vacuo* and the residue was dissolved in toluene (5 mL). Layering with *n*-pentane (40 mL) afforded the product (90 mg, 0.125 mmol, 62 %) as green to blue crystals, which were suitable for X-ray crystallography.

^{1}H NMR (500 MHz, THF-D8) δ (ppm) = 8.29 (d, *J* = 8.1 Hz, 2 H, C33–*H,* C38–*H*), 7.79 (s, 2 H, C35–*H,* C36–*H*), 7.66 (d, *J* = 8.2 Hz, 2 H, C32–*H,* C39–*H*), 6.76 (d, *J* = 7.5 Hz, 2 H, C23–*H,* C25–*H*), 6.60 (t, *J* = 7.5 Hz, 1 H, C24–*H*), 6.38 (d, *J* = 1.6 Hz, 1 H, C16–*H*), 6.26 (ddd, *J* = 7.8, 7.3, 1.6 Hz, 1 H, C14–*H*), 5.83 (td, *J* = 7.3, 1.5 Hz, 1 H, C15–*H*), 5.58 (dd, *J* = 7.9, 1.5 Hz, 1 H, C13–*H*), 5.01 (sept, *J* = 7.1 Hz, 2 H, NC*H*$(CH_3)_2$), 3.86 (sept, *J* = 6.9 Hz, 2 H, C*H*$(CH_3)_2$), 2.92 (s, 6 H, C31–H_3, C41–H_3), 2.03 (s, 6 H, C6–H_3, C8–H_3), 1.09 (d, *J* = 7.0 Hz, 6 H, CH$(CH_3)_2$), 0.97 (d, *J* = 6.9 Hz, 6 H), 0.64 (d, *J* = 7.1 Hz, 6 H, NCH$(CH_3)_2$), 0.49 (d, *J* = 7.0 Hz, 6 H, NCH$(CH_3)_2$).

^{13}C{^{1}H} NMR (126 MHz, THF-D8): δ (ppm) = 157.9 (s, *C*30, *C*40), 155.1 (s, *C*12), 154.1 (s, *C*18), 152.6 (s, *C*1) 145.4 (s, *C*19, *C*26), 144.0 (s, *C*42, *C*43), 142.1 (s, *C*17), 134.9 (s, *C*33, *C*38), 128.2 (s, *C*5, *C*7), 126.3 (s, *C*35, *C*36), 125.8 (s, *C*32, *C*39), 123.4 (s, *C*24), 121.2 (s, *C*14), 120.7 (s, *C*23, *C*25), 118.2 (s, *C*34, *C*37), 116.2 (s, *C*16), 110.7 (s, *C*13), 108.0 (s, *C*15), 47.2 (s, N*C*H$(CH_3)_2$), 32.7 (s, *C*H_3 neo), 27.6 (s, *C*H_3 neo), 26.7, 25.5, 24.5, 23.7 (s, *C*21, *C*22, *C*28, *C*29), 21.5 (s, NCH(*C*$H_3)_2$), 21.3 (s, NCH(*C*$H_3)_2$), 10.6 (s, *C*6, *C*8).

Elemental Analysis: Calculated for $C_{43}H_{54}CuN_6$: C 71.88, H 7.58, N 11.70. Found: C 67.27, H 7.05, N 10.43.

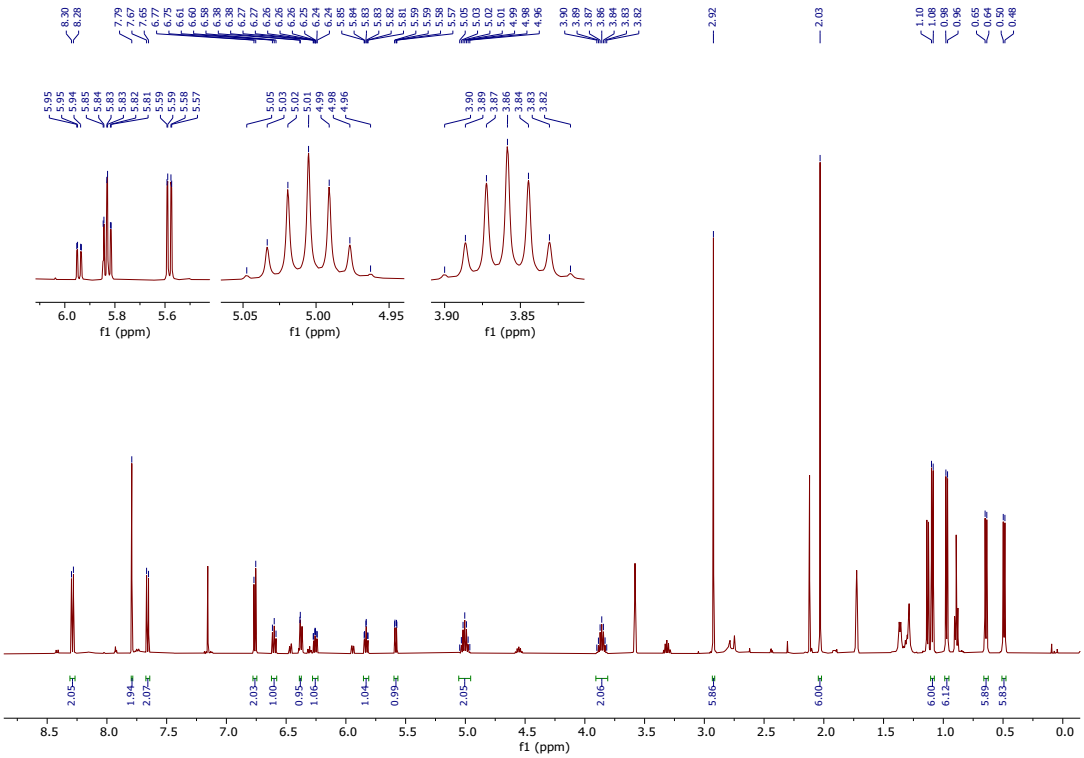

Figure S9: ^{1}H NMR spectrum of compound **5**, (500 MHz, THF-D8).

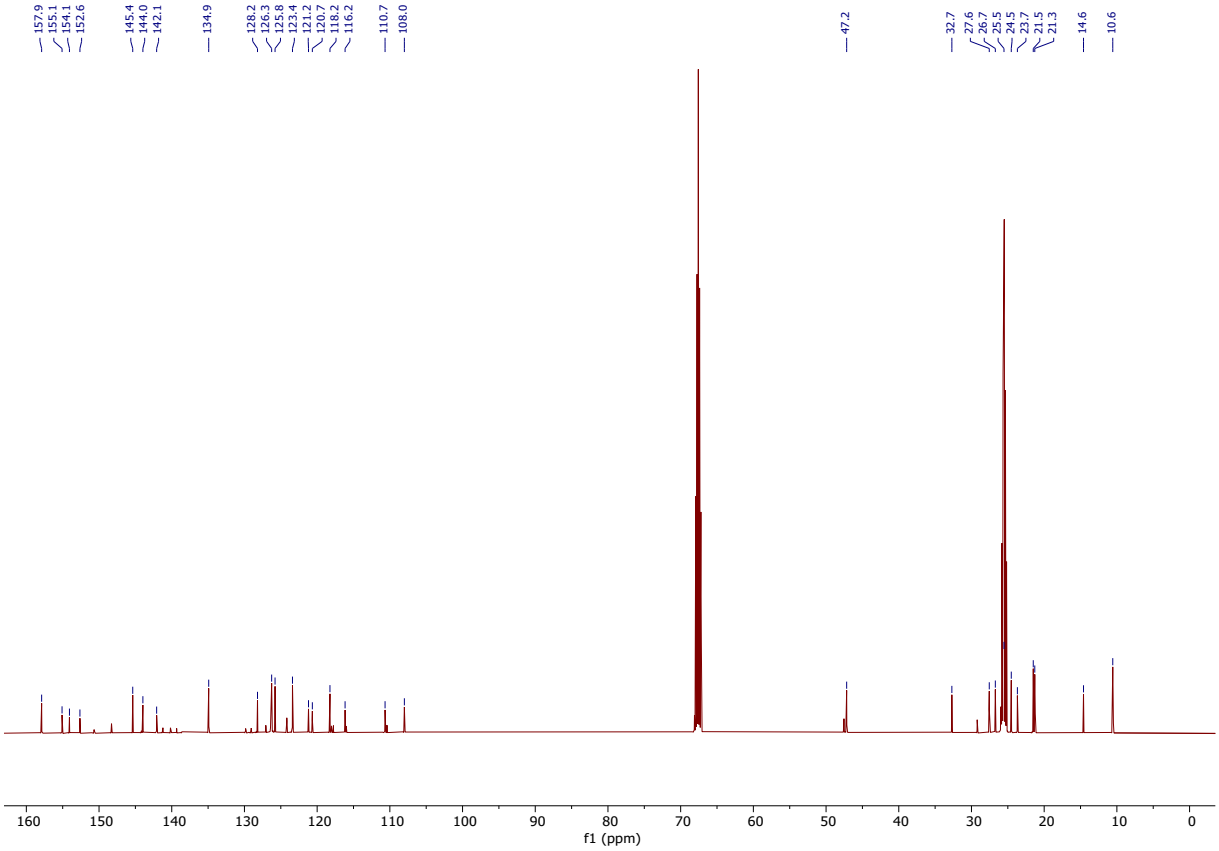

Figure S10: ^{13}C{^{1}H} NMR spectrum of compound **5**, (126 MHz, THF-D8).

2.6 Ligand **L2**

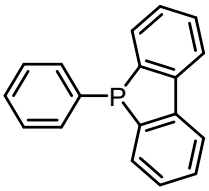

The procedure is based on literature known preparations.[7] 2,2'-dibromo-1,1'-biphenyl (1.50 g, 4.81 mmol, 1.0 eq.) was dissolved in THF (20 mL) and cooled down to −78 °C and *n-BuLi* (6.00 mL, 39.60 mmol, 1.6 M in hexanes, 2.0 eq.) was added within 30 min with stirring and formation of a white precipitate. The mixture was allowed to warm to room temperature and stirred overnight. Dichlorophenylphosphine (0.86 g, 0.65 mL 4.79 mmol, 1.0 eq.) was added at room temperature with complete dissolution. All volatile components were removed *in vacuo*. The crude product was purified by column chromatography using a mixture of DCM and *n*-hexane (1:3, v/v). The product was obtained as a white solid (160 mg, 0.61 mmol, 13 %).

^{1}H NMR (300 MHz, C_6D_6) δ(ppm) = 7.42-7.34 (m, 2 H, aryl C*H*), 7.28-7.20 (m, 2 H, aryl-C*H*), 7.08-6.99 (m, 2 H, aryl-C*H*), 6.86 (td, *J* = 7.6, 1.3 Hz, 2 H, aryl-C*H*), 6.72 (tdd, *J* = 7.4, 2.8, 1.1 Hz, 2 H, aryl-C*H*), 6.64-6.53 (m, 3 H, m-*H*, p-*H* in C_6H_5).

^{31}P{^{1}H} NMR (121 MHz, C_6D_6) δ(ppm) = −10.12.

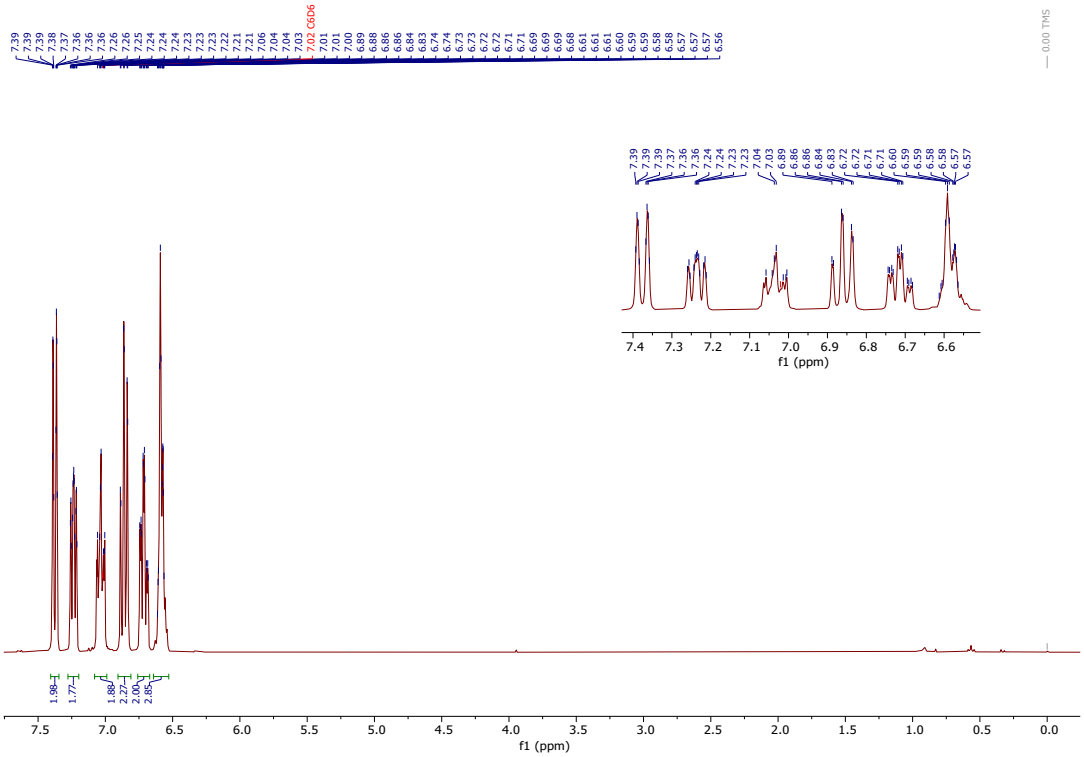

Figure S11: ^{1}H NMR spectrum of ligand **L2**, (300 MHz, C_6D_6).

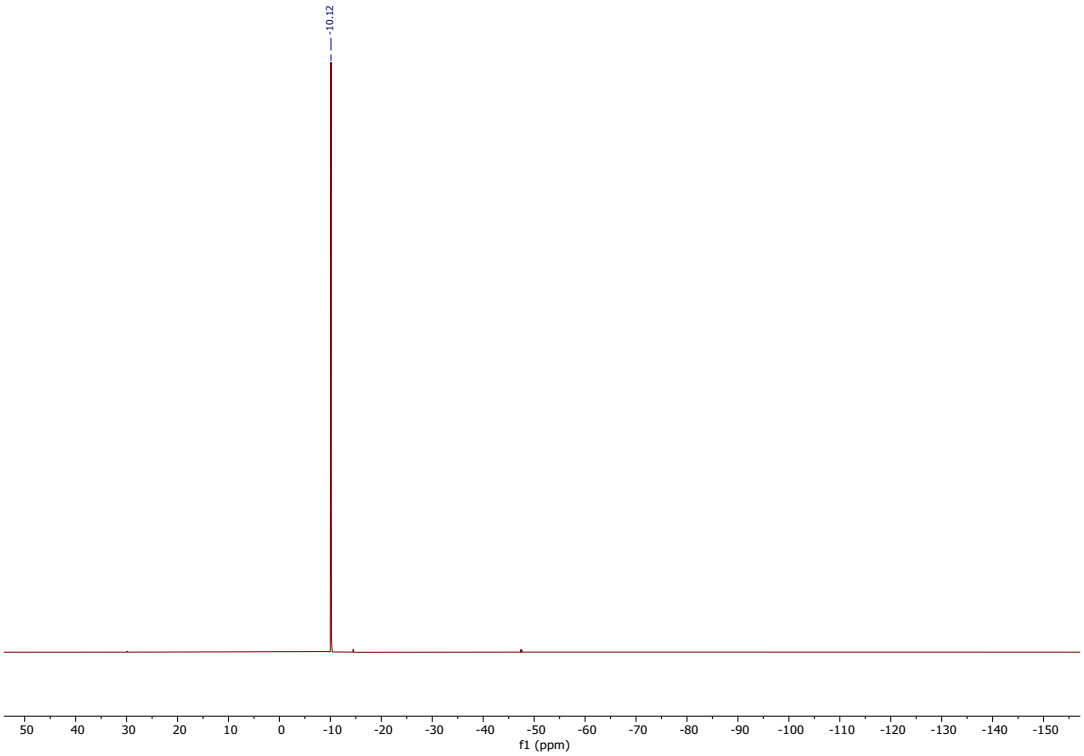

Figure S12: $^{31}P\{^{1}H\}$ NMR spectrum of ligand **L2**, (121 MHz, C_6D_6).

2.7 Ligand **L3**

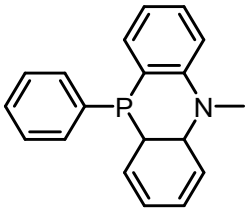

The procedure is based on literature known preparations.[6] *N*-methyl-*N*-phenylaniline (1.05 g, 1.00 mL, 5.73 mmol, 1.0 eq.), *n*-BuLi (7.30 mL, 11.75 mmol in 1.6 M in hexanes, 2.05 eq.) and TMEDA (1.77 mL, 1.36 g, 11.75 mmol, 2.05 eq.) were dissolved in *n*-hexane (5 mL) and heated to 68 °C for 6 h with formation of an orange solution accompanied with a white precipitate. The precipitate was filtered, dried *in vacuo* and dissolved in THF (15 mL). Dichlorophenylphosphine (0.80 mL, 1.06 g, 5.90 mmol, 1.03 Äq.) was added at room temperature. The mixture was stirred for 2 h, dried *in vacuo* and extracted with diethyl ether (50 mL) and water (50 mL). The crude product was purified by column chromatography using a mixture of DCM and hexane (1:3, v/v). The product was obtained as a white solid (130 mg, 0.46 mmol, 8 %).

^{1}H NMR (300 MHz, $CDCl_3$) δ(ppm) = 7.70 (ddd, *J* = 11.7, 7.3, 1.7 Hz, 2 H, aryl-C*H*), 7.43 (ddd, *J* = 8.5, 7.3, 1.7 Hz, 2 H, aryl-C*H*), 7.15-7.07 (m, 5 H, -C_6H_5), 7.05 (d, *J* = 8.3 Hz, 2 H, aryl-C*H*), 7.01-6.93 (m, 2 H, aryl-C*H*), 3.41 (s, 3 H, NCH_3).

^{31}P{^{1}H} NMR (121 MHz, $CDCl_3$) δ(ppm) = −44.84.

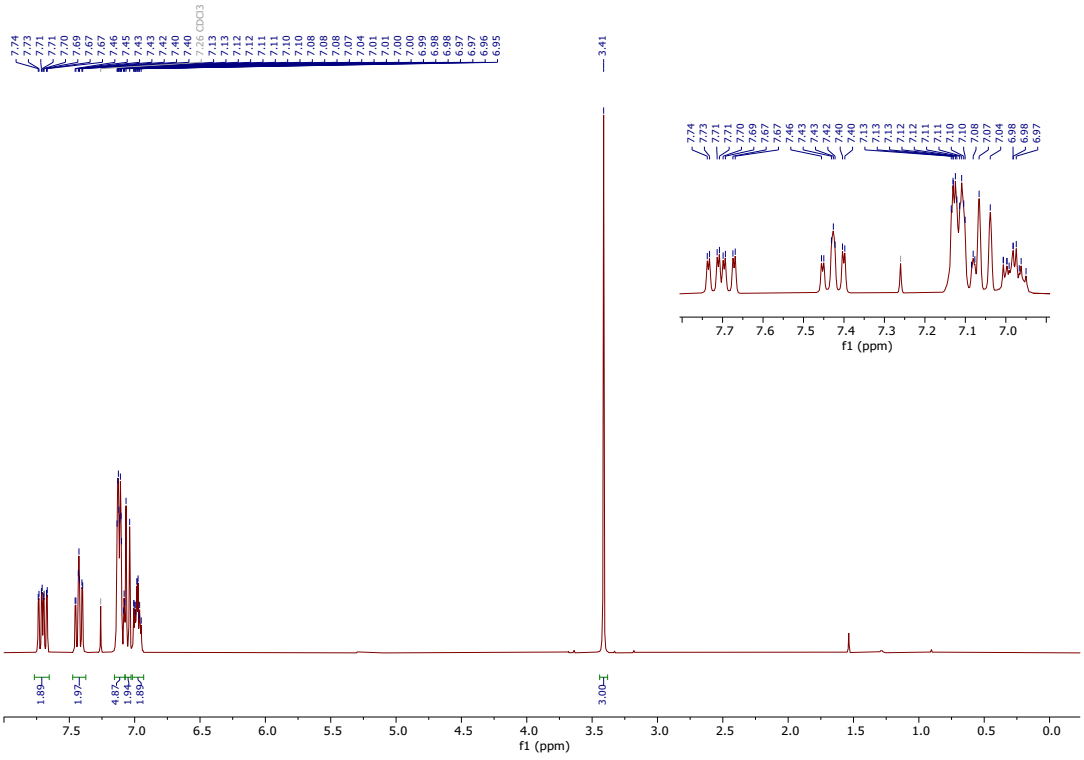

Figure S13: ^{1}H NMR spectrum of ligand **L3**, (300 MHz, $CDCl_3$).

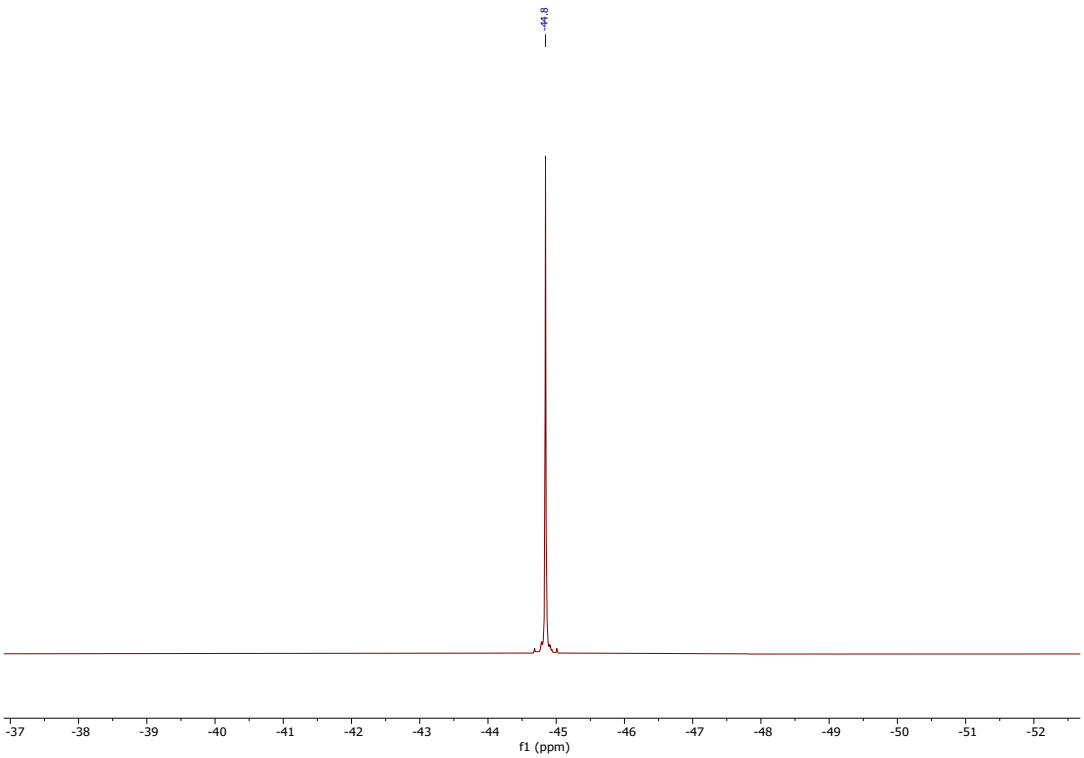

Figure S14: $^{31}P\{^{1}H\}$ NMR spectrum of ligand **L3**, (121 MHz, $CDCl_3$).

2.8 Ligand **L4**

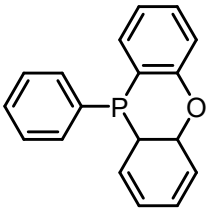

The procedure is based on literature known preparations.[5,6] Diphenyl ether (3.00 mL, 3.21 g, 18.86 mmol, 1.0 eq.) was solved in THF (20 mL) and stored at −40 °C overnight. The solution was removed from the refrigerator and *n*-BuLi (24.75 mL, 39.60 mmol, 1.6 M in hexanes, 2.0 eq.) was added over a 10 min period while stirring. The resulting orange solution was allowed to warm to room temperature and stirred overnight. An off-white solid formed was filtered, washed with cold *n*-hexane and dried *in vacuo*. The solid material was assumed to be 2,2´-dilithiodiphenylether and used in manipulations without further analysis. A portion of the solid (2,2´-dilithiodiphenylether, 2.50 g, 13.73 mmol, 1.0 eq.) was dissolved in THF (20 mL), and dichlorophenylphosphine (2.46 g, 1.86 mL, 13.73 mmol, 1.0 eq.) was added at 0 °C. The mixture was allowed to warm to room temperature and stirred for 1 h. All volatile components were removed *in vacuo*. The crude product was purified by column chromatography using a mixture of DCM and *n*-hexane (1:3, v/v). The product was obtained as a white solid (120 mg, 0.43 mmol, 3 %).

^{1}H NMR (300 MHz, $CDCl_3$) δ (ppm) = 7.55 (ddd, *J* = 10.4, 7.5, 1.7 Hz, 2 H, aryl-C*H*), 7.40 (ddd, *J* = 8.4, 7.2, 1.7 Hz, 2 H, aryl-C*H*), 7.28- 7.19 (m, 7 H, aryl-C*H*), 7.15 (tt, *J* = 7.4, 1.4 Hz, 2 H, aryl-C*H*).

^{31}P{^{1}H} NMR (121 MHz, $CDCl_3$) δ (ppm) = −53.85.

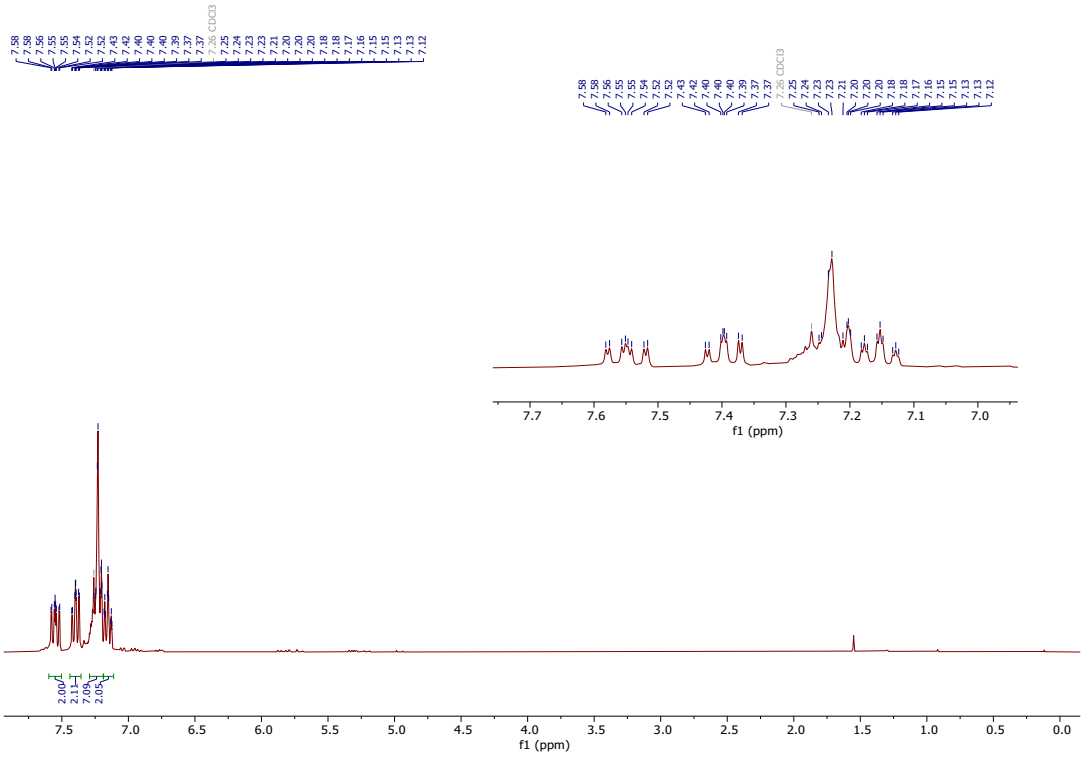

Figure S15: ^{1}H NMR spectrum of compound **L4**, (300 MHz, $CDCl_3$).

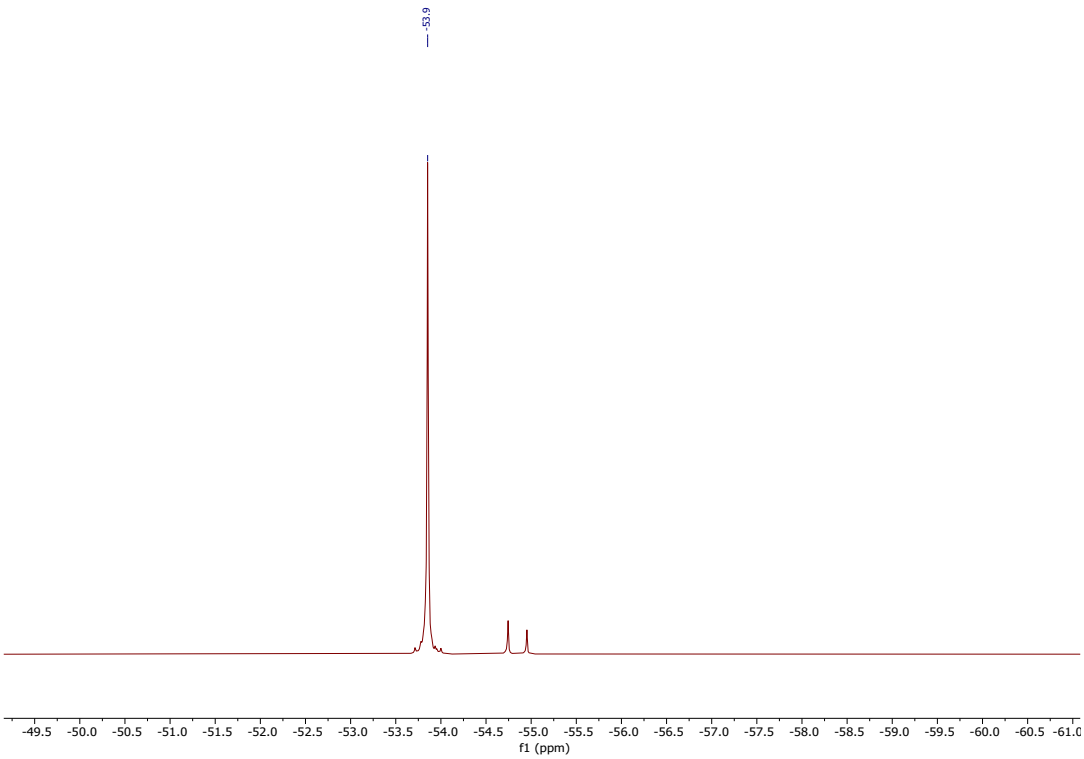

Figure S16: $^{31}P\{^{1}H\}$ NMR spectrum of compound **L4**, (121 MHz, $CDCl_3$).

2.9 Ligand **L5**

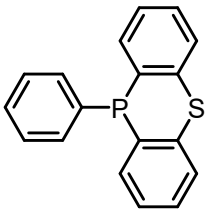

This procedure is based on literature known preparations.[5,6] Diphenylsulfide (2.01 mL, 2.24 g, 12.03 mmol, 1.0 eq.) was solved in 1:1 diethyl ether/*n*-hexane (30 mL), to which TMEDA (3.62 mL, 2.79 g, 24.00 mmol, 2.0 eq.) was added. The mixture was warmed to room temperature overnight. The solution was cooled to 0 °C and *n*-BuLi (15 mL, 0.024 mmol in 1.6 M hexanes, 2.0 eq.) was added. The solution was cooled to −78 °C and a solution of dichlorophenylphosphine (2.67 g, 14.91 mmol, 1.25 eq.) was added dropwise and the reaction warmed to room temperature slowly overnight. All volatile components were removed *in vacuo*. The crude product was purified by column chromatography using a mixture of DCM and hexane (1:3, v/v). The product was obtained as a white solid (1.40 g, 4.79 mmol, 40 %).

^{1}H NMR (300 MHz, C_6D_6) δ(ppm) = 7.15-6.99 (m, 4 H, Arom. *H*), 6.94-6.83 (m, 2 H, aryl-C*H*), 6.82-6.66 (m, 3 H, aryl-C*H*), 6.62-6.50 (m, 4 H, aryl-C*H*).

^{31}P{^{1}H} NMR (121 MHz, C_6D_6) δ(ppm) = −18.40.

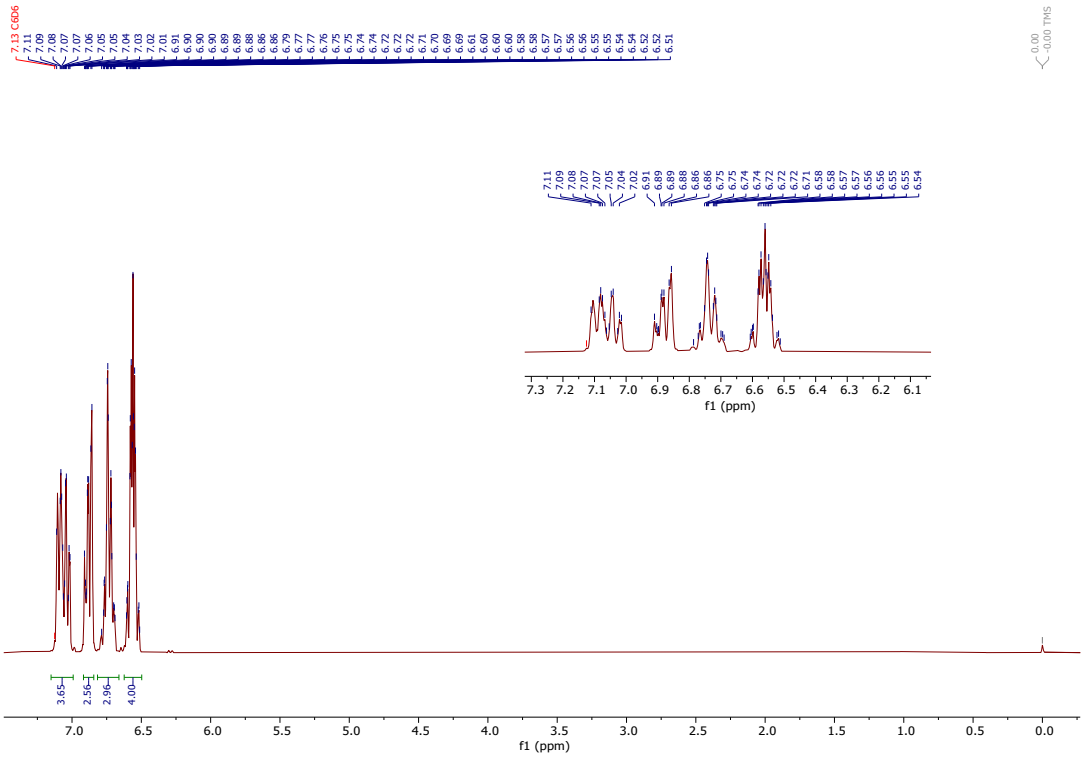

Figure S17: ^{1}H NMR spectrum of compound **L5**, (300 MHz, C_6D_6).

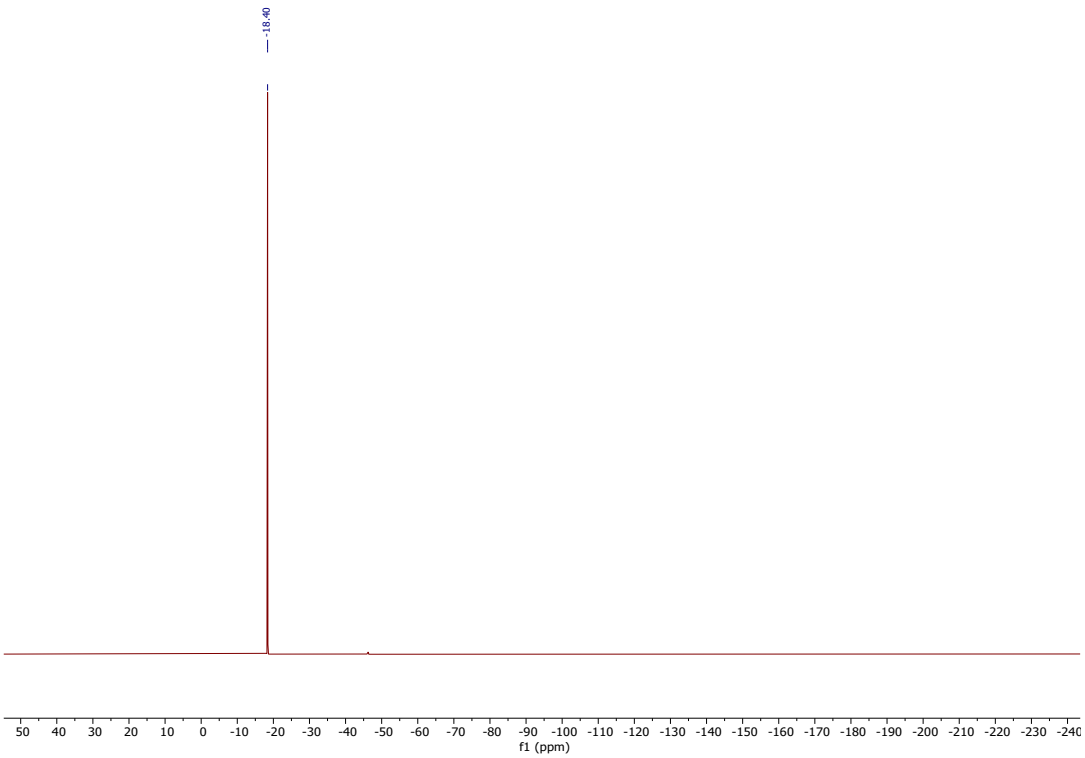

Figure S18: $^{31}P\{^{1}H\}$ NMR spectrum of compound **L5**, (121 MHz, C_6D_6).

2.10 Compound **6** - [Cu(AmIm)(L1)]

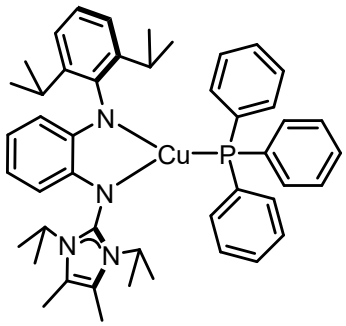

Compound **2** (210 mg, 0.21 mmol, 0.5 eq.) and triphenylphosphine (L1, 114 mg, 0.43 mmol, 1.05 eq.) were dissolved in toluene (10 mL) and stirred overnight. An orange solid formed, which was filtered, washed with cold *n*-hexane and dried *in vacuo*. The complex was obtained as an orange colored solid (282 mg, 0.35 mmol, 89 %). The product was dissolved in toluene (10 mL), layered with *n*-pentane (40 mL) and stored at 10 °C, which afforded the product as yellow crystals, which were suitable for X-ray crystallography.

^{1}H NMR (300 MHz, THF-D8) δ(ppm) = 7.36-7.09 (m, 15 H, 3 C_6H_5), 7.07 (d, *J* = 1.4 Hz, 1 H, aryl-C*H*), 7.05 (br, 1 H, aryl-C*H*), 6.96 (dd, *J* = 8.5, 6.4 Hz, aryl-C*H*), 6.29 (ddd, *J* = 7.8, 7.1, 1.6 Hz, 1 H, aryl-C*H*), 6.09 (dd, *J* = 7.3, 1.6 Hz, 1 H, aryl-C*H*), 5.92 (td, *J* = 7.3, 1.5 Hz, 1 H, aryl-C*H*), 5.80 (dd, *J* = 7.8, 1.4 Hz, 1 H, aryl-C*H*), 4.83 (sept, *J* = 7.1 Hz, 2 H, NC*H*$(CH_3)_2$), 3.59 (sept, 2 H, C*H*$(CH_3)_2$), 2.22 (s, 6 H, CH_3), 1.26 (d, *J* = 7.0 Hz, 6 H, CH(C*H*$_3)_2$), 1.01 (d, *J* = 6.9 Hz, 6 H, CH(C*H*$_3)_2$), 0.89 (d, *J* = 7.2 Hz, 6 H, NCH(C*H*$_3)_2$), 0.78 (d, *J* = 6.9 Hz, 6 H, NCH(C*H*$_3)_2$).

^{13}C{^{1}H} NMR (76 MHz, THF-D8) δ(ppm) = 154.87, 152.87, 152.65, 145.42, 144.25, 135.67, 135.18, 134.81 (d, *J* = 16.3 Hz), 130.53 (d, *J* = 1.9 Hz), 129.42 (d, *J* = 10.0 Hz), 123.63, 121.95, 119.93, 119.70, 114.32, 109.40 (d, *J* = 14.5 Hz), 48.56, 28.34, 24.85, 22.04, 21.24, 10.31.

^{31}P{^{1}H} NMR (122 MHz, THF-D8) δ(ppm) = 9.41.

Elemental Analysis: Calcd. for $C_{47}H_{56}CuN_4P$: C 73.17, H 7.32, N 7.26.
Found: C 73.15, H 7.25, N 7.28.

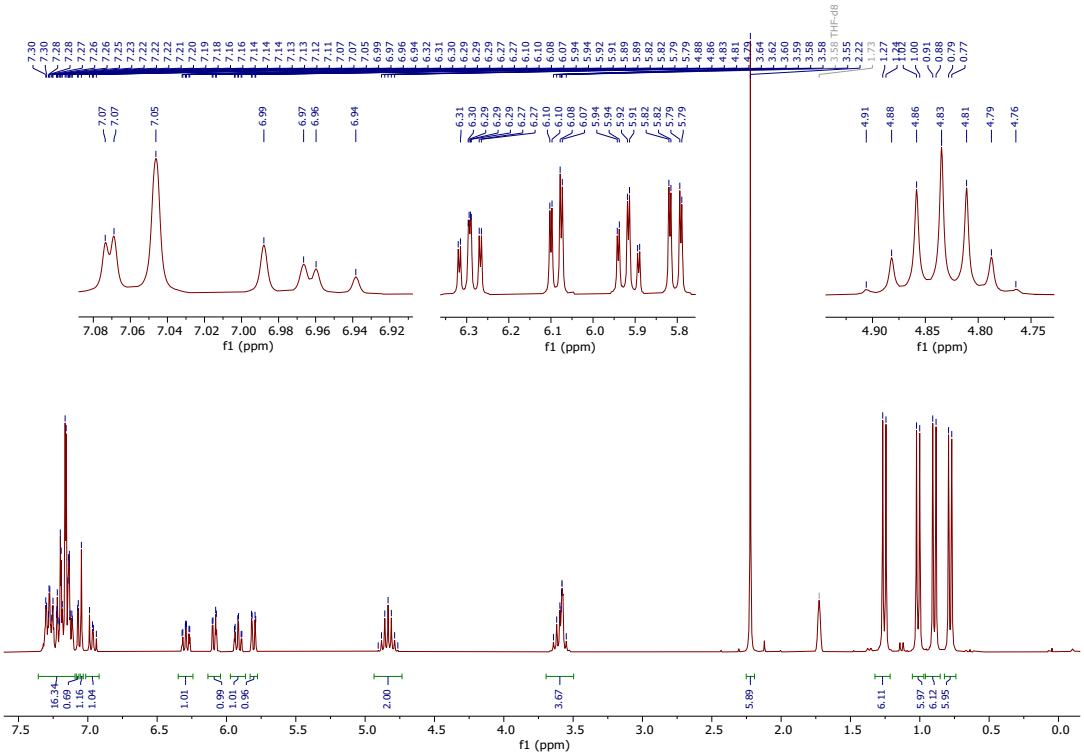

Figure S19: ^{1}H NMR spectrum of compound **6**, (300 MHz, THF-D8).

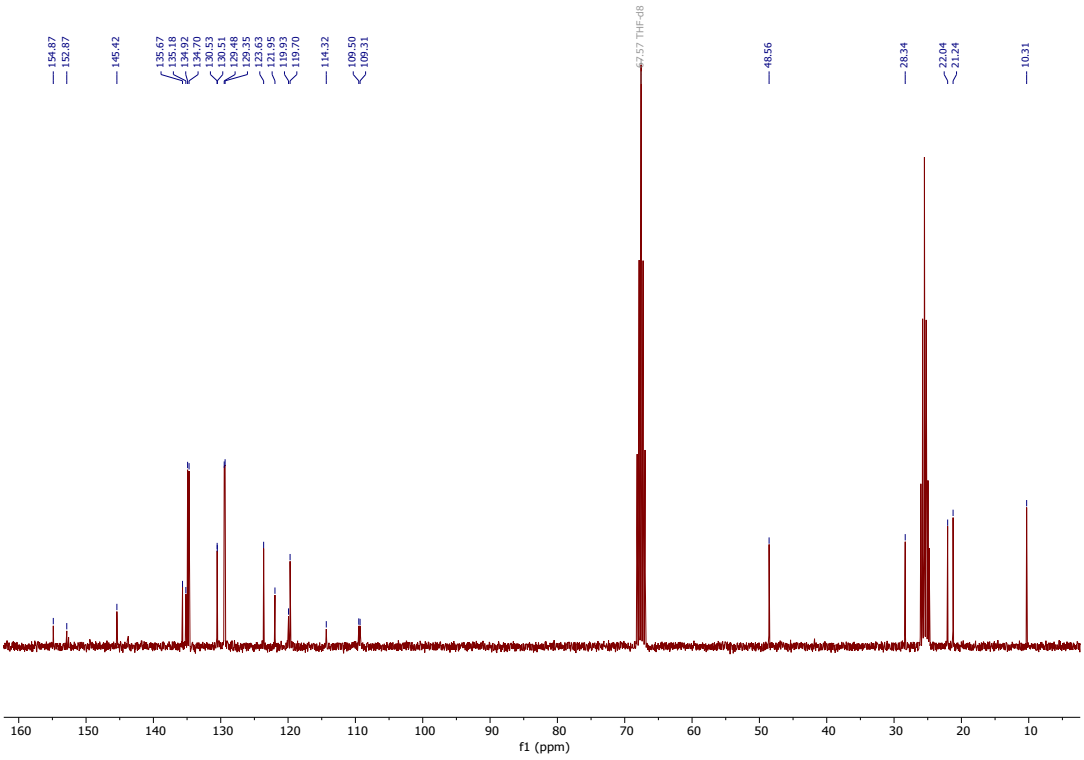

Figure S20: $^{13}C\{^{1}H\}$ NMR spectrum of compound **6**, (76 MHz, THF-D8).

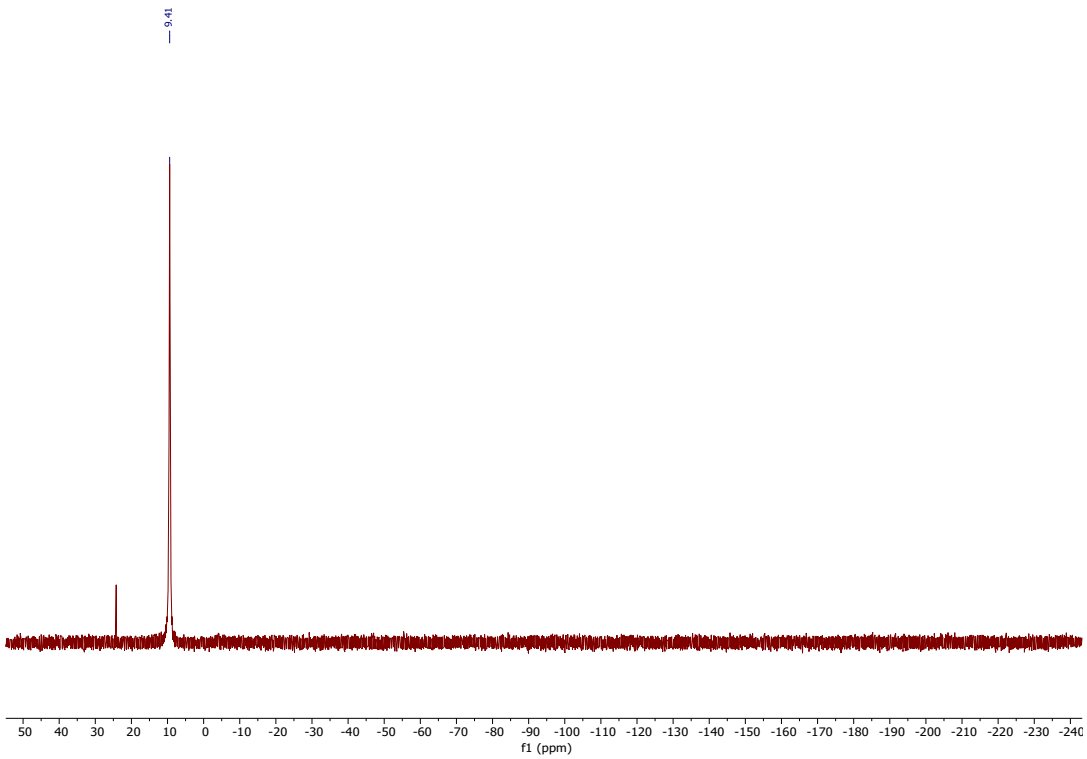

Figure S21: $^{31}P\{^{1}H\}$ NMR spectrum of compound **6**, (122 MHz, THF-D8).

2.11 Compound **7** - [Cu(AmIm)(L2)]

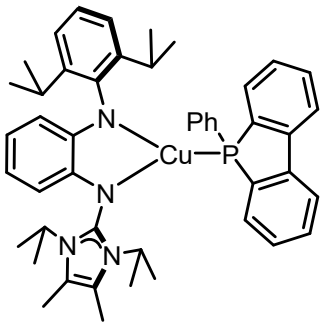

Compound **2** (100 mg, 0.10 mmol, 0.5 eq.) and ligand **L2** (54 mg, 0.21 mmol, 1.05 eq.) were dissolved in benzene (10 mL) and stirred overnight. A red solid formed, which was filtered, washed with cold *n*-hexane and dried *in vacuo*. The complex was obtained as a red colored solid (136 mg, 0.18 mmol, 90 %). The product was dissolved in toluene (10 mL), layered with *n*-pentane (40 mL) and stored at −40 °C, which afforded the product as red crystals, which were suitable for X-ray crystallography.

^{1}H NMR (300 MHz, THF-D8) δ(ppm) = 7.97-7.88 (m, 2 H, aryl-C*H*), 7.49-7.35 (m, 2 H, aryl-C*H*), 7.25-7.03 (m, 9 H, aryl-C*H*), 7.03-6.93 (m, 4 H, aryl-C*H*), 6.25 (ddd, *J* = 7.8, 7.0, 1.7 Hz, 1 H, aryl-C*H*), 5.98-5.93 (m, 1 H, aryl-C*H*), 5.89 (td, *J* = 7.1, 1.4 Hz, 1 H, Arom. *H*), 5.78 (dd, *J* = 7.8, 1.4 Hz, 1 H, aryl-C*H*), 4.65 (sept, *J* = 7.1 Hz, 2 H, NC*H*$(CH_3)_2$), 3.65 (sept, 2 H, C*H*$(CH_3)_2$), 2.16 (s, 6 H, CH_3), 1.23 (d, *J* = 7.0 Hz, 6 H, NC*H*$(CH_3)_2$), 1.01 (dd, *J* = 11.2, 7.0 Hz, 12 H, CH(C*H*$_3)_2$), 0.96 (d, *J* = 6.9 Hz, 6 H, NCH(C*H*$_3)_2$).

^{13}C{^{1}H} NMR (76 MHz, THF-D8) δ(ppm) = 154.68, 153.31, 152.13, 152.08, 145.23, 143.89 ($J_{P,C}$ = 19.5 Hz), 140.12 ($J_{P,C}$ = 41 Hz) 138.60, 134.51, 134.28, 131.38, 131.06, 130.99 ($J_{P,C}$ = 24 Hz), 129.48 ($J_{P,C}$ = 54 Hz), 129.45 ($J_{P,C}$ = 11 Hz), 129.08, 126.21, 123.55, 122.09 ($J_{P,C}$ = 26 Hz), 119.79, 119.39, 113.25, 109.60, 109.01, 48.57, 28.53, 26.09, 21.74, 21.67, 21.35, 10.11.

^{31}P{^{1}H} NMR (122 MHz, THF-D8) δ(ppm) = 1.77.

Elemental Analysis: Calculated for $C_{47}H_{55}CuN_4P$: C 73.27, H 7.20, N 7.27.
Found: C 73.15, H 7.18, N 7.43.

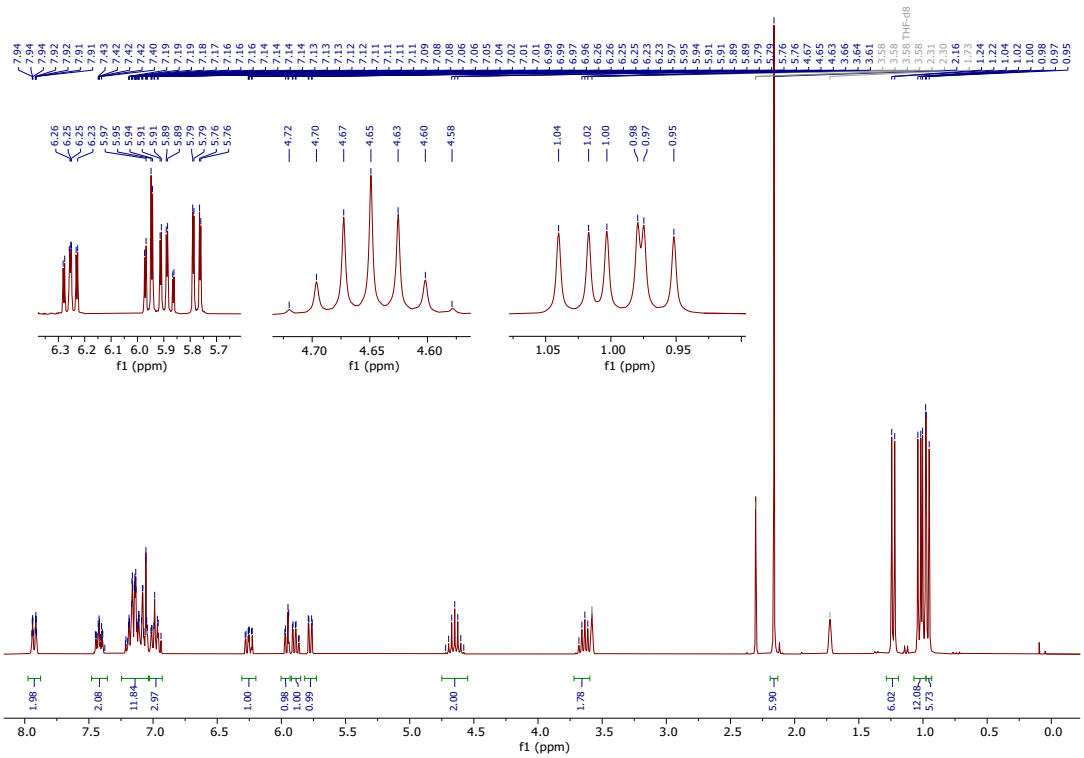

Figure S22: ^{1}H NMR spectrum of compound **7**, (300 MHz, THF-D8).

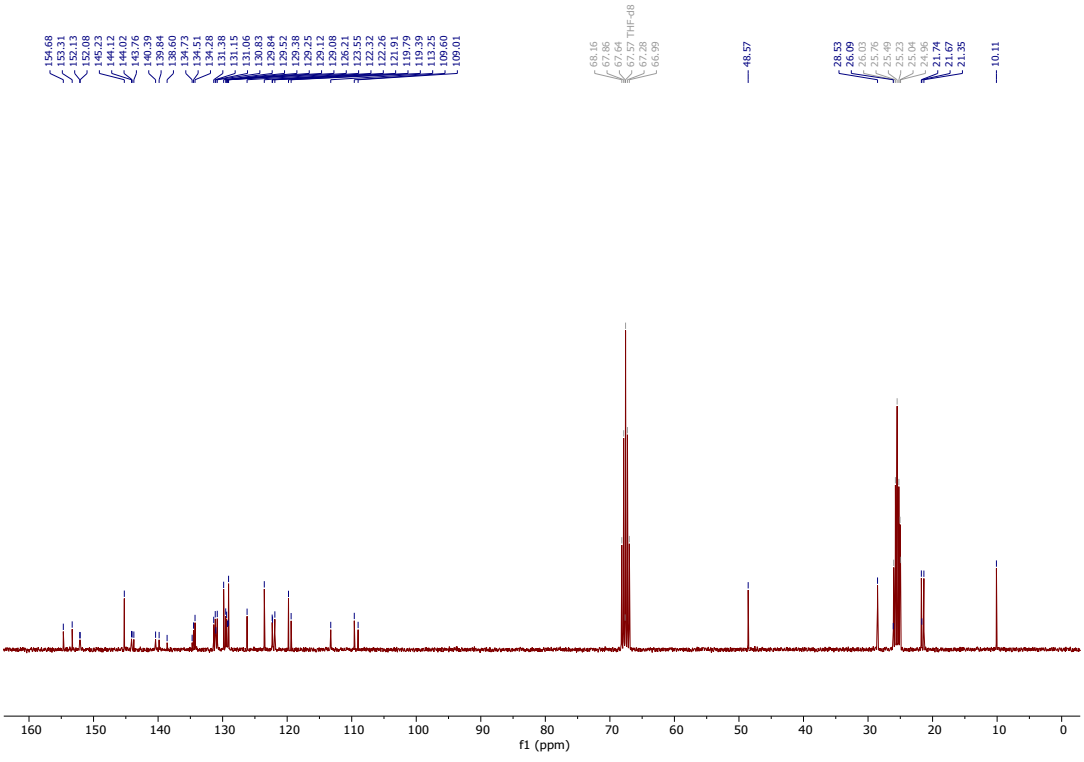

Figure S23: ^{13}C{^{1}H} NMR spectrum of compound **7**, (76 MHz, THF-D8).

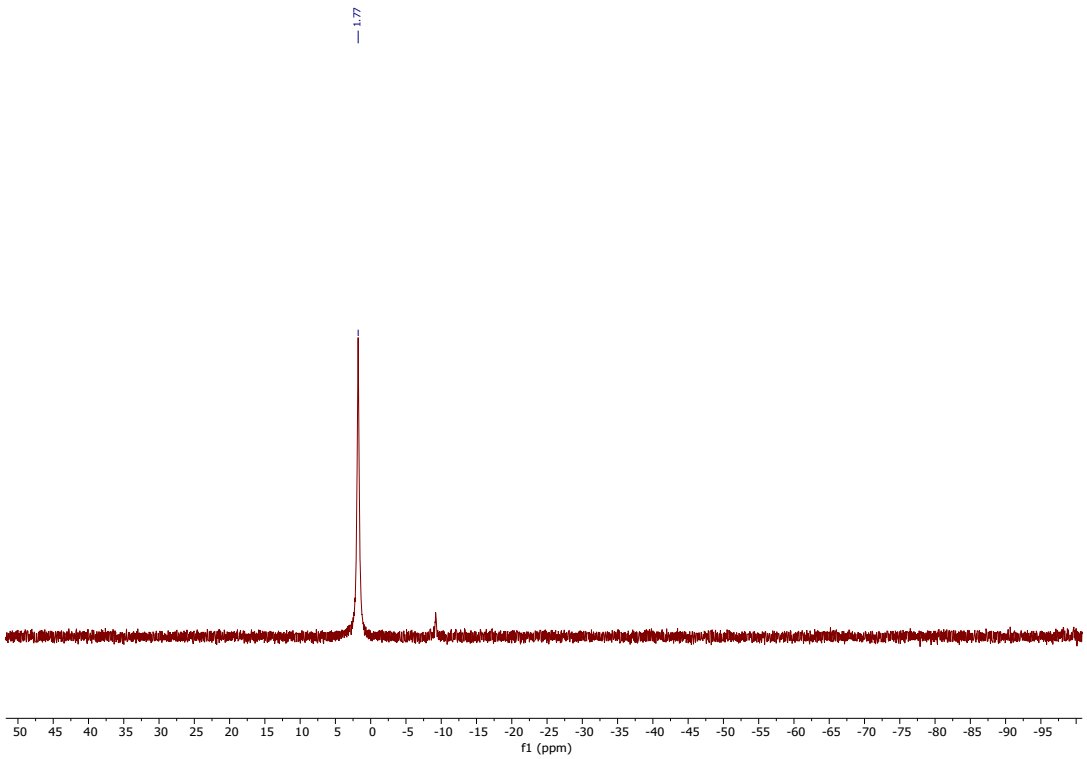

Figure S24: $^{31}P\{^{1}H\}$ NMR spectrum of compound **7**, (122 MHz, THF-D8).

2.12 Compound **8** - [Cu(AmIm)(L3)]

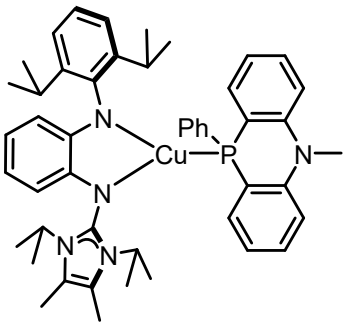

Compound **2** (128 mg, 0.13 mmol, 0.5 eq.) and ligand **L3** (72.7 mg, 0.25 mmol, 1.0 eq.) were solved in benzene (10 mL) and stirred overnight. An orange-yellow solid formed, which was filtered, washed with cold *n*-hexane and dried *in vacuo*. The complex was obtained as an orange-yellow colored solid (149 mg, 0.19 mmol, 74 %). The product was dissolved in THF (10 mL) and layered with *n*-hexane (40 mL), which afforded the product as yellow crystals, which were suitable for X-ray crystallography.

Due to the low solubility (in C_6D_6 and THF-D_8) meaningful ^{13}C NMR spectra could not be recorded.

^1H NMR (300 MHz, THF-D8) δ (ppm) = 7.32 (ddt, *J* = 8.2, 7.2, 1.4 Hz, 2 H, aryl-C*H*), 7.25-7.15 (m, 1 H, aryl-C*H*), 7.15-7.06 (m, 9 H, aryl-C*H*), 7.05-6.95 (m, 3 H, aryl-C*H*), 6.67 (t, *J* = 7.3 Hz, 1 H, aryl-C*H*), 6.30 (td, *J* = 7.5, 1.6 Hz, 1 H, aryl-C*H*), 6.10 (dd, *J* = 7.4, 1.5 Hz, 1 H, aryl-C*H*), 5.94 (td, *J* = 7.2, 1.4 Hz, 1 H, aryl-C*H*), 5.84 (dd, *J* = 7.8, 1.4 Hz, 1 H, aryl-C*H*), 4.87 (sept, *J* = 7.2 Hz, 2 H, NC*H*$(CH_3)_2$, 3.69 (sept, *J* = 6.9 Hz, 2 H, C*H*$(CH_3)_2$), 3.43 (s, 3H, NC*H*$_3$), 2.31 (s, 6 H, C*H*$_3$), 1.30 (d, *J* = 7.0 Hz, 6 H, NCH(C*H*$_3)_2$, 1.06 (dd, *J* = 11.5, 7.0 Hz, 12 H, CH(C*H*$_3)_2$), 0.92 (d, *J* = 6.9 Hz, 6 H, NCH(C*H*$_3)_2$).

$^{31}P\{^1H\}$ NMR (121 MHz, THF-D8) δ (ppm) = −22.23.

Elemental Analysis: Calculated for $C_{48}H_{58}CuN_5P$: C 72.11, H 7.31, N 8.76.
Found: C 71.96, H 7.25, N 8.64.

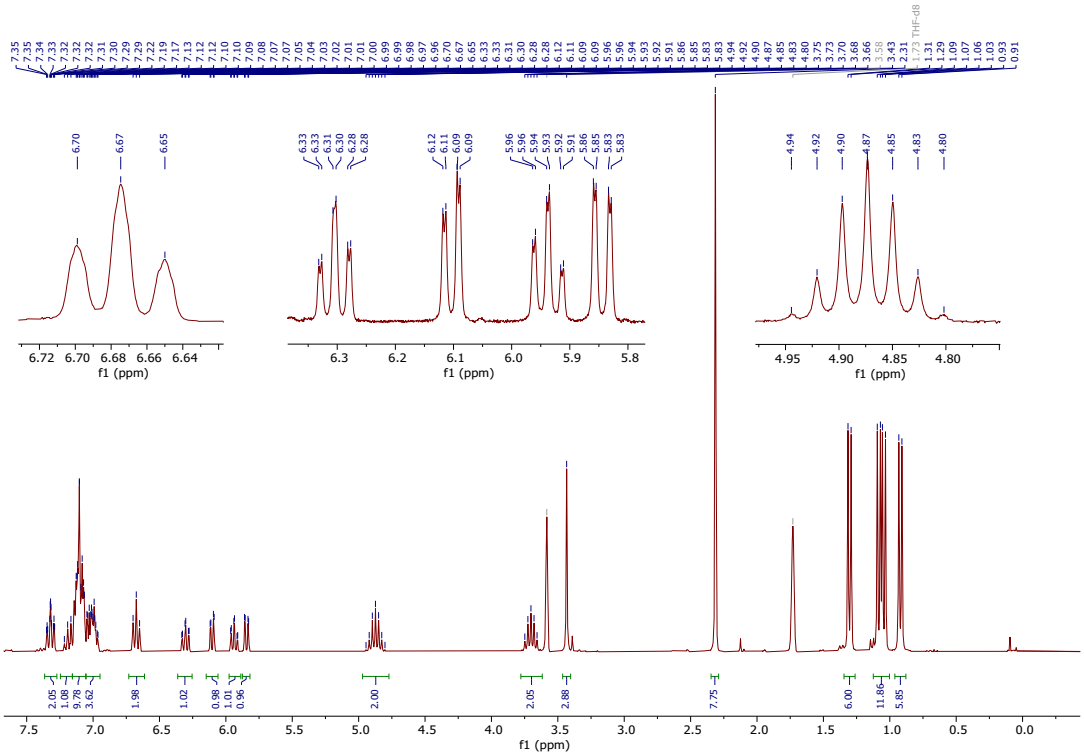

Figure S25: ^{1}H NMR spectrum of compound **8**, (300 MHz, THF-D8).

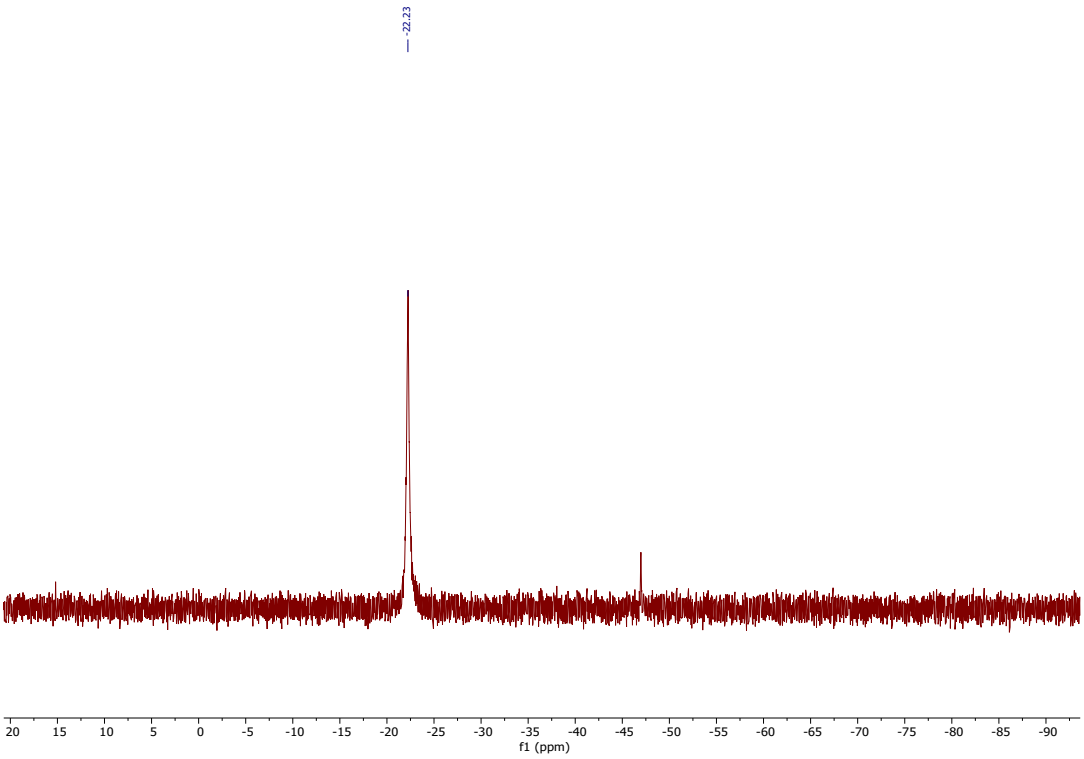

Figure S26: $^{31}P\{^{1}H\}$ NMR spectrum of compound **8**, (121 MHz, THF-D8).

2.13 Compound **9** - [Cu(AmIm)(L4)]

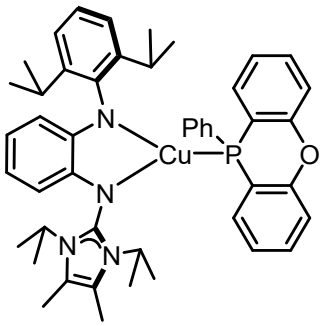

Compound **2** (0.15 g, 0.15 mmol, 0.5 eq.) and ligand **L4** (81.4 mg, 0.29 mmol, 1.0 eq.) were solved in benzene (10 mL) and stirred overnight. An orange solid formed, which was filtered, washed with cold *n*-hexane and dried *in vacuo*. The complex was obtained as an orange colored solid (132 mg, 0.17 mmol, 60 %). The product was dissolved in THF (10 mL), layered with *n*-pentane (40 mL) and stored at −40 °C, which afforded the product as yellow crystals, which were suitable for X-ray crystallography.

Due to the low solubility (in C_6D_6 and THF-D_8) meaningful ^{13}C NMR spectra could not be recorded.

^1H NMR (300 MHz, THF-D8) δ (ppm) = 7.44-7.29 (m, 4 H, aryl-C*H*), 7.21-7.05 (m, 7 H, aryl-C*H*), 6.99 (dd, *J* = 8.4, 6.5 Hz, 1 H, aryl-C*H*), 6.90 (ddd, 2 H, aryl-C*H*), 6.77 (t, *J* = 7.3 Hz, 2 H, aryl-C*H*), 6.30 (t, *J* = 7.7 Hz, 1 H, aryl-C*H*), 6.09 (dd, *J* = 7.4, 1.6 Hz, 1 H, aryl-C*H*), 5.95 (dd, *J* = 7.9, 6.5 Hz, 1 H, aryl-C*H*), 5.85 (dd, *J* = 7.9, 1.4 Hz, 1 H, aryl-C*H*), 4.87 (sept, *J* = 7.0 Hz, 2 H, NC*H*(CH_3)$_2$), 3.67 (sept, *J* = 6.9 Hz, 2 H, C*H*(CH_3)$_2$), 2.30 (s, 6 H, C*H*$_3$), 1.33 (d, *J* = 7.1 Hz, 6 H, NCH(C*H*$_3$)$_2$), 1.05 (dd, *J* = 9.0, 7.0 Hz, 12 H, CH(C*H*$_3$)$_2$), 0.89 (d, *J* = 6.9 Hz, 6 H, NCH(C*H*$_3$)$_2$).

$^{31}P\{^1H\}$ NMR (122 MHz, THF-D8) δ (ppm) = −29.53.

Elemental Analysis: Calculated for $C_{47}H_{55}CuN_4OP$: C 71.78, H 7.05, N 7.12.
Found: C 71.95, H 7.18, N 7.08.

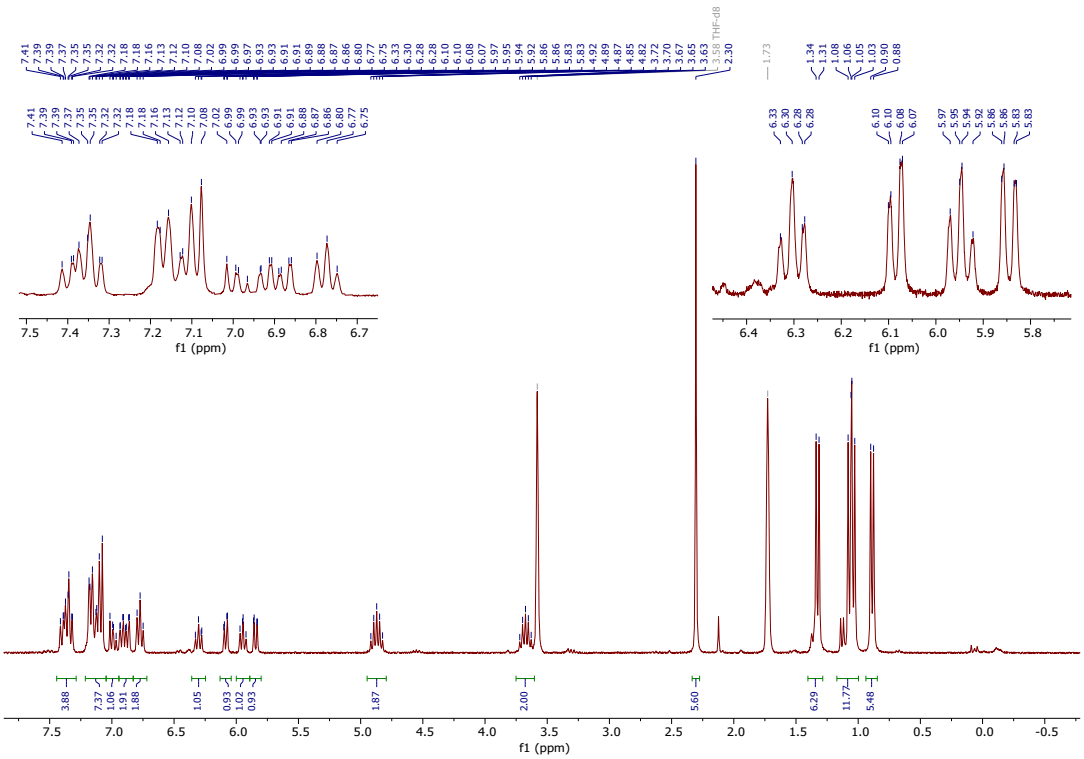

Figure S27: ^{1}H NMR spectrum of compound **9**, (300 MHz, THF-D8).

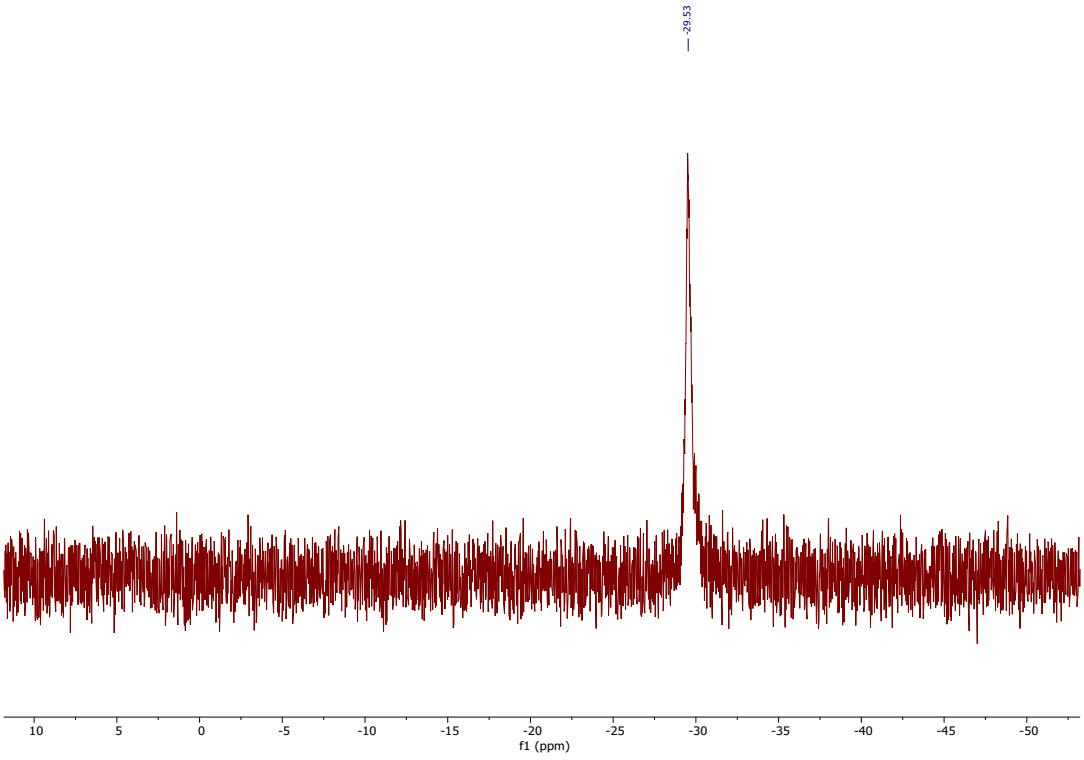

Figure S28: $^{31}P\{^{1}H\}$ NMR spectrum of compound **9**, (122 MHz, THF-D8).

2.14 Compound **10** - [Cu(AmIm)(L5)]

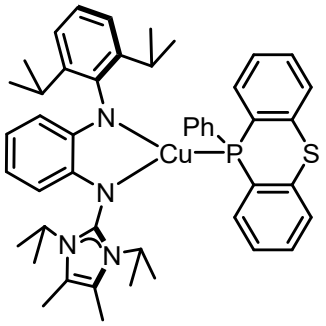

Compound **2** (200 mg, 0.20 mmol, 0.5 eq.) and ligand **L5** (121 mg, 0.41 mmol, 1.05 eq.) were solved in toluene (10 mL) and stirred overnight. An orange solid formed, which was filtered, washed with cold *n*-hexane and dried *in vacuo*. The complex was obtained as an orange colored solid (185.6 mg, 0.23 mmol, 60 %). Orange crystals were harvested from the reaction solution, which were suitable for X-ray crystallography.

Due to the low solubility (in C_6D_6 and THF-D_8) meaningful ^{13}C NMR spectra could not be recorded.

^1H NMR (300 MHz, THF-D8) δ(ppm) = 7.57-7.51 (m, 1 H, aryl-C*H*), 7.49-6.91 (m, 16 H, aryl-C*H*), 6.28 (ddd, *J* = 7.8, 7.1, 1.6 Hz, 1 H, aryl-C*H*), 6.03 (dd, *J* = 7.4, 1.6 Hz, 1 H, aryl-C*H*), 5.92 (td, *J* = 7.2, 1.5 Hz, 1 H, aryl-C*H*), 5.83 (dd, *J* = 7.8, 1.4 Hz, 1 H, aryl-C*H*), 4.81 (sept, *J* = 7.1 Hz, 2 H, NC*H*(CH_3)$_2$), 3.64 (sept, 2 H, C*H*(CH_3)$_2$), 2.32 (s, 6 H, C*H*$_3$), 1.29 (d, *J* = 7.0 Hz, 6 H, NCH(C*H*$_3$)$_2$), 1.06 (dd, *J* = 17.9, 7.0 Hz, 12 H, CH(C*H*$_3$)$_2$), 0.93 (d, *J* = 7.0 Hz, 6 H, NCH(C*H*$_3$)$_2$).

$^{31}P\{^1H\}$ NMR (122 MHz, CD_2Cl_2) δ(ppm) = −5.26.

Elemental Analysis: Calculated for $C_{47}H_{55}CuN_4SP$: C 70.34, H 6.91, N 6.98.
Found: C 70.40, H 6.85, N 6.85.

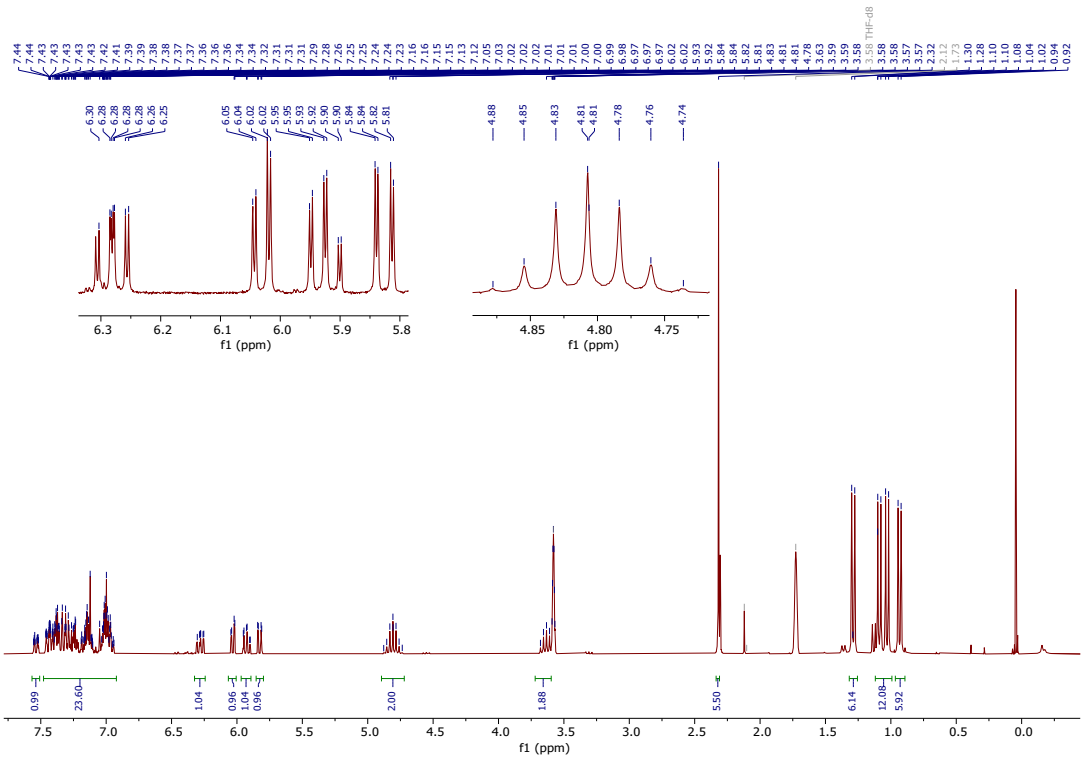

Figure S29: ^{1}H NMR spectrum of compound **10**, (300 MHz, THF-D8).

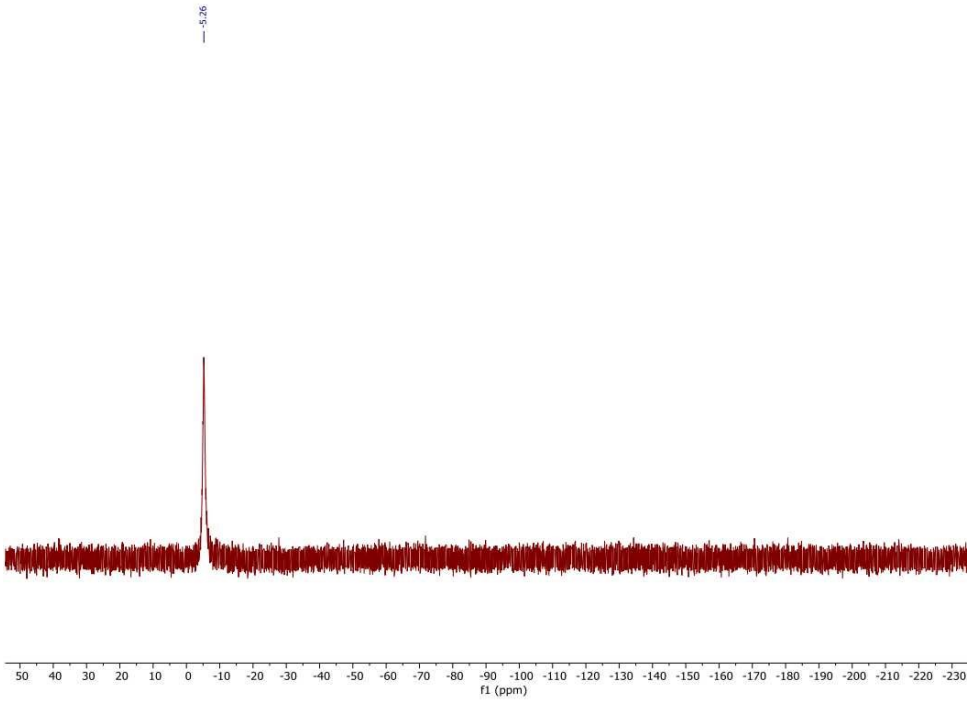

Figure S30: $^{31}P\{^{1}H\}$ NMR spectrum of compound **10**, (121 MHz, THF-D8).

3. X-Ray Crystallography

Data collections were performed by mounting single crystals on glass fibres or MiTeGen mounts in perfluorinated oil. Diffractometers used for intensity measurements (at 100 K) were Oxford Diffraction Xcalibur E with Mo K_α radiation or Rigaku XtaLab Synergy S Single Source with either Mo K_α or Cu K_α micro source. Absorption correction was applied based on multi-scan methods. Data reduction was performed using the program CrysalisPro[27] The structures were solved with SHELXT-14/5[28] and refined anisotropically on F^2 using the programs SHELXL-14/7 and SHELXL-17/1[29] in OLEX2[30].

The Compounds **8** and **9** were refined as non-merohedral twins.

For compound **9** no appropriate model could be established for cocrystallied solvent molecules; the data were processed using the PLATON/SQUEEZE program.[31] A solvent mask was calculated and 40 electrons were found in a volume of 145 Å^3 in 1 void per unit cell. This is consistent with the presence of 0.5 THF per Asymmetric Unit which account for 40 electrons per unit cell.

Complete data have been deposited with the Cambridge Crystallographic Data Centre under the CCDC numbers 2428671 (**1**), 2428672 (**2**), 2428673 (**3**), 2428674 (**4**), 2428675 (**5**), 2428676 (**6**), 2428677 (**7**), 2428678 (**8**), 2428679 (**9**), 2428680 (**10**). These data can be obtained free of charge from http://www.ccdc.cam.ac.ak/.

The standard deviation of the angle σ as the sum of all three bond angles at copper(I) was calculated using the following formula:

$$\sigma = \sqrt{\frac{1}{9} \cdot (\sigma_1^2 + \sigma_2^2 + \sigma_3^2)}$$

Table S1: Crystallographic data for compounds **1** and **2**.

Compound	[Cu(HAmIm)Cl] **1** · PhMe	$[Cu_2(AmIm)_2]$ **2**
CCDC entry number	2428671	2428672
Empirical formula	$C_{36}H_{50}ClCuN_4$	$C_{58}H_{82}Cu_2N_8$
Formula weight	637.79 [g·mol^{-1}]	1018.39 [g·mol^{-1}]
Temperature	100(2) K	100(2) K
Wavelength	0.71073 Å	1.54184 Å
Crystal system	Monoclinic	Monoclinic
Space group	$P2_1/c$	$I2/a$
a	10.1475(4) Å	24.22247(12) Å
b	14.4372(7) Å	10.96270(4) Å
c	23.2269(9) Å	22.52171(10) Å
α	90°	90°
β	92.120(3)°	115.0135(6)°
γ	90°	90°
Volume	3400.4(3) Å^3	5419.57(5) Å^3
Z	4	4
Density (calculated)	1.246 Mg/m^3	1.248 Mg/m^3
Absorption coefficient	0.751 mm^{-1}	1.298 mm^{-1}
F(000)	1360	2176
Crystal size	0.460 × 0.210 × 0.180 mm^3	0.120 × 0.090 × 0.070 mm^3
Theta range for data collection	2.252° to 28.282°	4.028° to 77.369°
Reflections collected	55407	113844
Independent reflections	8447 [R_{int} = 0.0763]	5759 [R_{int} = 0.0253]
Goodness-of-fit on F^2	1.185	1.049
R1 [I > 2σ(I)]	0.0728	0.0266
wR_2	0.1516	0.0719

Table S2: Crystallographic data for compounds **4** and **5**.

Compound	[Cu(AmIm)(phen)] **4**	[Cu(AmIm)(neo)] **5**

Identification code	2428674	2428675
Empirical formula	$C_{41}H_{49}CuN_6$	$C_{43}H_{53}CuN_6$
Formula weight	689.40 [g·mol^{-1}]	717.45 [g·mol^{-1}]
Temperature	100(2) K	100(2) K
Wavelength	1.54184 Å	1.54184 Å
Crystal system	Orthorhombic	Monoclinic
Space group	*Pbcn*	$P2_1/c$
a	18.9928(4) Å	13.85297(6) Å
b	22.3123(5) Å	13.80287(5) Å
c	17.0614(4) Å	19.92220(8) Å
α	90°	90°
β	90°	93.8705(4)°
γ	90°	90°
Volume	7230.2(3) Å^3	3800.65(3) Å^3
Z	8	4
Density (calculated)	1.267 Mg/m^3	1.254 Mg/m^3
Absorption coefficient	1.131 mm^{-1}	1.095 mm^{-1}
F(000)	2928	1528
Crystal size	0.160 × 0.080 × 0.040 mm^3	0.230 × 0.140 × 0.110 mm^3
Theta range for data collection	3.056° to 77.515°	3.197° to 77.703°
Reflections collected	123743	201613
Independent reflections	7662 [R_{int} = 0.0831]	8079 [R_{int} = 0.0367]
Goodness-of-fit on F^2	1.027	1.069
R1 [I > 2σ(I)]	0.0457	0.0300
wR2	0.1195	0.0842

Table S3: Crystallographic data for compounds **3** and **9**.

Compound	$[Cu_2(AmIm)_2(OH)_2]$ **3** · C_6H_6	[Cu(AmIm)(L4)] **9**
Identification code	2428673	2428679
Empirical formula	$C_{35}H_{48}CuN_4O$	$C_{47}H_{54}CuN_4OP$

Formula weight	604.31 [g·mol^{-1}]	785.45 [g·mol^{-1}]
Temperature	100(2) K	100(2) K
Wavelength	1.54184 Å	1.54184 Å
Crystal system	Monoclinic	Triclinic
Space group	$P2_1/c$	$P(-1)$
a	14.27540(10) Å	11.6370(2) Å
b	12.23630(10) Å	11.72410(10) Å
c	18.6878(2) Å	17.9114(2) Å
α	90°	93.4210(10) °
β	96.1930(10)°	104.2770(10)
γ	90°	113.5760(10)
Volume	3245.30(5) Å^3	2135.81(5) Å^3
Z	4	2
Density (calculated)	1.237 Mg/m^3	1.277 Mg/m^3
Absorption coefficient	1.189 mm^{-1}	1.399 mm^{-1}
F(000)	1292	872
Crystal size	0.155 × 0.111 × 0.082 mm^3	0.093 × 0.058 × 0.042 mm^3
Theta range for data collection	3.114° to 77.798°	4.181° to77.483°
Reflections collected	159311	16777
Independent reflections	6877 [R_{int} = 0.0422]	16777
Goodness-of-fit on F^2	1.052	1.064
R1 [I > 2σ(I)]	0.0350	0.0586
wR_2	0.0999	0.1716

Table S4: Crystallographic data for compounds **7** and **8**.

Compound	[Cu(AmIm)(L3)] **8** · 0.5 THF	[Cu(AmIm)(L2)] **7**
Identification code	2428678	2428677
Empirical formula	$C_{50}H_{61}CuN_5O_{0.50}P$	$C_{54}H_{62}CuN_4P$
Formula weight	834.54 [g·mol^{-1}]	861.58 [g·mol^{-1}]
Temperature	100(2) K	100(2) K
Wavelength	1.54184 Å	0.71073 Å
Crystal system	Orthorhombic	Triclinic

Space group	*Pbca*	*P*(-1)
a	17.35640(10) Å	12.2360(3) Å
b	22.28900(10) Å	12.5547(3) Å
c	23.08570(10) Å	15.7648(4) Å
α	90°	78.568(2)°
β	90°	76.947(2)°
γ	90°	89.429(2)°
Volume	8930.86(8) $Å^3$	2310.86(10) $Å^3$
Z	8	2
Density (calculated)	1.241 Mg/m^3	1.238 Mg/m^3
Absorption coefficient	1.335 mm^{-1}	0.548 mm^{-1}
F(000)	3552	916
Crystal size	0.172 × 0.081 × 0.056 mm^3	0.240 × 0.170 × 0.150 mm^3
Theta range for data collection	3.753° to 80.926°	2.337° to 38.355°
Reflections collected	21265	225409
Independent reflections	21265	24554 [R_{int} = 0.0532]
Goodness-of-fit on F^2	1.048	1.031
R1 [I > 2σ(I)]	0.0460	0.0383
wR_2	0.1172	0.0951

Table S5: Crystallographic data for compounds **6** and **10**.

Compound	[Cu(AmIm)(L5)] **10**	[Cu(AmIm)(L1)] **6**
Identification code	2428680	2428676
Empirical formula	$C_{50.50}H_{58}CuN_4PS$	$C_{47}H_{56}CuN_4P$
Formula weight	847.48 [$g \cdot mol^{-1}$]	771.46 [$g \cdot mol^{-1}$]
Temperature	100(2) K	100(2) K
Wavelength	0.71073 Å	1.54184 Å
Crystal system	Triclinic	Triclinic
Space group	*P*(-1)	*P*(-1)
a	11.96120(10) Å	13.09850(10) Å

b	12.42860(10) Å	16.27550(10) Å
c	17.2938(2) Å	20.3130(2) Å
α	93.4370(10)°	90.1040(10)°
β	103.8840(10)°	95.2480(10)°
γ	114.8190(10)°	90.0380(10)°
Volume	2227.30(4) $Å^3$	4312.26(6) $Å^3$
Z	2	4
Density (calculated)	1.264 Mg/m^3	1.188 Mg/m^3
Absorption coefficient	0.612 mm^{-1}	1.327 mm^{-1}
F(000)	898	1640
Crystal size	0.520 × 0.270 × 0.150 mm^3	0.160 × 0.120 × 0.080 mm^3
Theta range for data collection	1.988° to 36.318°	2.715° to 77.726°
Reflections collected	218259	181626
Independent reflections	21590 [R_{int} = 0.0349]	18172 [R_{int} = 0.0695]
Goodness-of-fit on F^2	1.034	1.293
R1 [I > 2σ(I)]	0.0442	0.0785
wR_2	0.1160	0.1820

4. Computational Studies

4.1 Compound **4** - [Cu(AmIm)(phen)]

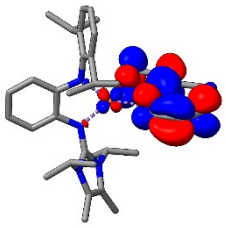

LUMO (-1.95 eV)

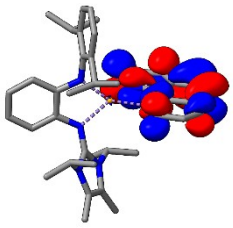

LUMO+1 (-1.86 eV)

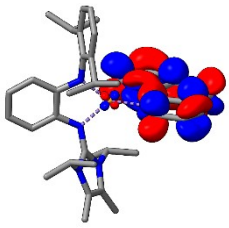

LUMO+2 (-0.68 eV)

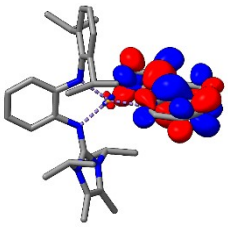

LUMO+3 (+0.08 eV)

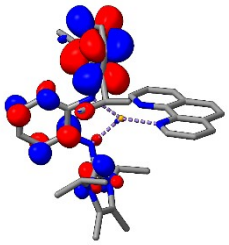

LUMO+4 (+0.24 eV)

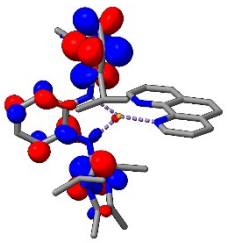

LUMO+5 (+0.41 eV)

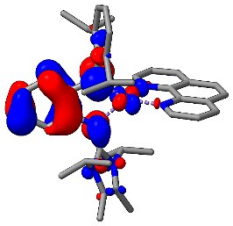

HOMO (-4.02 eV)

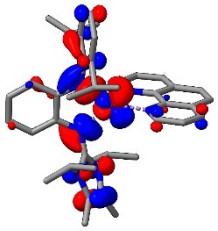

HOMO-1 (-4.67 eV)

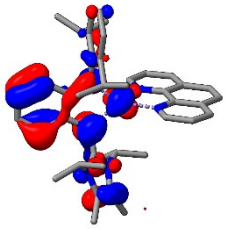

HOMO-2 (-5.34 eV)

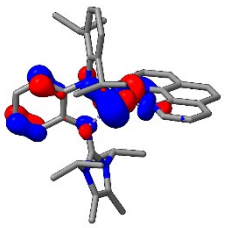

HOMO-3 (-5.57 eV)

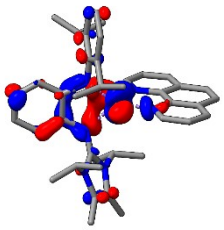

HOMO-4 (-5.99 eV)

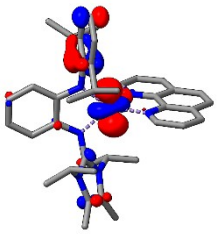

HOMO-5 (-6.27 eV)

Figure S31: Molecular orbitals of **4** with their respective energies given in eV. The top half shows the lowest unoccupied molecular orbitals, while the bottom half shows the highest occupied molecular orbitals. Blue and red correspond to a negative and positive sign respectively (isosurface: ±0.035).

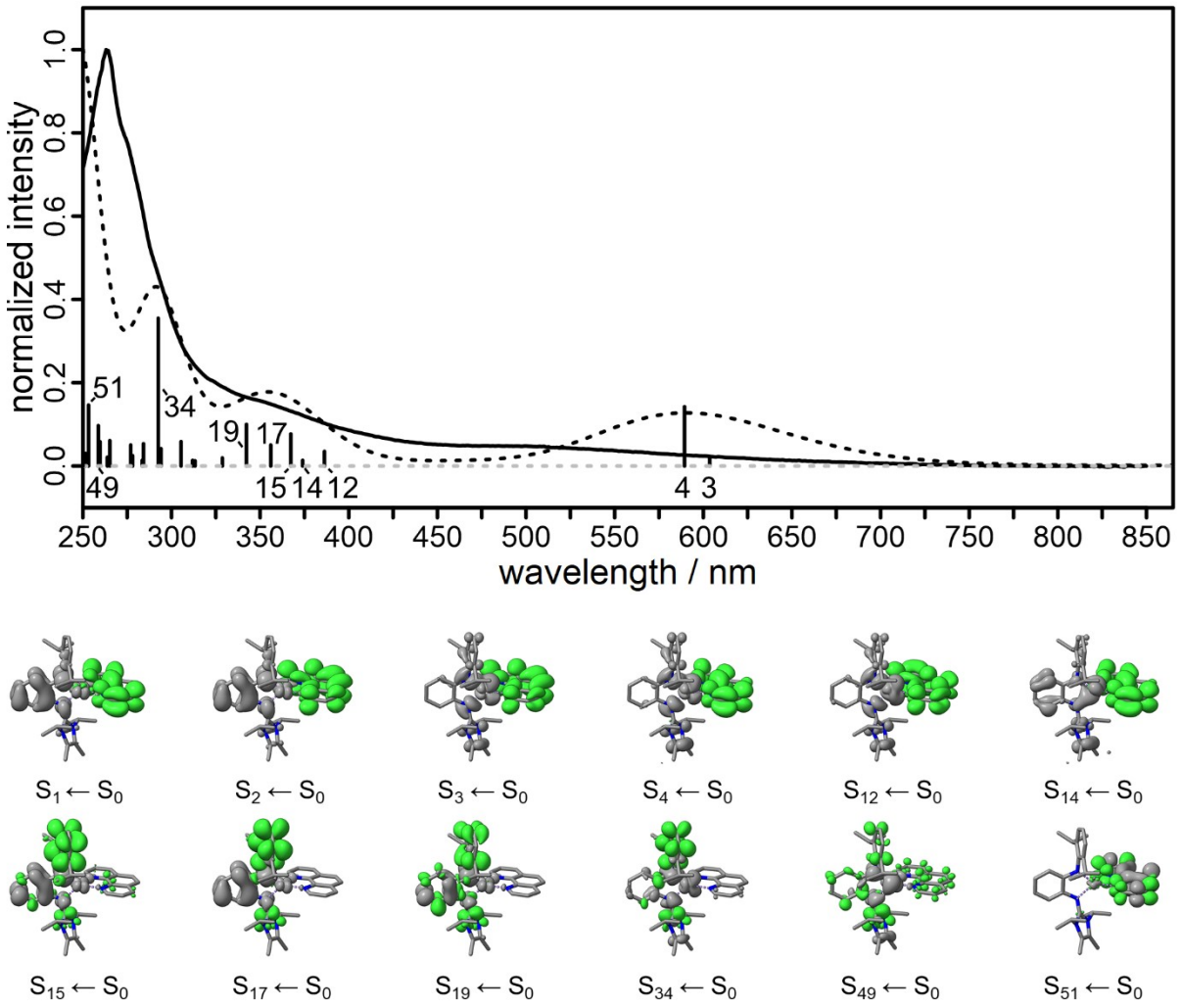

Figure S32: Normalised excitation spectrum (dotted black) of **4** (top) compared to the first absorption measurement of the stability measurements (solid black). The height of the excitation energies (sticks) corresponds to the absolute oscillator strength $f_{osc.}$. The difference density plots (bottom) show the migration of electron density from gray (-) to green (+) during the respective excitation.

Table S6: Excitation energies $E_{exc.}$ and wavelengths $\lambda_{exc.}$, oscillator strengths $f_{osc.}$, weight W (≥15%) of the individual excitations of HOMO (H) and LUMO (L) and the description of the transition $S_n \leftarrow S_0$ of **4**.

n	$E_{exc.}$ / cm^{-1}	$\lambda_{exc.}$ / nm	$f_{osc.}$	W / %	HOMO	LUMO	Description
1	10410.5	960.6	0.002	95.0	H	L	$\pi_{phen}^* \leftarrow \pi_{AmIm}$, ($d_{Cu}$)
2	12252.7	816.1	0.0003	98.0	H	L+1	$\pi_{phen}^* \leftarrow \pi_{AmIm}$, ($d_{Cu}$)
3	16565.9	603.6	0.022	97.3	H-1	L+1	$\pi_{phen}^* \leftarrow d_{Cu}$, ($\pi_{AmIm}$)
4	16965.1	589.4	0.142	93.0	H-1	L	$\pi_{phen}^* \leftarrow d_{Cu}$, ($\pi_{AmIm}$)
12	25889.9	386.3	0.035	78.8	H-1	L+2	$\pi_{phen}^* \leftarrow d_{Cu}$, ($\pi_{AmIm}$)
14	26735.2	374.0	0.014	68.6	H-6	L	$\pi_{phen}^* \leftarrow d_{Cu}$
15	27227.8	367.3	0.077	87.0	H	L+4	$\pi_{AmIm}^* \leftarrow \pi_{AmIm}$, ($d_{Cu}$)
17	28090.3	356.0	0.051	74.2	H	L+5	$\pi_{AmIm}^* \leftarrow \pi_{AmIm}$, ($d_{Cu}$)
				21.9	H	L+6	$\pi_{AmIm}^* \leftarrow \pi_{AmIm}$, ($d_{Cu}$)
19	29210.0	342.3	0.100	22.1	H	L+5	$\pi_{AmIm}^* \leftarrow \pi_{AmIm}$, ($d_{Cu}$)
				72.3	H	L+6	$\pi_{AmIm}^* \leftarrow \pi_{AmIm}$, ($d_{Cu}$)
34	34188.0	292.5	0.355	49.8	H-1	L+5	$\pi_{AmIm}^* \leftarrow d_{Cu}$, ($\pi_{AmIm}$)
				18.0	H	L+9	$\pi_{AmIm}^* \leftarrow \pi_{AmIm}$, ($d_{Cu}$)
49	38652.4	258.7	0.097	37.2	H-2	L+4	$\pi_{AmIm}^* \leftarrow \pi_{AmIm}$, ($d_{Cu}$)
51	39494.5	253.2	0.146	50.8	H-11	L+1	$\pi_{phen}^* \leftarrow \pi_{phen}$
				17.5	H-10	L+2	$\pi_{phen}^* \leftarrow \pi_{phen}$

4.2 Compound **5** - [Cu(AmIm)(neo)]

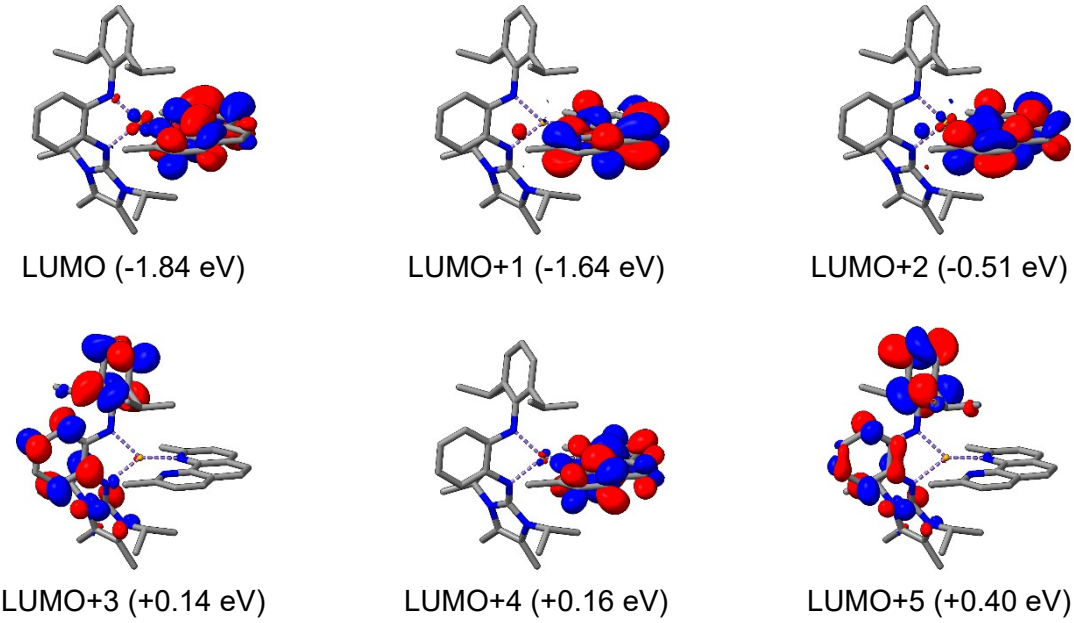

Figure S33: Molecular orbitals of **5** with their respective energies given in eV. The top half shows the lowest unoccupied molecular orbitals, while the bottom half shows the highest occupied molecular orbitals. Blue and red correspond to a negative and positive sign respectively (isosurface: ±0.035).

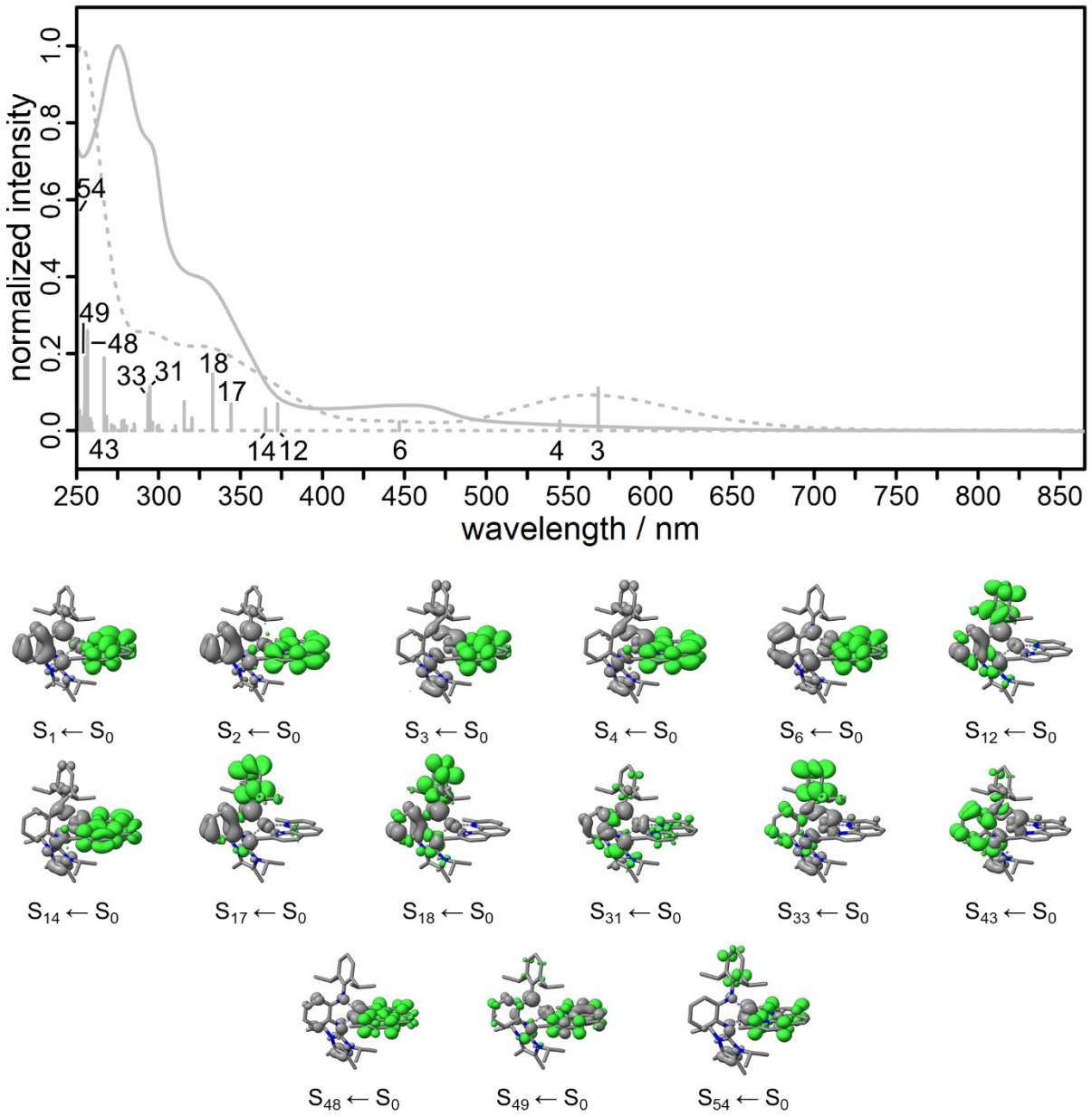

Figure S34: Normalised excitation spectrum (dotted gray) of **5** (top) *vs.* a measurement in solution (solid gray). The height of the excitation energies (sticks) corresponds to the absolute oscillator strength $f_{osc.}$. The difference density plots (bottom) show the migration of electron density from gray (-) to green (+) during the respective excitation.

Table S7: Excitation energies $E_{exc.}$ and wavelengths $\lambda_{exc.}$, oscillator strengths $f_{osc.}$, weight W (≥15%) of the individual excitations of HOMO (H) and LUMO (L) and the description of the transition $S_n \leftarrow S_0$ for **5**.

n	$E_{exc.}$ / cm^{-1}	$\lambda_{exc.}$ / nm	$f_{osc.}$	W / %	HOMO	LUMO	Description
1	11980.1	834.7	0.001	96.3	H	L	$\pi_{phen}^* \leftarrow \pi_{AmIm}$, ($d_{Cu}$)
2	14468.5	691.2	0.0006	98.4	H	L+1	$\pi_{phen}^* \leftarrow \pi_{AmIm}$, ($d_{Cu}$)
3	17598.6	568.2	0.111	92.0	H-1	L	$\pi_{phen}^* \leftarrow d_{Cu}$, ($\pi_{AmIm}$)
4	18359.3	544.7	0.025	93.6	H-1	L+1	$\pi_{phen}^* \leftarrow d_{Cu}$, ($\pi_{AmIm}$)
6	22381.3	446.8	0.023	37.1	H-3	L	$\pi_{phen}^* \leftarrow d_{Cu}$
				47.1	H-2	L	$\pi_{phen}^* \leftarrow d_{Cu}$, ($\pi_{AmIm}$)
12	26837.0	372.6	0.070	92.9	H	L+3	$\pi_{AmIm}^* \leftarrow \pi_{AmIm}$, ($d_{Cu}$)
14	27373.1	365.3	0.057	80.6	H-1	L+2	$\pi_{phen}^* \leftarrow d_{Cu}$, ($\pi_{AmIm}$)
17	29052.6	344.2	0.070	87.9	H	L+5	$\pi_{AmIm}^* \leftarrow \pi_{AmIm}$, ($d_{Cu}$)
18	30033.1	333.0	0.147	87.5	H	L+6	$\pi_{AmIm}^* \leftarrow \pi_{AmIm}$, ($d_{Cu}$)
31	33930.3	294.7	0.114	57.3	H	L+8	$\pi_{AmIm}^* \leftarrow \pi_{AmIm}$, ($d_{Cu}$)
33	34076.9	293.5	0.095	90.6	H-1	L+5	$\pi_{AmIm}^* \leftarrow d_{Cu}$, ($\pi_{AmIm}$)
43	37479.1	266.8	0.189	70.2	H-1	L+8	$\pi_{AmIm}^* \leftarrow d_{Cu}$, ($\pi_{AmIm}$)
48	38977.5	256.6	0.260	16.4	H-11	L	$\pi_{phen}^* \leftarrow \pi_{phen}$
				40.7	H-6	L+2	$\pi_{phen}^* \leftarrow d_{Cu}$
49	39197.6	255.1	0.190	29.4	H-11	L+1	$\pi_{phen}^* \leftarrow \pi_{phen}$
				17.0	H	L+14	$\pi_{AmIm}^* \leftarrow \pi_{AmIm}$, ($d_{Cu}$)
54	39889.7	250.7	0.573	21.6	H-11	L	$\pi_{phen}^* \leftarrow \pi_{phen}$
				32.3	H-6	L+2	$\pi_{phen}^* \leftarrow d_{Cu}$

4.3 Compound **6** - [Cu(AmIm)(PPh_3)]

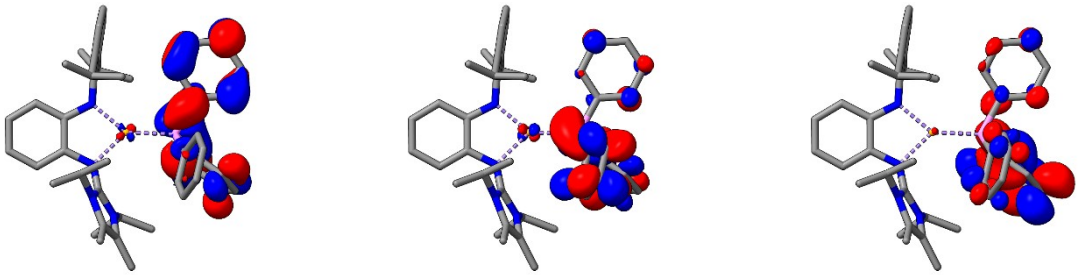

LUMO (-1.06 eV) LUMO+1 (-0.98 eV) LUMO+2 (-0.65 eV)

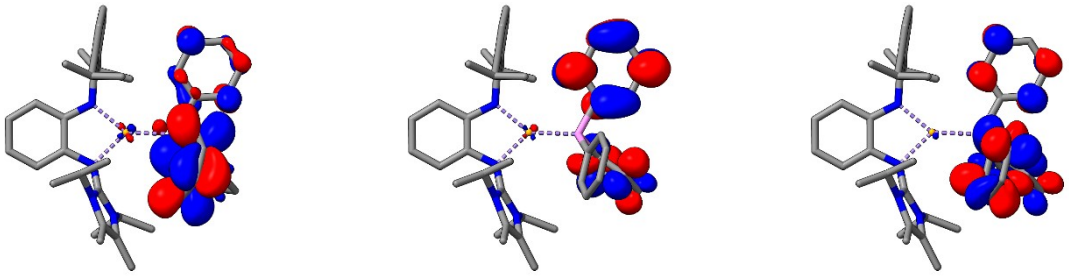

LUMO+3 (-0.57 eV) LUMO+4 (-0.33 eV) LUMO+5 (-0.19 eV)

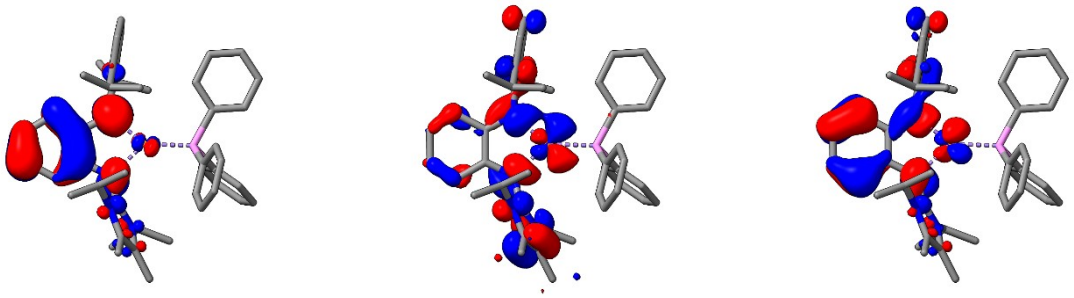

HOMO (-4.37 eV) HOMO-1 (-5.09 eV) HOMO-2 (-5.72 eV)

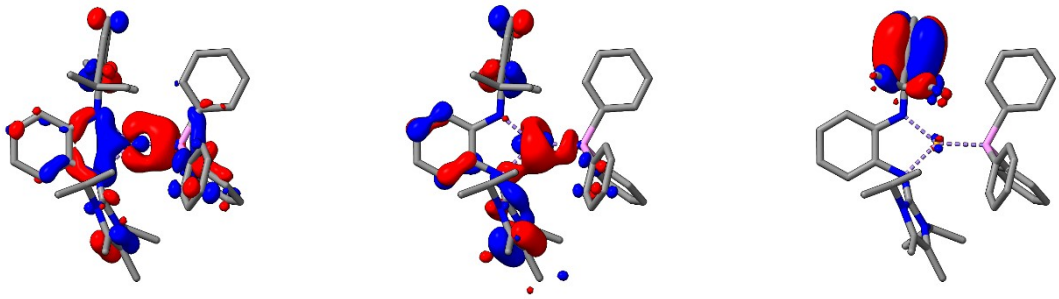

HOMO-3 (-6.27 eV) HOMO-4 (-6.33 eV) HOMO-5 (-6.51 eV)

Figure S35: Molecular orbitals of **6** with their respective energies given in eV. The top half shows the lowest unoccupied molecular orbitals, while the bottom half shows the highest occupied molecular orbitals. Blue and red correspond to a negative and positive sign respectively (isosurface: ±0.035).

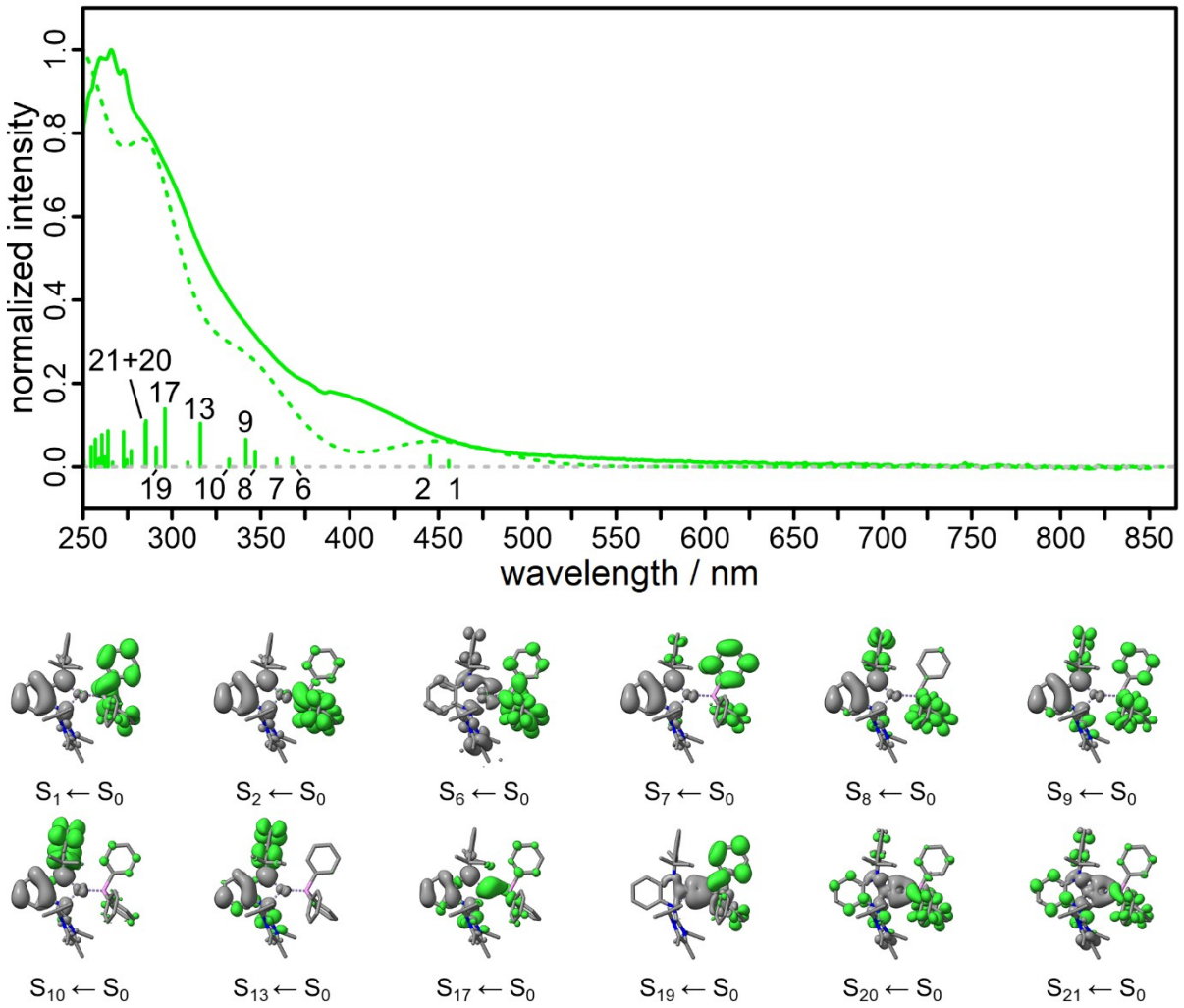

Figure S36: Normalised excitation spectrum (dotted green) of **6** (top) compared to the first absorption measurement of the stability measurements (solid green). The height of the excitation energies (sticks) corresponds to the absolute oscillator strength $f_{osc.}$. The difference density plots (bottom) show the migration of electron density from gray (-) to green (+) during the respective excitation.

Table S8: Excitation energies $E_{exc.}$ and wavelengths $\lambda_{exc.}$, oscillator strengths $f_{osc.}$, weight W (≥15%) of the individual excitations of HOMO (H) and LUMO (L) and the description of the transition $S_n \leftarrow S_0$ for **6**.

n	$E_{exc.}$ / cm^{-1}	$\lambda_{exc.}$ / nm	$f_{osc.}$	W / %	HOMO	LUMO	Description
1	21943.9	455.7	0.015	96.2	H	L	$\pi_{PPh3}^* \leftarrow \pi_{Amlm}, (d_{Cu})$
2	22454.9	445.3	0.026	95.6	H	L+1	$\pi_{PPh3}^* \leftarrow \pi_{Amlm}, (d_{Cu})$
6	27193.4	367.7	0.021	39.6	H-1	L	$\pi_{PPh3}^* \leftarrow d_{Cu}, (\pi_{Amlm})$
				55.8	H-1	L+1	$\pi_{PPh3}^* \leftarrow d_{Cu}, (\pi_{Amlm})$
7	27855.4	359.0	0.019	87.6	H	L+4	$\pi_{PPh3}^* \leftarrow \pi_{Amlm}, (d_{Cu})$
8	28830.6	346.9	0.037	43.7	H	L+5	$\pi_{PPh3}^* \leftarrow \pi_{Amlm}, (d_{Cu})$
				42.2	H	L+6	$\pi_{Amlm}^* \leftarrow \pi_{Amlm}, (d_{Cu})$
9	29273.9	341.6	0.066	48.3	H	L+5	$\pi_{PPh3}^* \leftarrow \pi_{Amlm}, (d_{Cu})$
				37.3	H	L+6	$\pi_{Amlm}^* \leftarrow \pi_{Amlm}, (d_{Cu})$
10	30101.3	332.2	0.018	73.2	H	L+7	$\pi_{Amlm}^* \leftarrow \pi_{Amlm}, (d_{Cu})$
13	31643.3	316.0	0.104	81.3	H	L+8	$\pi_{Amlm}^* \leftarrow \pi_{Amlm}, (d_{Cu})$
17	33777.1	296.1	0.139	76.1	H	L+9	$p_{Cu}, (\pi_{Amlm}^*) \leftarrow \pi_{Amlm}, (d_{Cu})$
19	34340.4	291.2	0.047	24.0	H-4	L	$\pi_{PPh3}^* \leftarrow d_{Cu}, (\pi_{Amlm})$
				60.9	H-3	L	$\pi_{PPh3}^* \leftarrow d_{Cu}, \sigma_{Cu}$
20	35021.6	285.5	0.110	15.4	H-4	L+1	$\pi_{PPh3}^* \leftarrow d_{Cu}, (\pi_{Amlm})$
				32.7	H-3	L+1	$\pi_{PPh3}^* \leftarrow d_{Cu}, \sigma_{Cu}$
				32.9	H-1	L+6	$\pi_{Amlm}^* \leftarrow d_{Cu}, (\pi_{Amlm})$
21	35088.3	285.0	0.104	27.9	H-3	L+1	$\pi_{PPh3}^* \leftarrow d_{Cu}, \sigma_{Cu}$
				48.0	H-1	L+6	$\pi_{Amlm}^* \leftarrow d_{Cu}, (\pi_{Amlm})$

4.4 Compound **7** - [Cu(AmIm)(L2)]

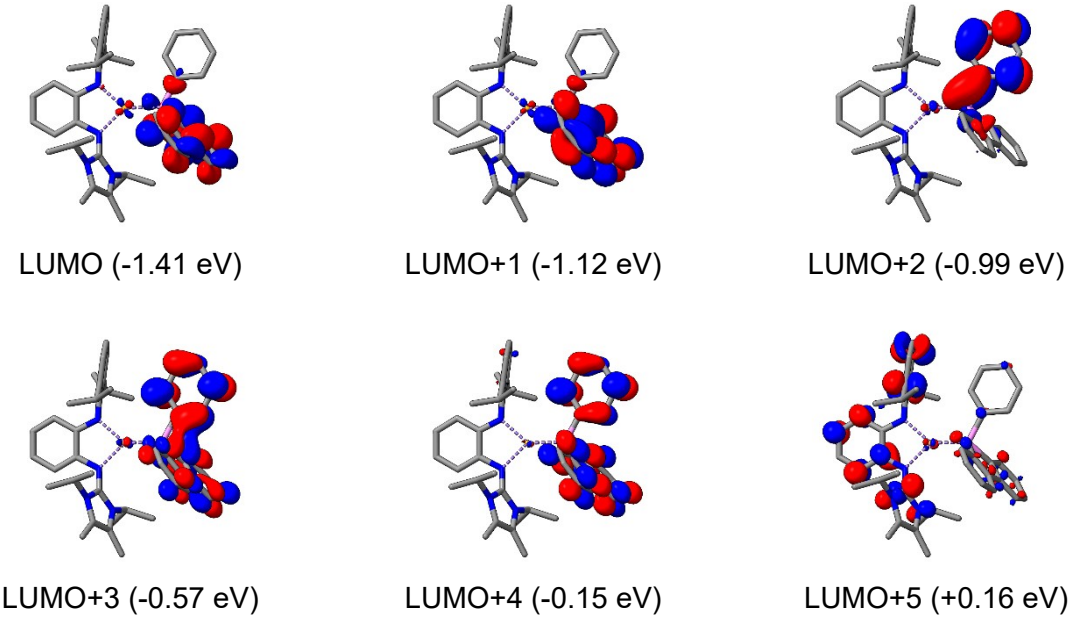

Figure S37: Molecular orbitals of **7** with their respective energies given in eV. The top half shows the lowest unoccupied molecular orbitals, while the bottom half shows the highest occupied molecular orbitals. Blue and red correspond to a negative and positive sign respectively (isosurface: ±0.035).

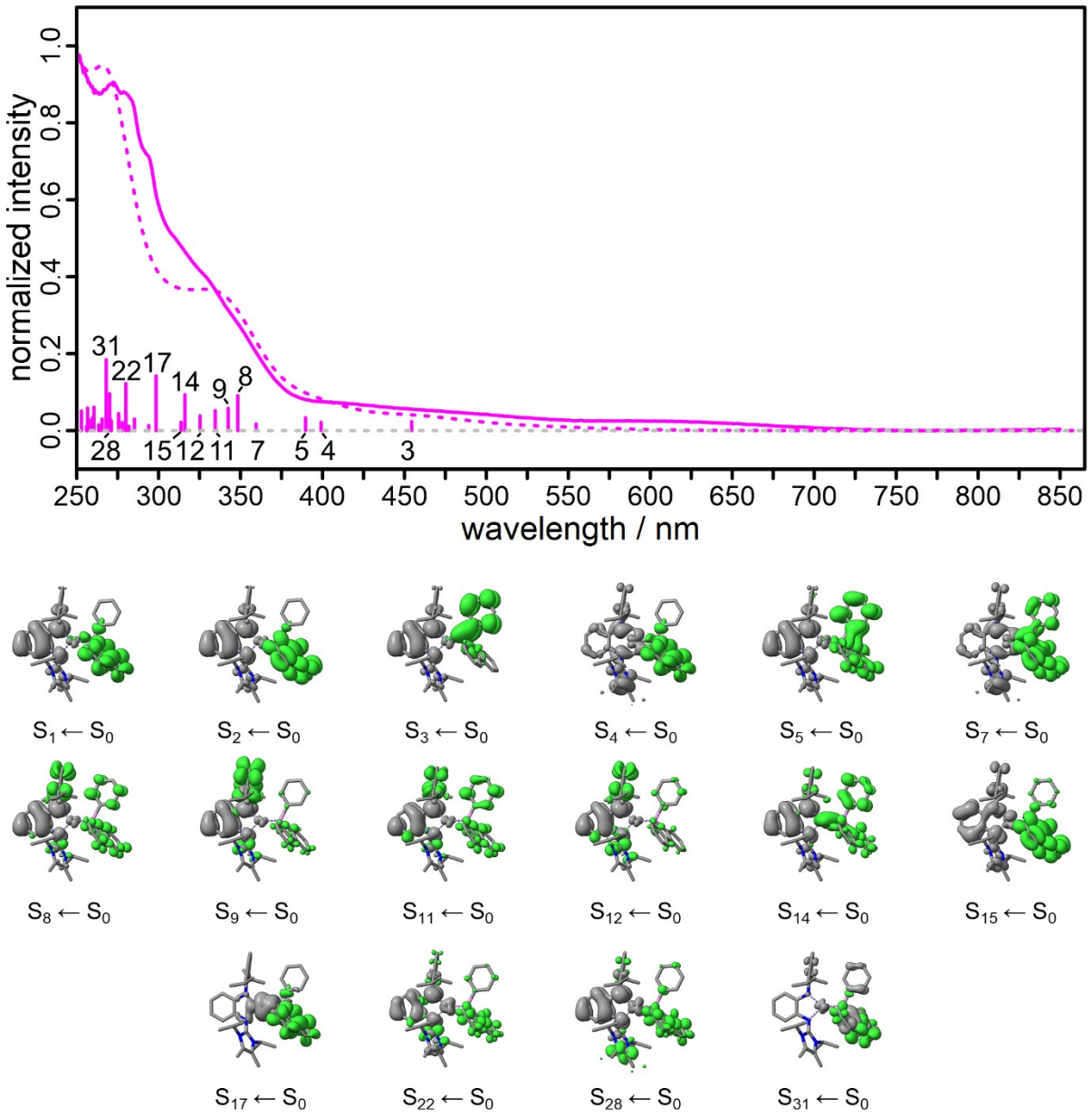

Figure S38: Normalised excitation spectrum (dotted pink) of **7** (top) compared to the first absorption measurement of the stability measurements (solid pink). The height of the excitation energies (sticks) corresponds to the absolute oscillator strength $f_{osc.}$. The difference density plots (bottom) show the migration of electron density from gray (-) to green (+) during the respective excitation.

Table S9: Excitation energies $E_{exc.}$ and wavelengths $\lambda_{exc.}$, oscillator strengths $f_{osc.}$, weight W (≥15%) of the individual excitations of HOMO (H) and LUMO (L) and the description of the transition $S_n \leftarrow S_0$ for **7**.

n	$E_{exc.}$ / cm^{-1}	$\lambda_{exc.}$ / nm	$f_{osc.}$	W / %	HOMO	LUMO	Description
1	18889.8	529.4	0.007	97.6	H	L	$\pi_{L2}^* \leftarrow \pi_{Amlm}, (d_{Cu})$
2	21460.4	466.0	0.004	97.6	H	L+1	$\pi_{L2}^* \leftarrow \pi_{Amlm}, (d_{Cu})$
3	22009.2	454.4	0.024	98.3	H	L+2	$\pi_{L2}^* \leftarrow \pi_{Amlm}, (d_{Cu})$
4	25051.7	399.2	0.022	92.3	H-1	L	$\pi_{L2}^* \leftarrow d_{Cu}, \pi_{Amlm}$
5	25663.1	389.7	0.033	95.7	H	L+3	$\pi_{L2}^* \leftarrow \pi_{Amlm}, (d_{Cu})$
7	27814.6	359.5	0.017	54.5	H-1	L+1	$\pi_{L2}^* \leftarrow d_{Cu}, \pi_{Amlm}$
				39.4	H-1	L+2	$\pi_{L2}^* \leftarrow d_{Cu}, \pi_{Amlm}$
8	28708.3	348.3	0.091	56.5	H	L+4	$\pi_{L2}^* \leftarrow \pi_{Amlm}, (d_{Cu})$
				35.0	H	L+5	$\pi_{Amlm}^* \leftarrow \pi_{Amlm}, (d_{Cu})$
9	29195.5	342.5	0.058	68.8	H	L+6	$\pi_{Amlm}^* \leftarrow \pi_{Amlm}, (d_{Cu})$
11	29883.6	334.6	0.052	23.5	H	L+4	$\pi_{L2}^* \leftarrow \pi_{Amlm}, (d_{Cu})$
				43.7	H	L+5	$\pi_{Amlm}^* \leftarrow \pi_{Amlm}, (d_{Cu})$
				21.5	H	L+6	$\pi_{Amlm}^* \leftarrow \pi_{Amlm}, (d_{Cu})$
12	30742.0	325.3	0.038	39.7	H	L+7	$p_{Cu}, \pi_{Amlm,L2}^* \leftarrow \pi_{Amlm}, (d_{Cu})$
				47.0	H	L+8	$\pi_{Amlm}^* \leftarrow \pi_{Amlm}$
14	31637.7	316.1	0.093	37.8	H	L+7	$p_{Cu}, \pi_{Amlm,L2}^* \leftarrow \pi_{Amlm}, (d_{Cu})$
				34.9	H	L+8	$\pi_{Amlm}^* \leftarrow \pi_{Amlm}$
17	33500.0	298.5	0.142	70.9	H-4	L	$\pi_{L2}^* \leftarrow d_{Cu}, \pi_{L2}$
22	35704.3	280.1	0.122	37.9	H	L+10	$\pi_{Amlm}^* \leftarrow \pi_{Amlm}, (d_{Cu})$
31	37296.3	268.1	0.184	38.7	H-6	L	$\pi_{L2}^* \leftarrow \pi_{L2}$
				25.0	H-6	L+1	$\pi_{L2}^* \leftarrow \pi_{L2}$

4.5 Compound **8** - [Cu(AmIm)(L3)]

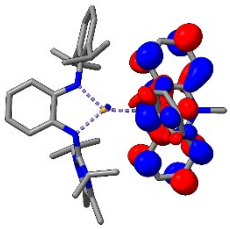

LUMO (-0.99 eV)

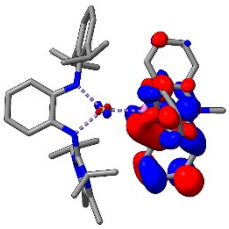

LUMO+1 (-0.80 eV)

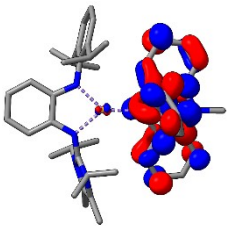

LUMO+2 (-0.56 eV)

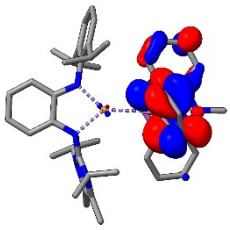

LUMO+3 (-0.44 eV)

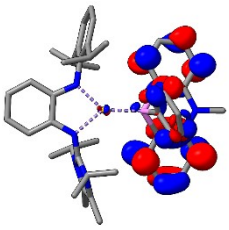

LUMO+4 (-0.21 eV)

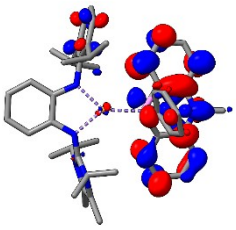

LUMO+5 (+0.02 eV)

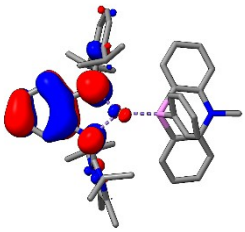

HOMO (-4.34 eV)

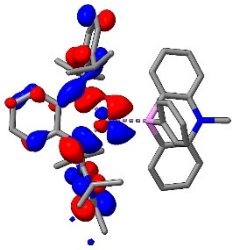

HOMO-1 (-5.12 eV)

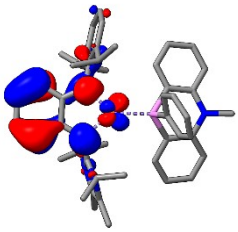

HOMO-2 (-5.78 eV)

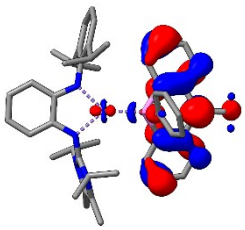

HOMO-3 (-5.90 eV)

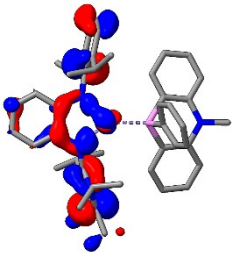

HOMO-4 (-6.32 eV)

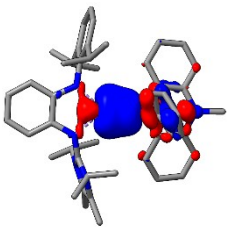

HOMO-5 (-6.49 eV)

Figure S39: Molecular orbitals of **8** with their respective energies given in eV. The top half shows the lowest unoccupied molecular orbitals, while the bottom half shows the highest occupied molecular orbitals. Blue and red correspond to a negative and positive sign respectively (isosurface: ±0.035).

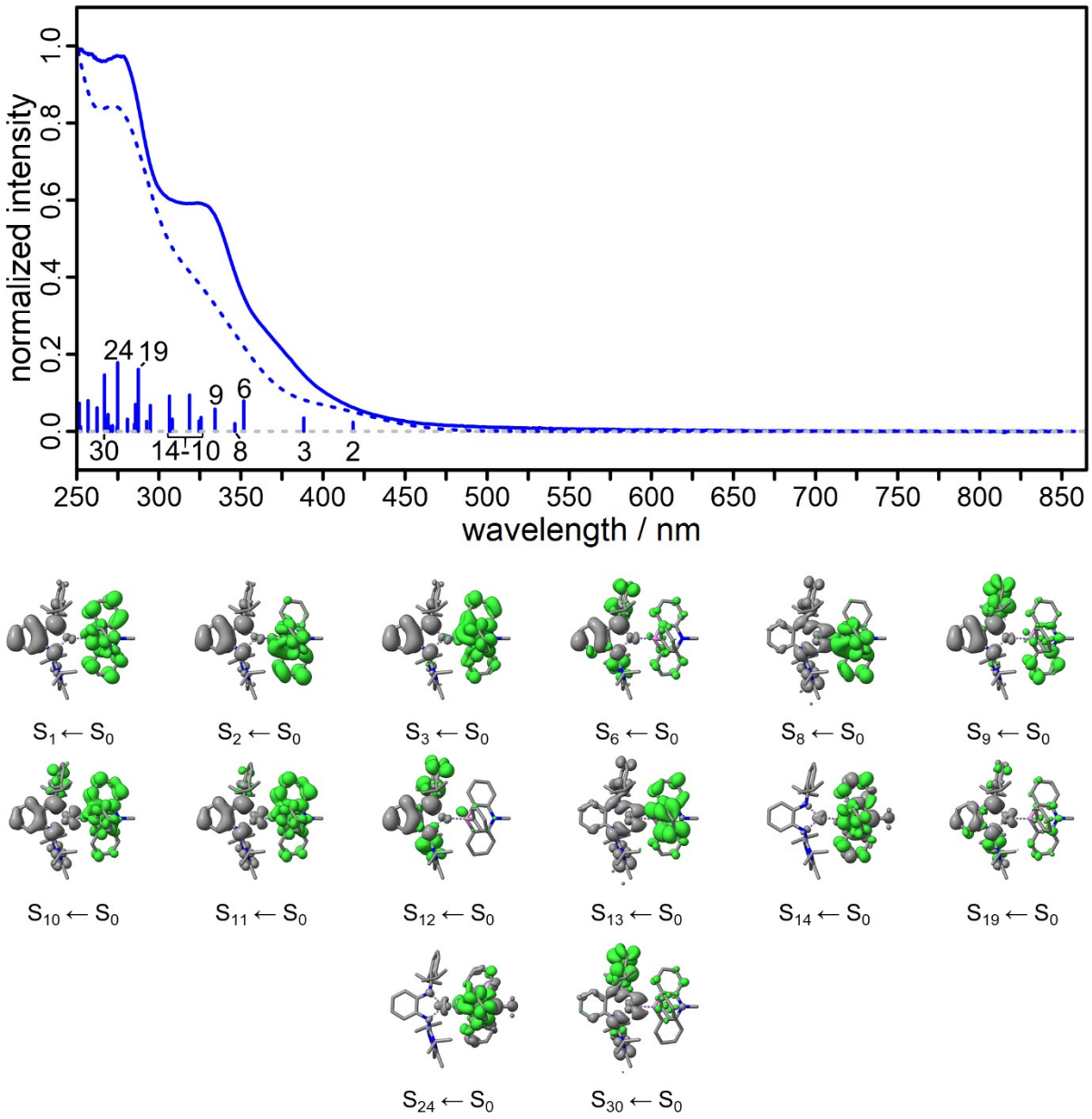

Figure S40: Normalised excitation spectrum (dotted blue) of **8** (top) compared to the first absorption measurement of the stability measurements (solid blue). The height of the excitation energies (sticks) corresponds to the absolute oscillator strength $f_{osc.}$.. The difference density plots (bottom) show the migration of electron density from gray (-) to green (+) during the respective excitation.

Table S10: Excitation energies $E_{exc.}$ and wavelengths $\lambda_{exc.}$, oscillator strengths $f_{osc.}$, weight W (≥15%) of the individual excitations of HOMO (H) and LUMO (L) and the description of the transition $S_n \leftarrow S_0$ for **8**.

n	$E_{exc.}$ / cm^{-1}	$\lambda_{exc.}$ / nm	$f_{osc.}$	W / %	HOMO	LUMO	Description
1	22382.6	446.8	0.0004	99.3	H	L	$\pi_{L3}^* \leftarrow \pi_{AmIm}$, (d_{Cu})
2	23908.8	418.3	0.024	98.2	H	L+1	$\pi_{L3}^* \leftarrow \pi_{AmIm}$, (d_{Cu})
3	25753.9	388.3	0.035	95.5	H	L+2	$\pi_{L3}^* \leftarrow \pi_{AmIm}$, (d_{Cu})
6	28433.8	351.7	0.079	24.4	H	L+4	$\pi_{L3}^* \leftarrow \pi_{AmIm}$, (d_{Cu})
				58.1	H	L+6	$\pi_{AmIm}^* \leftarrow \pi_{AmIm}$, (d_{Cu})
8	28878.3	346.3	0.020	85.1	H-1	L+1	$\pi_{L3}^* \leftarrow d_{Cu}$, π_{AmIm}
9	29923.8	334.2	0.058	51.0	H	L+5	$\pi_{L3}^* \leftarrow \pi_{AmIm}$, (d_{Cu})
				34.4	H	L+7	$\pi_{AmIm}^* \leftarrow \pi_{AmIm}$, (d_{Cu})
10	30702.1	325.7	0.036	44.1	H-1	L+2	$\pi_{L3}^* \leftarrow d_{Cu}$, π_{AmIm}
				31.5	H	L+7	$\pi_{AmIm}^* \leftarrow \pi_{AmIm}$, (d_{Cu})
11	30816.9	324.5	0.027	34.3	H-1	L+2	$\pi_{L3}^* \leftarrow d_{Cu}$, π_{AmIm}
				22.1	H	L+5	$\pi_{L3}^* \leftarrow \pi_{AmIm}$, (d_{Cu})
				20.3	H	L+7	$\pi_{AmIm}^* \leftarrow \pi_{AmIm}$, (d_{Cu})
12	31381.1	318.7	0.094	87.5	H	L+8	$\pi_{AmIm}^* \leftarrow \pi_{AmIm}$, (d_{Cu})
13	32450.2	308.2	0.032	87.8	H-1	L+3	$\pi_{L3}^* \leftarrow d_{Cu}$, π_{AmIm}
14	32625.5	306.5	0.092	88.4	H-3	L	$\pi_{L3}^* \leftarrow \pi_{L3}$
19	34785.9	287.5	0.161	26.5	H-1	L+6	$\pi_{AmIm}^* \leftarrow d_{Cu}$, π_{AmIm}
				45.0	H	L+10	$\pi_{AmIm,L3}^*, p_{Cu} \leftarrow \pi_{AmIm}$, (d_{Cu})
24	36382.3	274.9	0.178	84.5	H-3	L+2	$\pi_{L3}^* \leftarrow \pi_{L3}$
30	37461.6	266.9	0.146	82.6	H-1	L+7	$\pi_{AmIm}^* \leftarrow d_{Cu}$, π_{AmIm}

4.6 Compound **9** - [Cu(AmIm)(L4)]

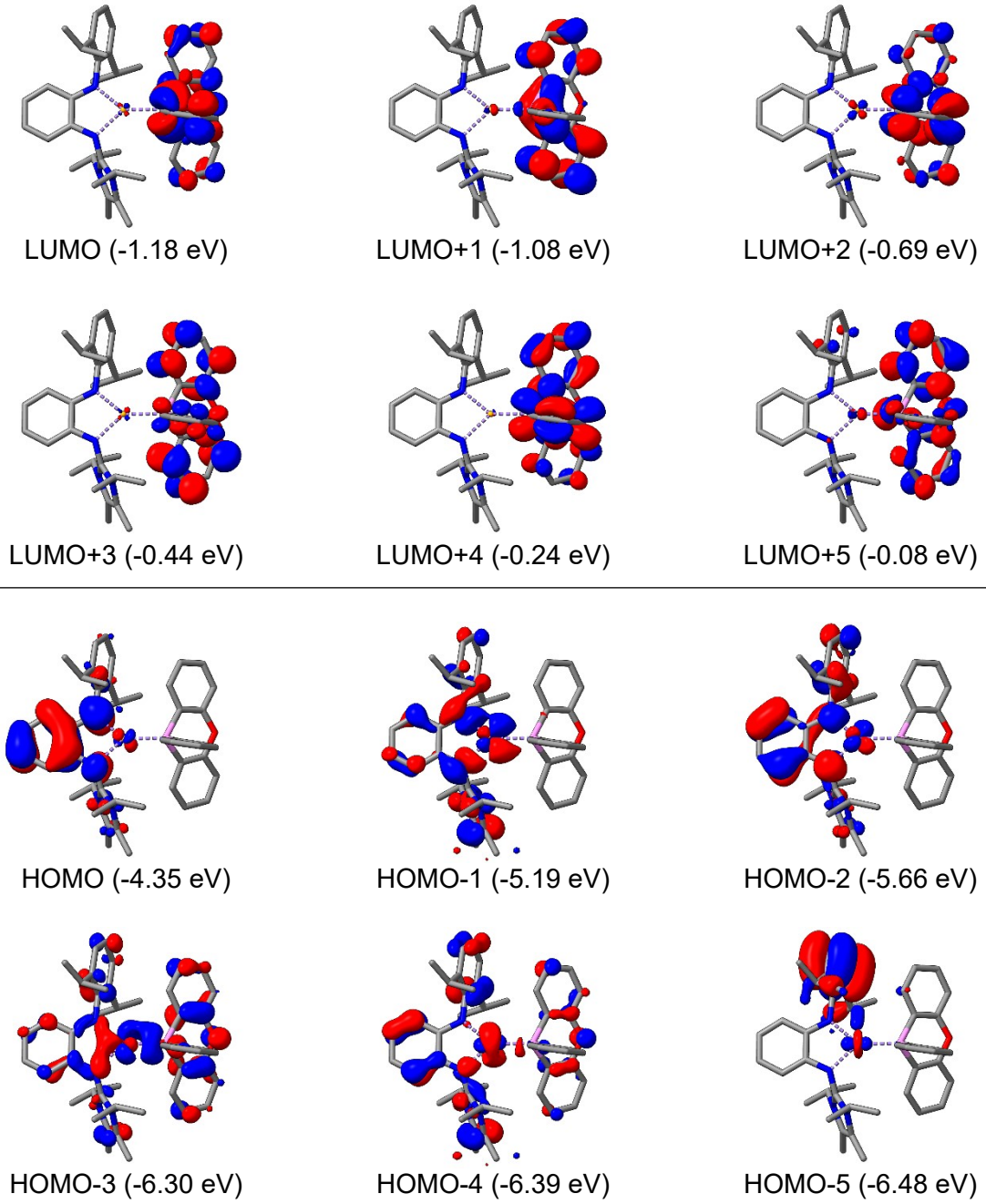

Figure S41: Molecular orbitals of **9** with their respective energies given in eV. The top half shows the lowest unoccupied molecular orbitals, while the bottom half shows the highest occupied molecular orbitals. Blue and red correspond to a negative and positive sign respectively (isosurface: ±0.035).

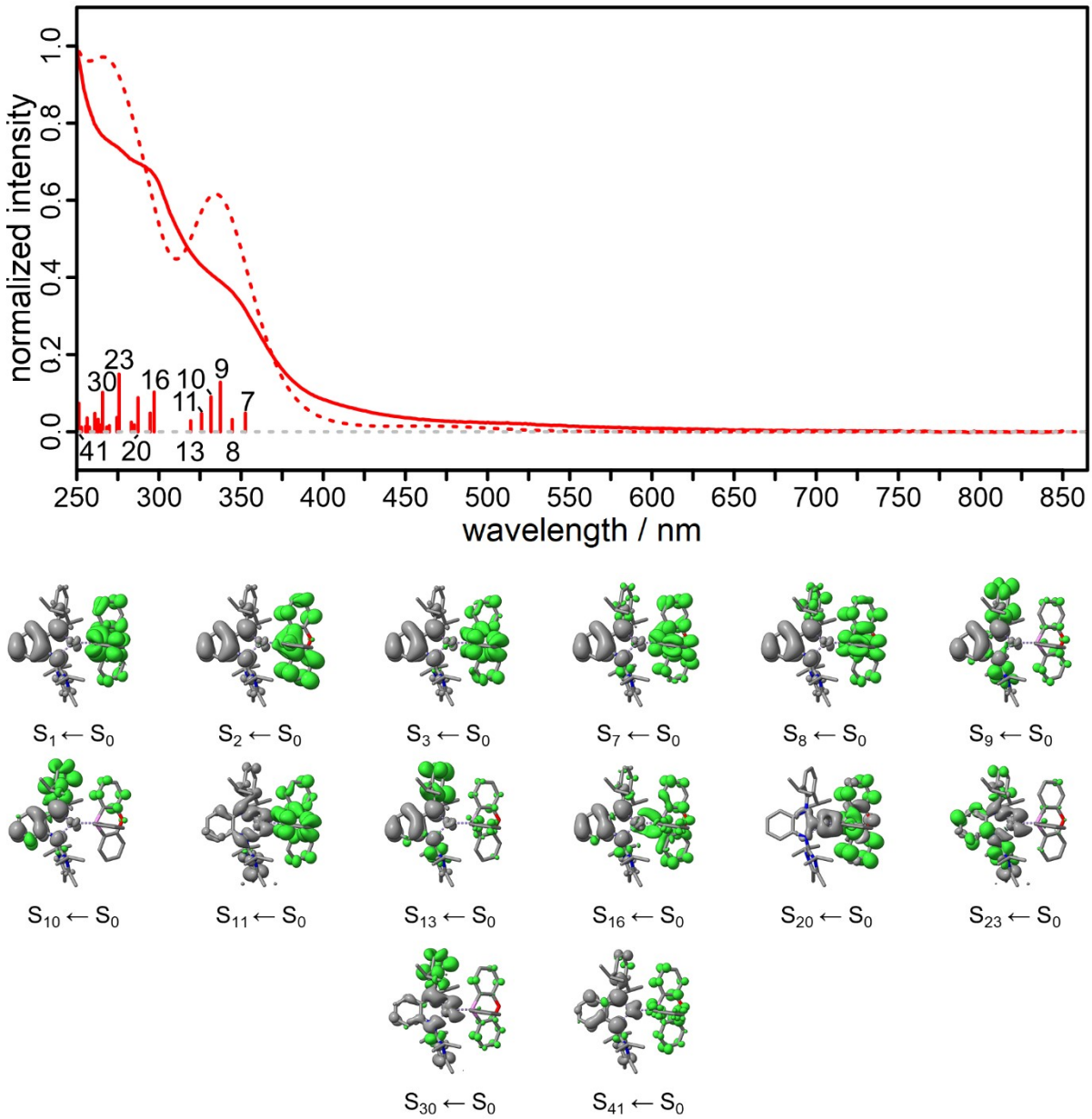

Figure S42: Normalised excitation spectrum (dotted red) of **9** (top) compared to the first absorption measurement of the stability measurements (solid red). The height of the excitation energies (sticks) corresponds to the absolute oscillator strength $f_{osc.}$.. The difference density plots (bottom) show the migration of electron density from gray (-) to green (+) during the respective excitation.

Table S11: Excitation energies $E_{exc.}$ and wavelengths $\lambda_{exc.}$, oscillator strengths $f_{osc.}$, weight W (≥15%) of the individual excitations of HOMO (H) and LUMO (L) and the description of the transition $S_n \leftarrow S_0$ for **9**.

n	$E_{exc.}$ / cm^{-1}	$\lambda_{exc.}$ / nm	$f_{osc.}$	W / %	HOMO	LUMO	Description
1	20857.8	479.4	0.002	99.1	H	L	$\pi_{L4}^* \leftarrow \pi_{Amlm}, (d_{Cu})$
2	21468.1	465.8	0.006	98.8	H	L+1	$\pi_{L4}^* \leftarrow \pi_{Amlm}, (d_{Cu})$
3	24761.5	403.9	0.007	98.3	H	L+2	$\pi_{L4}^* \leftarrow \pi_{Amlm}, (d_{Cu})$
7	28360.0	352.6	0.048	73.0	H	L+4	$\pi_{L4}^* \leftarrow \pi_{Amlm}, (d_{Cu})$
				16.4	H	L+5	$\pi_{L4}^* \leftarrow \pi_{Amlm}, (d_{Cu})$
8	29020.5	344.6	0.031	22.7	H	L+4	$\pi_{L4}^* \leftarrow \pi_{Amlm}, (d_{Cu})$
				64.7	H	L+5	$\pi_{L4}^* \leftarrow \pi_{Amlm}, (d_{Cu})$
9	29635.9	337.4	0.128	66.7	H	L+6	$\pi_{Amlm}^* \leftarrow \pi_{Amlm}, (d_{Cu})$
				17.3	H	L+7	$\pi_{Amlm}^* \leftarrow \pi_{Amlm}, (d_{Cu})$
10	30150.2	331.7	0.090	23.6	H	L+6	$\pi_{Amlm}^* \leftarrow \pi_{Amlm}, (d_{Cu})$
				63.8	H	L+7	$\pi_{Amlm}^* \leftarrow \pi_{Amlm}, (d_{Cu})$
11	30680.9	325.9	0.047	92.0	H-1	L+2	$\pi_{L4}^* \leftarrow d_{Cu}, \pi_{Amlm}$
13	31322.4	319.3	0.028	82.8	H	L+8	$\pi_{Amlm}^* \leftarrow \pi_{Amlm}, (d_{Cu})$
16	33658.0	297.1	0.103	84.3	H	L+9	$p_{Cu}, \pi_{Amlm,L4}^* \leftarrow \pi_{Amlm}, (d_{Cu})$
20	34807.1	287.3	0.088	17.2	H-4	L+1	$\pi_{L4}^* \leftarrow d_{Cu}, \pi_{Amlm,L4}$
				71.3	H-3	L+1	$\pi_{L4}^* \leftarrow d_{Cu}, \pi_{Amlm,L4}$
23	36277.5	275.7	0.149	83.4	H-1	L+6	$\pi_{Amlm}^* \leftarrow d_{Cu}, \pi_{Amlm}$
30	37637.9	265.7	0.102	43.8	H-1	L+7	$\pi_{Amlm}^* \leftarrow d_{Cu}, \pi_{Amlm}$
41	39789.9	251.3	0.073	30.7	H-2	L+5	$\pi_{L4}^* \leftarrow d_{Cu}, \pi_{Amlm}$
				24.7	H	L+14	$\pi_{Amlm}^* \leftarrow \pi_{Amlm}, (d_{Cu})$

4.7 Compound **10** - [Cu(AmIm)(L5)]

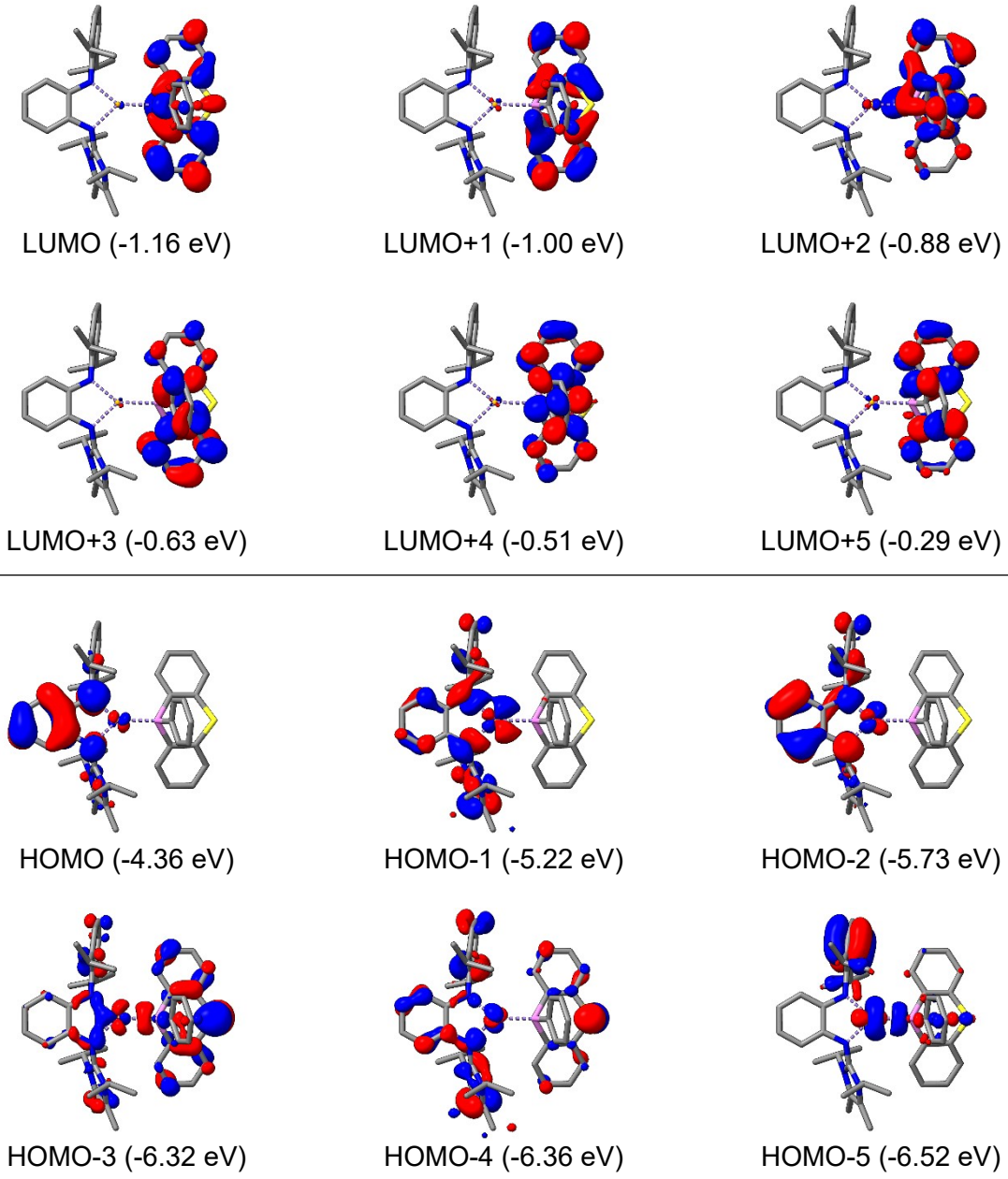

Figure S43: Molecular orbitals of **10** with their respective energies given in eV. The top half shows the lowest unoccupied molecular orbitals, while the bottom half shows the highest occupied molecular orbitals. Blue and red correspond to a negative and positive sign respectively (isosurface: ±0.035).

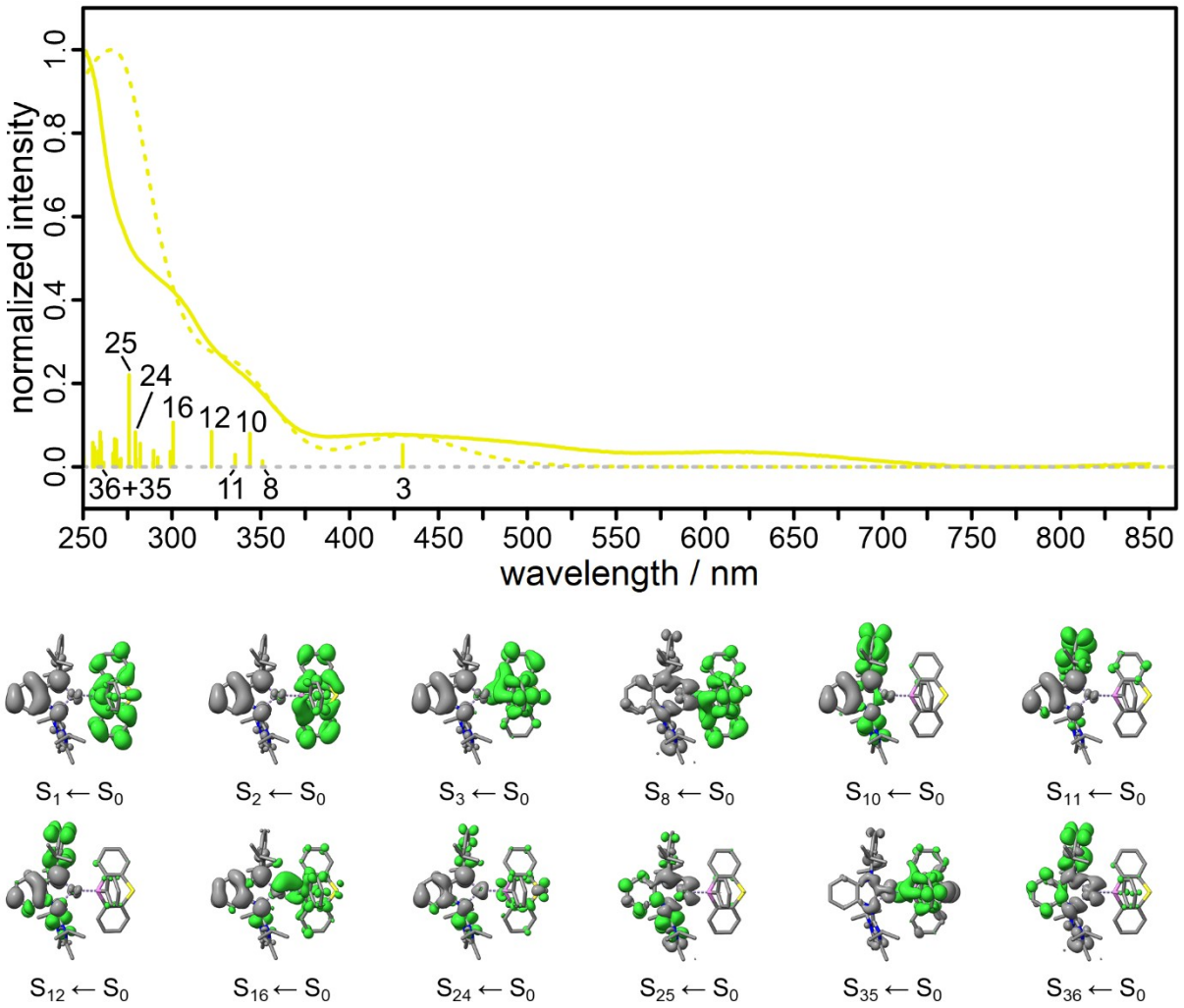

Figure S44: Normalised excitation spectrum (dotted yellow) of **10** (top) compared to the first absorption measurement of the stability measurements (solid yellow). The height of the excitation energies (sticks) corresponds to the absolute oscillator strength $f_{osc.}$. The difference density plots (bottom) show the migration of electron density from gray (-) to green (+) during the respective excitation.

Table S12: Excitation energies $E_{exc.}$ and wavelengths $\lambda_{exc.}$, oscillator strengths $f_{osc.}$, weight W (≥15%) of the individual excitations of HOMO (H) and LUMO (L) and the description of the transition $S_n \leftarrow S_0$ for **10**.

n	$E_{exc.}$ / cm^{-1}	$\lambda_{exc.}$ / nm	$f_{osc.}$	W / %	HOMO	LUMO	Description
1	21215.8	471.3	0.004	99.3	H	L	$\pi_{L5}^* \leftarrow \pi_{Amlm}$, (d_{Cu})
2	22536.4	443.7	0.002	98.6	H	L+1	$\pi_{L5}^* \leftarrow \pi_{Amlm}$, (d_{Cu})
3	23263.5	429.9	0.053	97.7	H	L+2	$\pi_{L5}^* \leftarrow \pi_{Amlm}$, (d_{Cu})
8	28488.7	351.0	0.014	51.6	H-1	L+1	$\pi_{L5}^* \leftarrow d_{Cu}$, π_{Amlm}
				33.4	H-1	L+2	$\pi_{L5}^* \leftarrow d_{Cu}$, π_{Amlm}
10	29077.8	343.9	0.080	56.0	H	L+6	$\pi_{Amlm}^* \leftarrow \pi_{Amlm}$, (d_{Cu})
				34.6	H	L+7	$\pi_{Amlm}^* \leftarrow \pi_{Amlm}$, (d_{Cu})
11	29801.1	335.6	0.029	35.3	H	L+6	$\pi_{Amlm}^* \leftarrow \pi_{Amlm}$, (d_{Cu})
				58.4	H	L+7	$\pi_{Amlm}^* \leftarrow \pi_{Amlm}$, (d_{Cu})
12	31028.6	322.3	0.084	87.1	H	L+8	$\pi_{Amlm}^* \leftarrow \pi_{Amlm}$, (d_{Cu})
16	33256.8	300.7	0.107	56.1	H	L+9	$\pi_{Amlm,L5}^*, p_P \leftarrow \pi_{Amlm}$, (d_{Cu})
				18.4	H	L+10	$\pi_{Amlm,L5}^*, p_P \leftarrow \pi_{Amlm}$, (d_{Cu})
24	35790.9	279.4	0.083	19.1	H	L+11	$\pi_{Amlm,L5}^* \leftarrow \pi_{Amlm}$, (d_{Cu})
				17.0	H	L+12	$\pi_{Amlm,L5}^* \leftarrow \pi_{Amlm}$, (d_{Cu})
				21.5	H	L+13	$\pi_{Amlm}^* \leftarrow \pi_{Amlm}$, (d_{Cu})
25	36248.3	275.9	0.220	67.6	H-1	L+6	$\pi_{Amlm}^* \leftarrow d_{Cu}$, π_{Amlm}
35	38426.1	260.2	0.060	49.5	H-4	L+2	$\pi_{L5}^* \leftarrow \pi_{Amlm,L5}$, d_{Cu}
36	38521.2	259.6	0.083	74.2	H-1	L+8	$\pi_{Amlm}^* \leftarrow d_{Cu}$, π_{Amlm}

5. UV/vis and Emission Spectroscopy

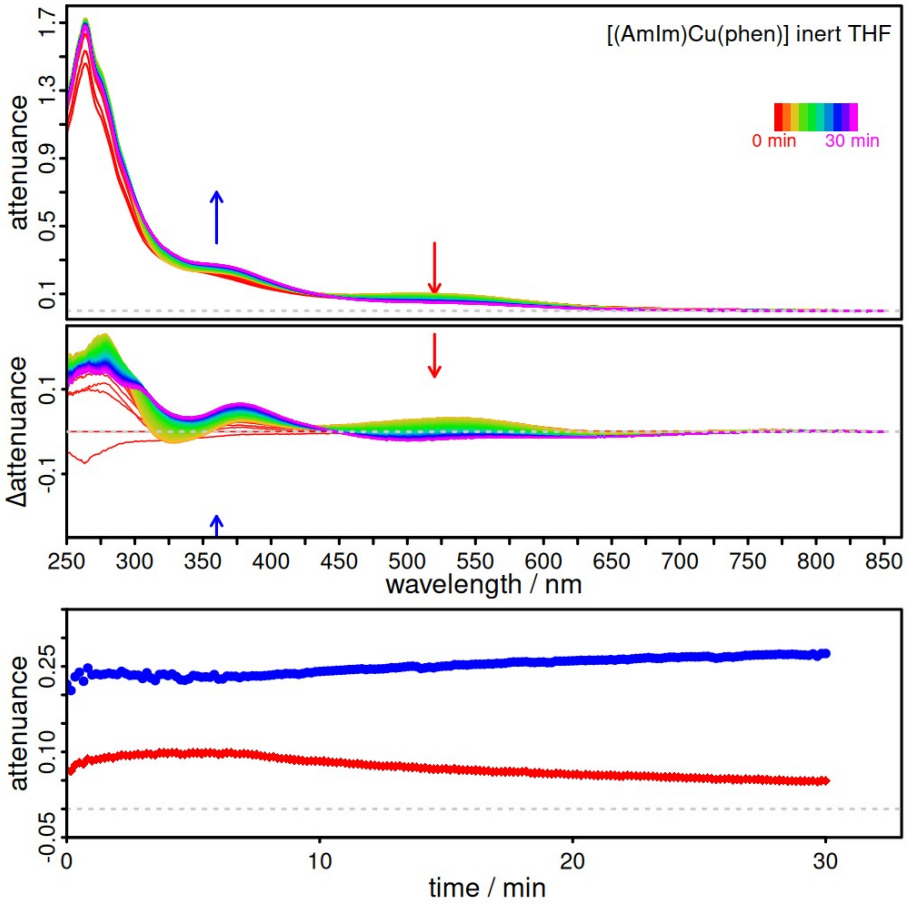

Figure S45: Steady-state absorption of **4** in inert tetrahydrofuran over time. The spectrum (top) over time and its associated spectral changes (middle) are shown. Kinetics (bottom) at 520 nm (red) and 360 nm (blue) are shown.

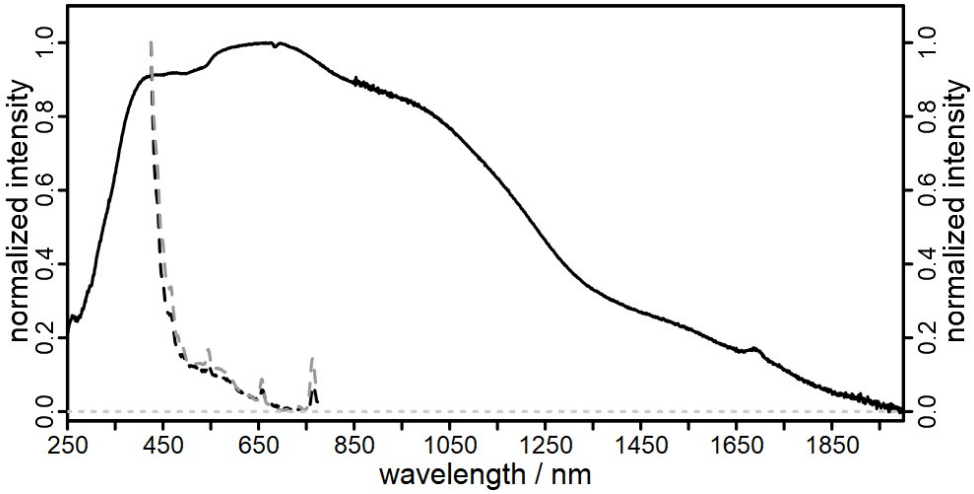

Figure S46: Solid-state steady-state absorption (solid black) and uncorrected emission ($\lambda_{exc.}$ = 400 nm, dashed black) of **4** in KBr pellet form. The absorption was measured *vs*. the pure KBr pellet and the emission of the cuvette window with a pure KBr pellet is shown dashed in gray. No emission was observed at the given excitation wavelength at room temperature.

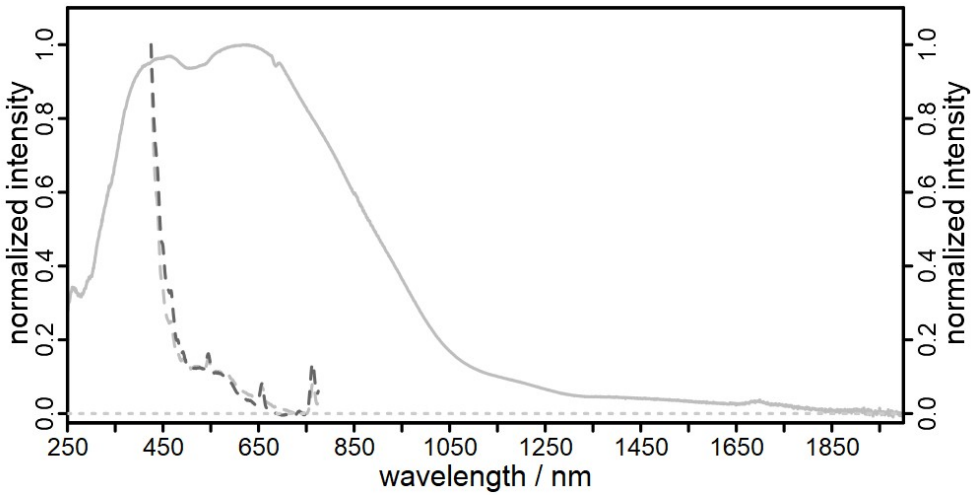

Figure S47: Solid-state steady-state absorption (solid gray) and uncorrected emission ($\lambda_{exc.}$ = 400 nm, dashed gray) of **5** in KBr pellet form. The absorption was measured *vs*. the pure KBr pellet and the emission of the cuvette window with a pure KBr pellet is shown dashed in dark gray. No emission was observed at the given excitation wavelength at room temperature.

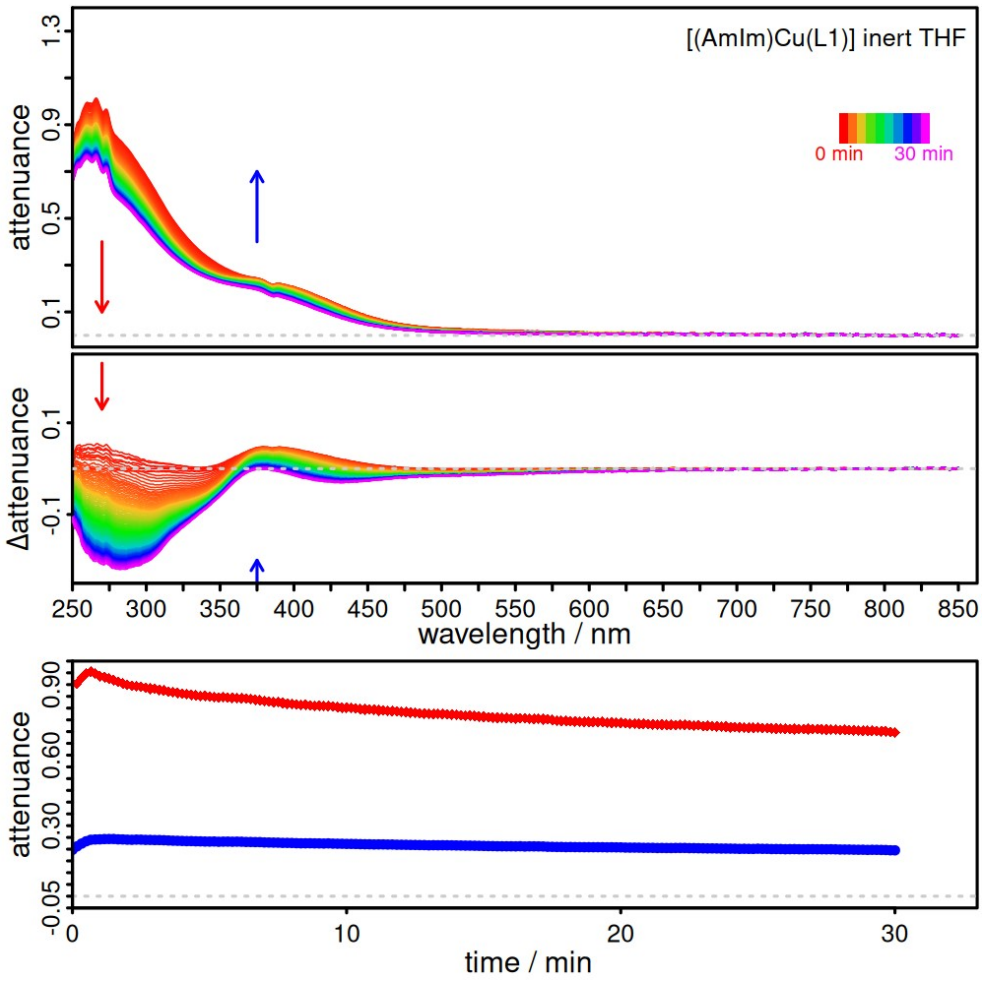

Figure S48: Steady-state absorption of **6** in inert tetrahydrofuran over time. The spectrum (top) over time and its associated spectral changes (middle) are shown. Kinetics (bottom) at 270 nm (red) and 375 nm (blue) are shown.

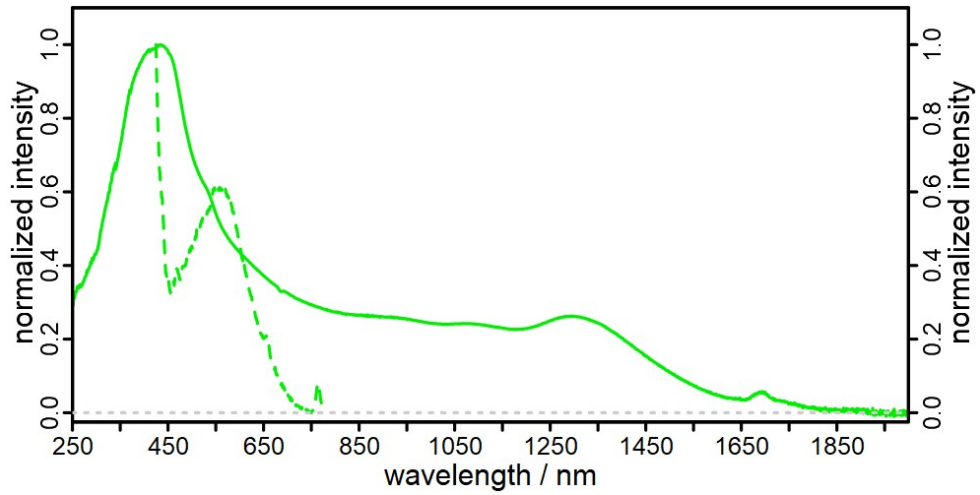

Figure S49: Solid-state steady-state absorption (solid) and uncorrected emission ($\lambda_{exc.}$ = 400 nm, dashed) of **6**.

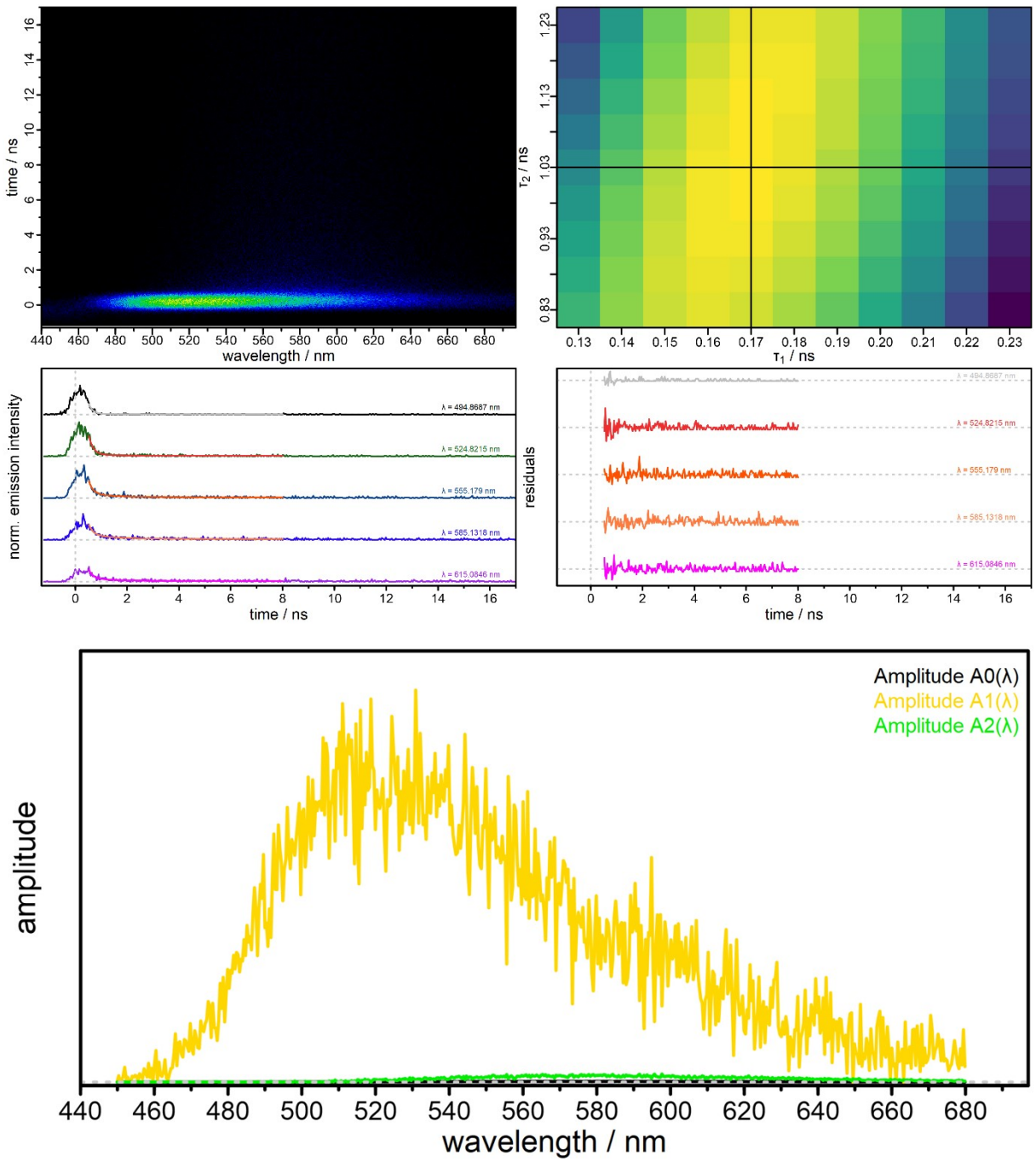

Figure S50: Time-resolved measurement ($\lambda_{exc.}$ = 400 nm) of the KBr solid-state luminescence of **6** showing the streak image (top left), the residual sum of squares summed up over the fitted wavelengths (top right), yellow lowest and purple highest. Selected kinetics (middle left, offset for visual clarity) with biexponential decays and the residuals of the fits with lowest residual sum of squares (middle right, offset for visual clarity). The biexponential fit has the following lifetimes: τ_1 = 0.17 ns and τ_2 = 1.03 ns. The decay-associated spectrum (bottom) shows the amplitude distribution of the lifetimes at each wavelength. The DAS of τ_1 shows a peak at 523.8 nm and the DAS for τ_2 at 582.8 nm.

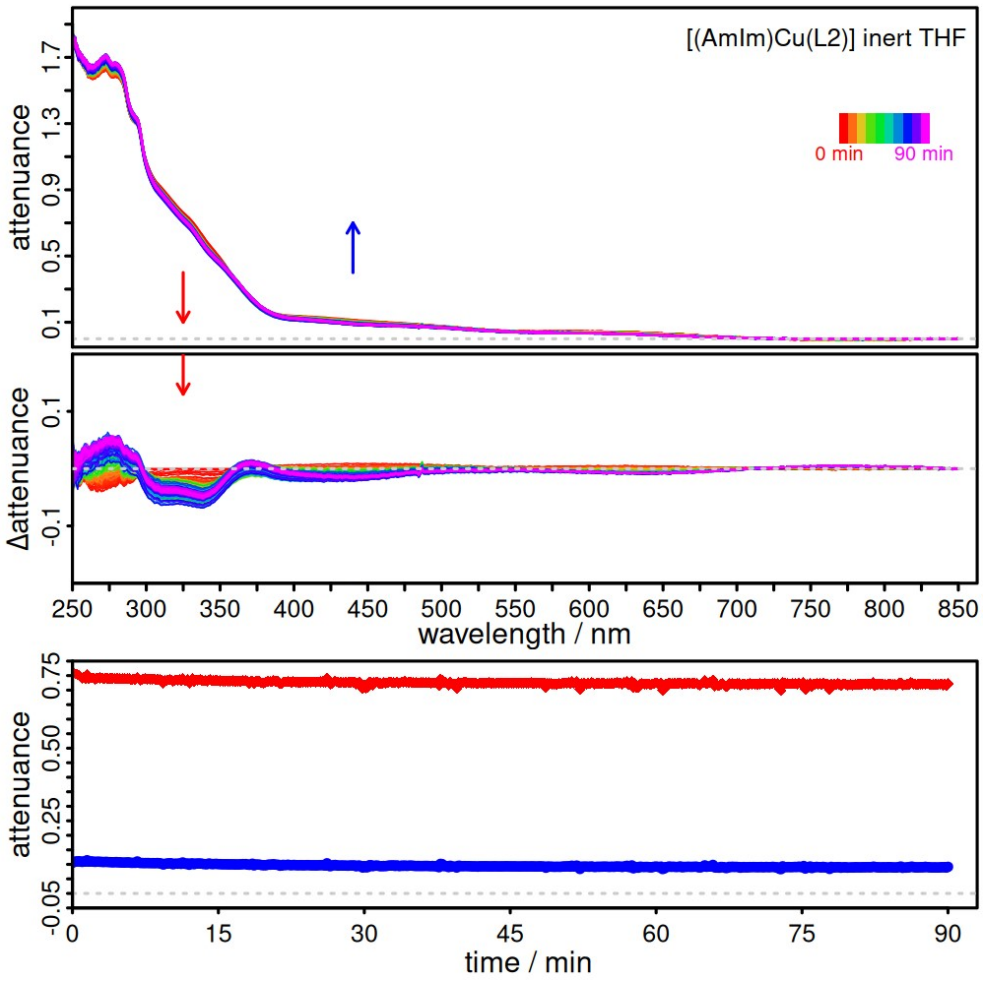

Figure S51: Steady-state absorption of **7** in inert tetrahydrofuran over time. The spectrum (top) over time and its associated spectral changes (middle) are shown. Kinetics (bottom) at 325 nm (red) and 440 nm (blue) are shown.

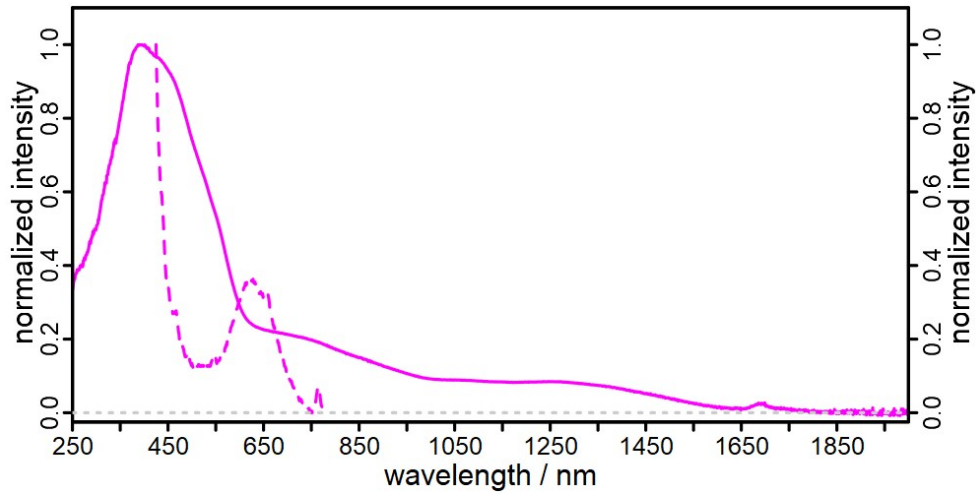

Figure S52: Normalised Solid-state steady-state absorption *vs.* KBr (solid) and uncorrected emission ($\lambda_{exc.}$ = 400 nm, dotted) of **7**.

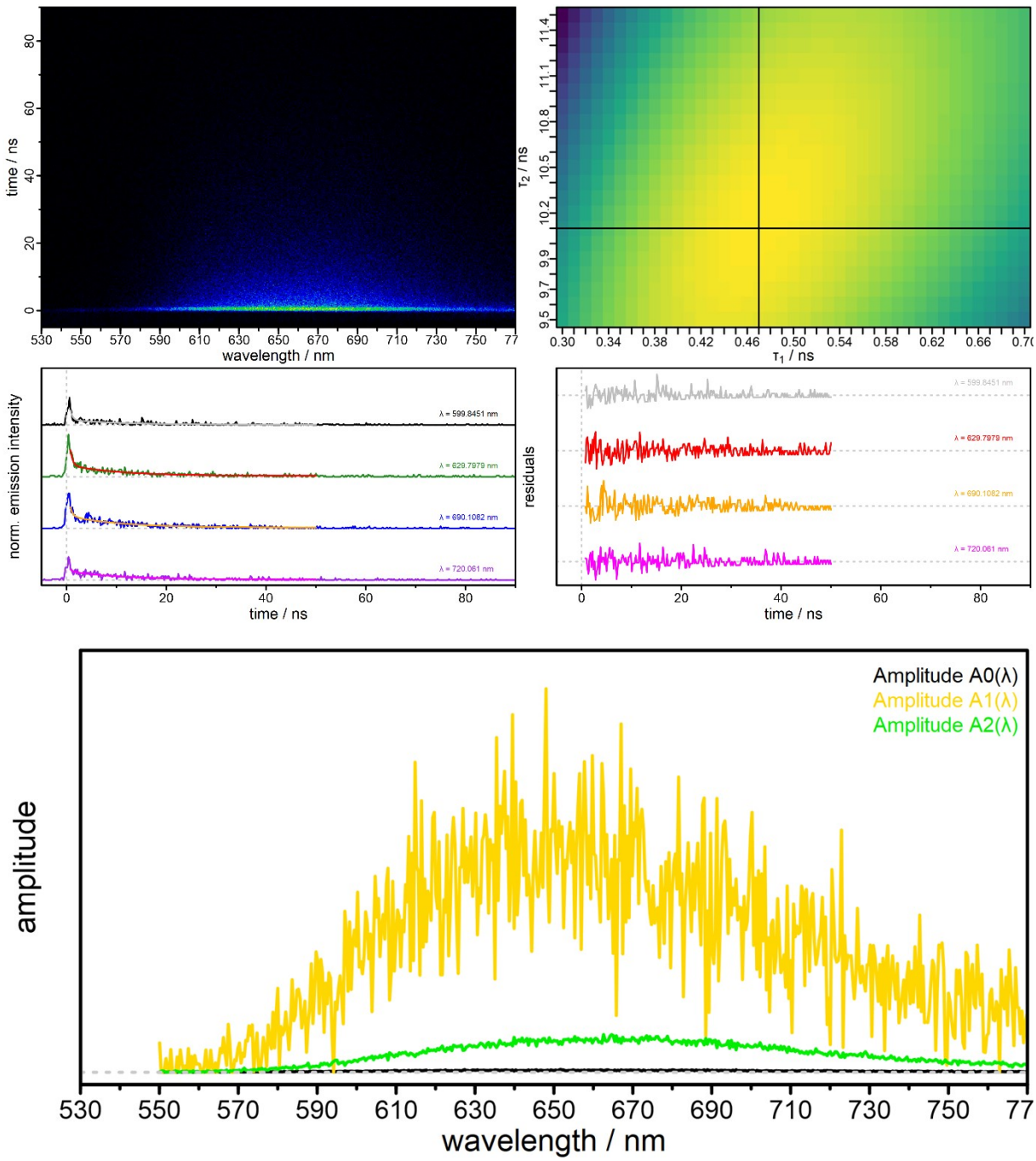

Figure S53: Time-resolved measurement ($\lambda_{exc.}$ = 400 nm) of the KBr solid-state luminescence of **7** showing the streak image (top left), the residual sum of squares summed up over the fitted wavelengths (top right), yellow lowest and purple highest. Selected kinetics (middle left, offset for visual clarity) with biexponential decays and the residuals of the fits with lowest residual sum of squares (middle right, offset for visual clarity). The biexponential fit has the following lifetimes: τ_1 = 0.47 ns and τ_2 = 10.1 ns. The decay-associated spectrum (bottom) shows the amplitude distribution of the lifetimes at each wavelength. The DAS of τ_1 shows a peak at 657.2 nm and the DAS for τ_2 at 665.6 nm.

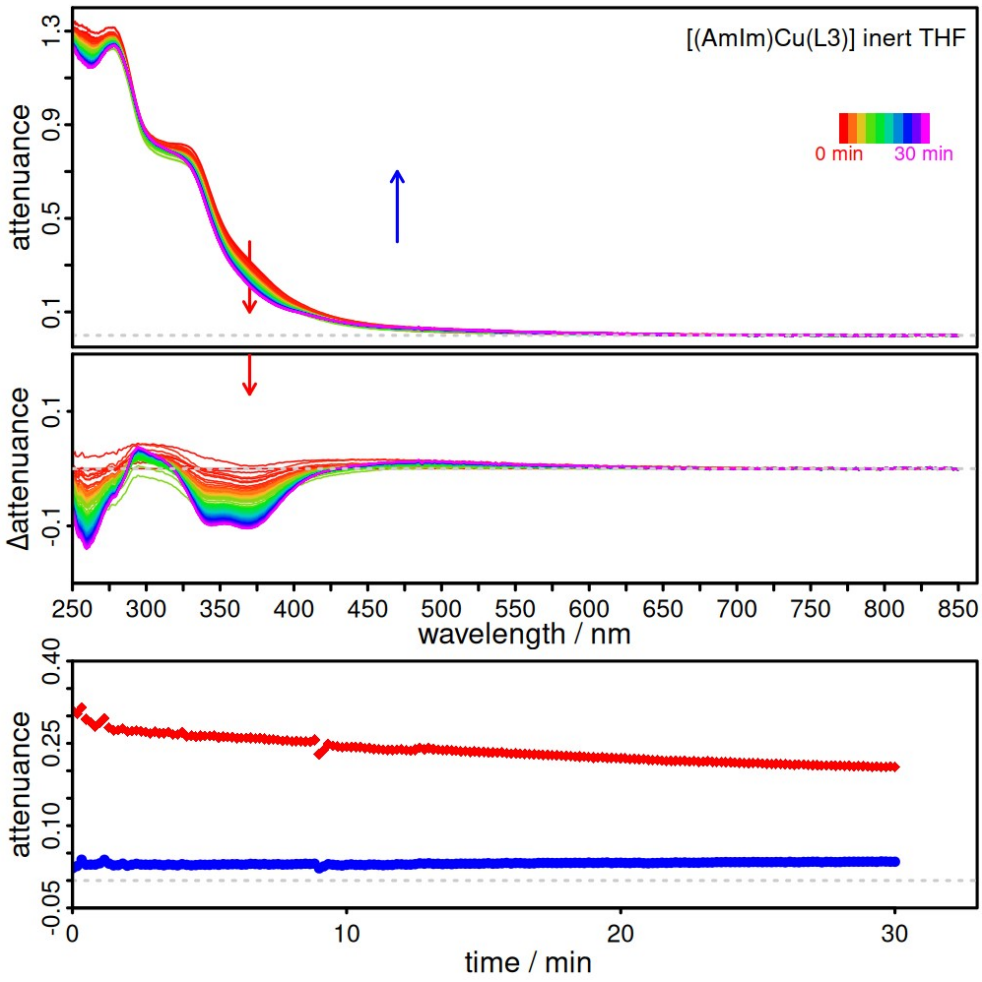

Figure S54: Steady-state absorption of **8** in inert tetrahydrofuran over time. The spectrum (top) over time and its associated spectral changes (middle) are shown. Kinetics (bottom) at 370 nm (red) and 470 nm (blue) are shown.

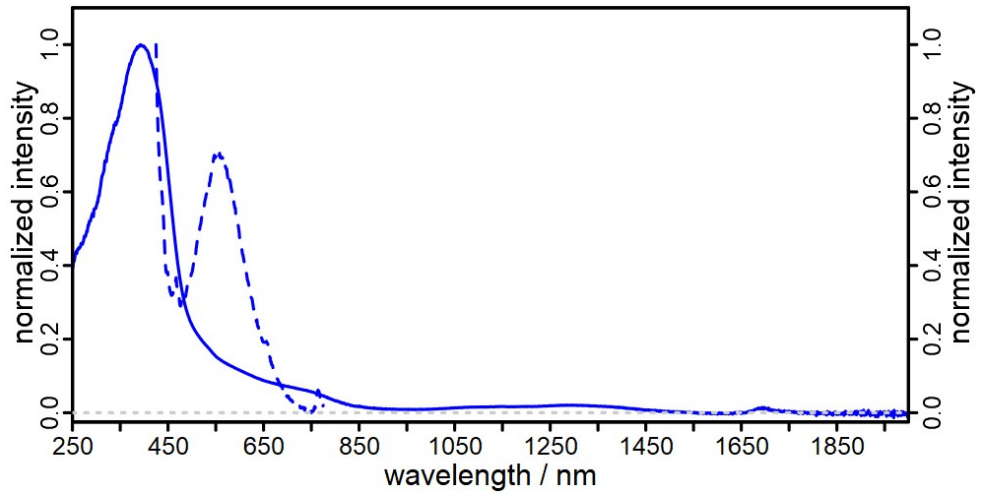

Figure S55: Normalised solid-state steady-state absorption *vs.* KBr (solid) and uncorrected emission ($\lambda_{exc.}$ = 400 nm, dotted) of **8**.

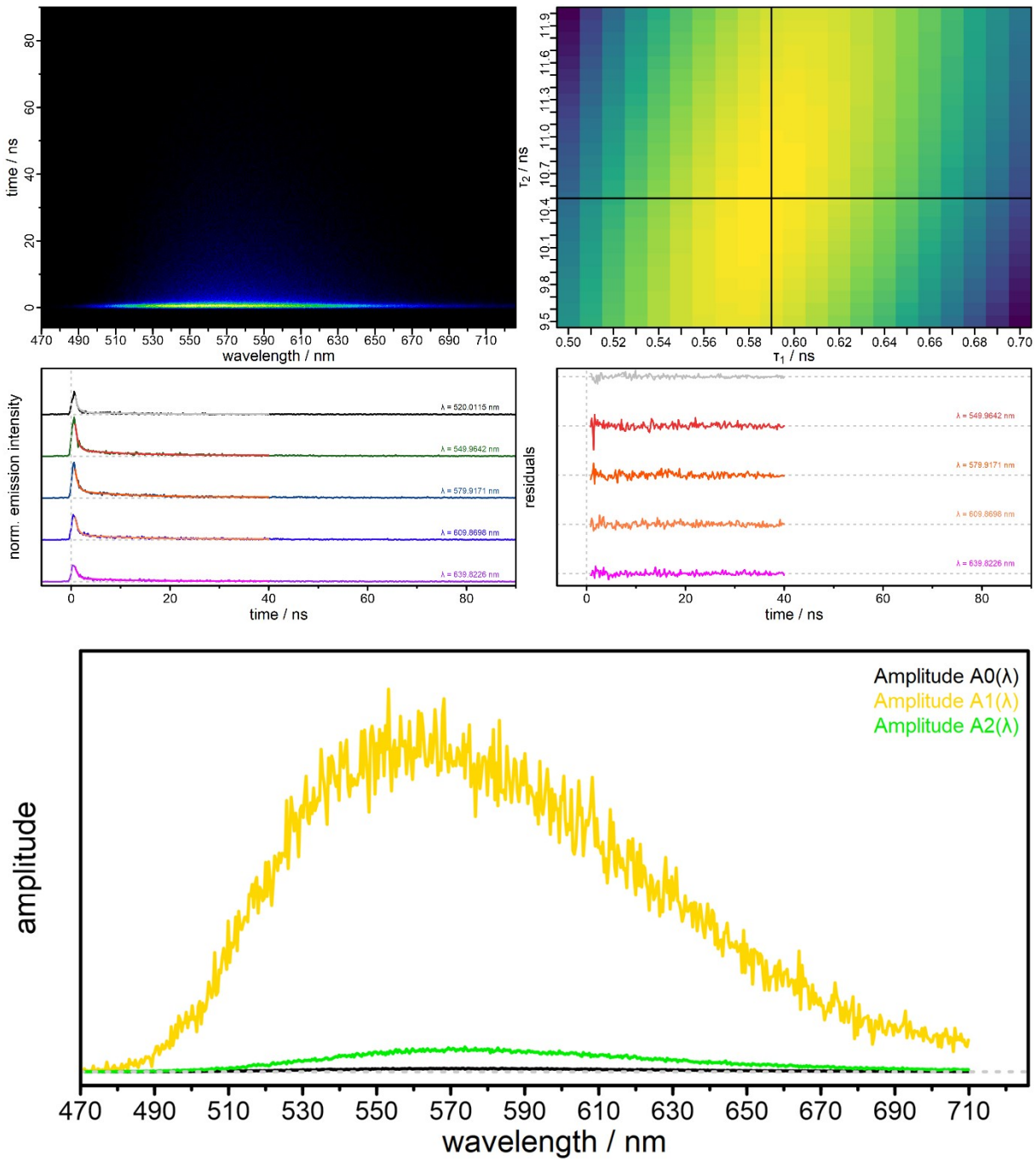

Figure S56: Time-resolved measurement ($\lambda_{exc.}$ = 400 nm) of the KBr solid-state luminescence of **8** showing the streak image (top left), the residual sum of squares summed up over the fitted wavelengths (top right), yellow lowest and purple highest. Selected kinetics (middle left, offset for visual clarity) with biexponential decays and the residuals of the fits with lowest residual sum of squares (middle right, offset for visual clarity). The biexponential fit has the following lifetimes: τ_1 = 0.59 ns and τ_2 = 10.5 ns. The decay-associated spectrum (bottom) shows the amplitude distribution of the lifetimes at each wavelength. The DAS of τ_1 shows a peak at 563.4 nm and the DAS for τ_2 at 573.8 nm.

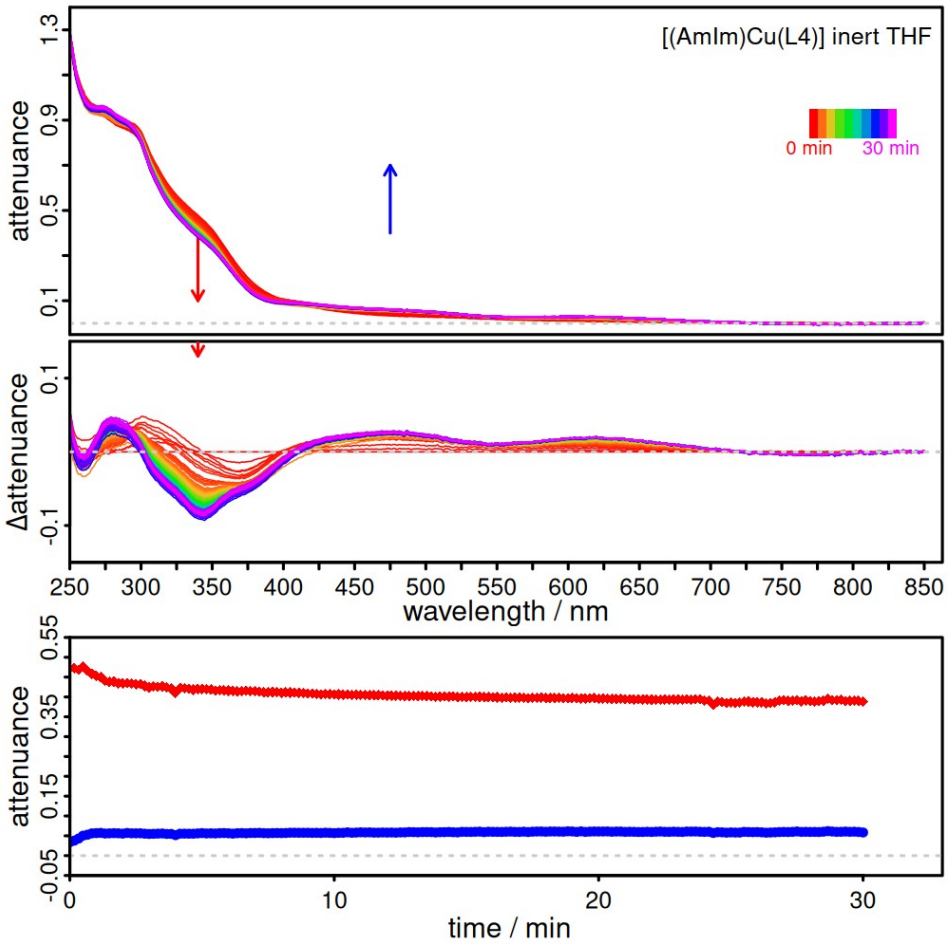

Figure S57: Steady-state absorption of **9** in inert tetrahydrofuran over time. The spectrum (top) over time and its associated spectral changes (middle) are shown. Kinetics (bottom) at 340 nm (red) and 475 nm (blue) are shown.

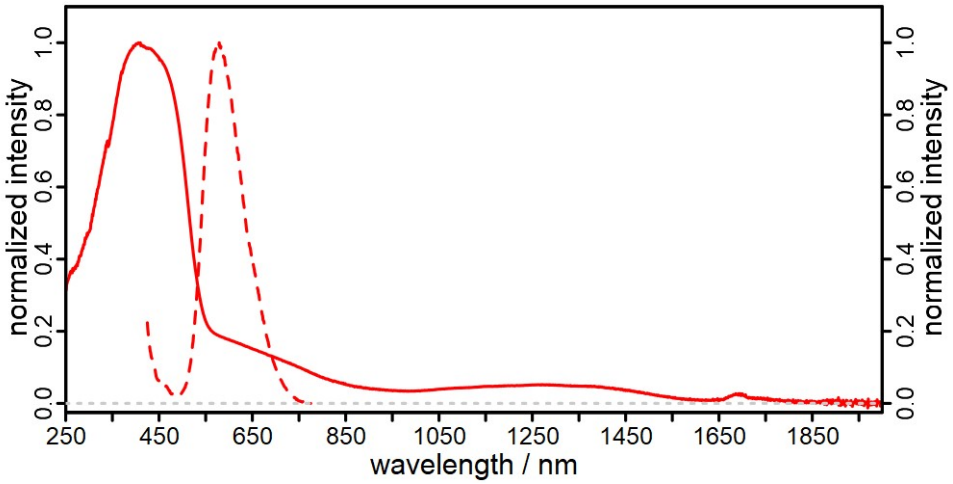

Figure S58: Solid-state steady-state absorption (solid) and uncorrected emission ($\lambda_{exc.}$ = 400 nm, dashed) of **9**.

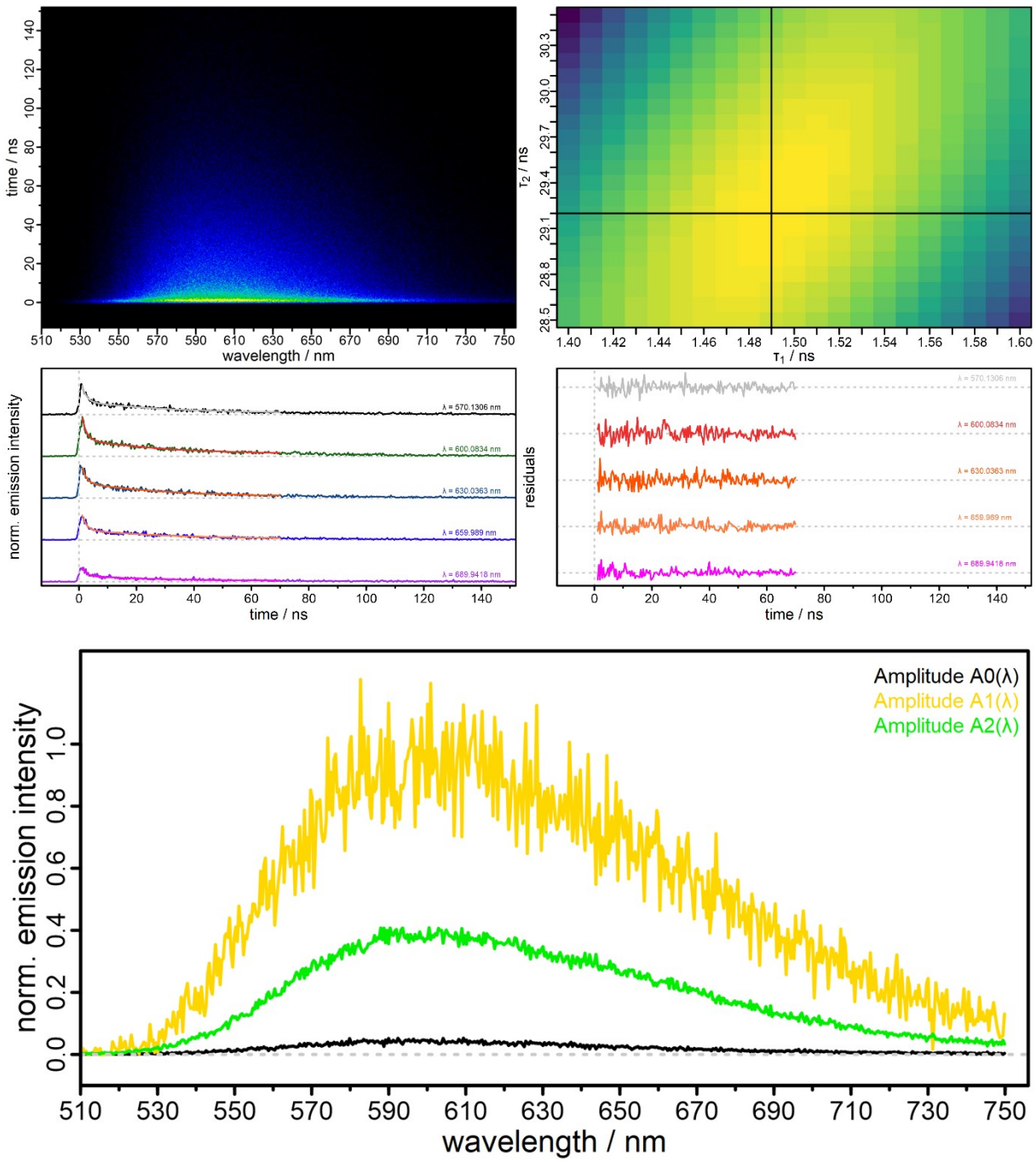

Figure S59: Time-resolved measurement ($\lambda_{exc.}$ = 400 nm) of the KBr solid-state luminescence of **9** showing the streak image (top left), the residual sum of squares summed up over the fitted wavelengths (top right), yellow lowest and purple highest. Selected kinetics (middle left, offset for visual clarity) with biexponential decays and the residuals of the fits with lowest residual sum of squares (middle right, offset for visual clarity). The biexponential fit has the following lifetimes: τ_1 = 1.49 ns and τ_2 = 29.2 ns. The decay-associated spectrum (bottom) shows the amplitude distribution of the lifetimes at each wavelength. The DAS of τ_1 shows a peak at 607.1 nm and the DAS for τ_2 at 602.5 nm.

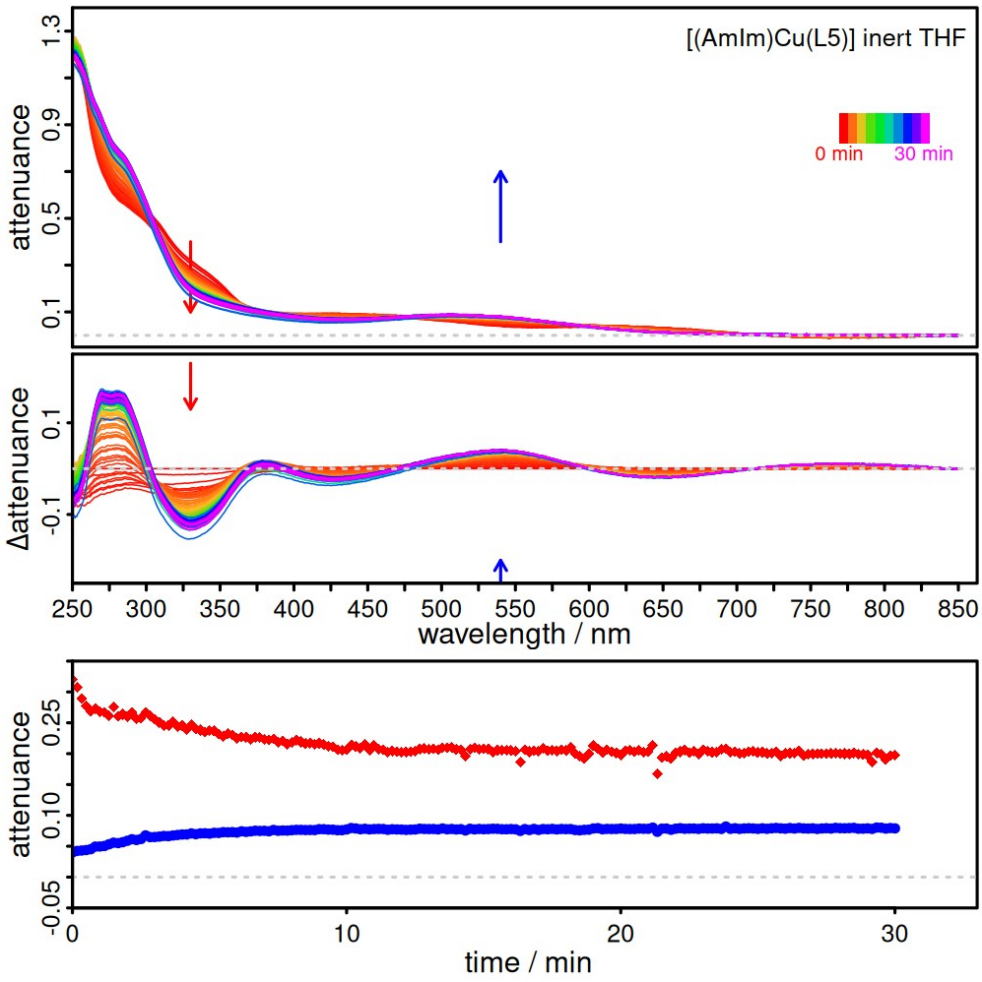

Figure S60: Steady-state absorption of **10** in inert tetrahydrofuran over time. The spectrum (top) over time and its associated spectral changes (middle) are shown. Kinetics (bottom) at 330 nm (red) and 540 nm (blue) are shown.

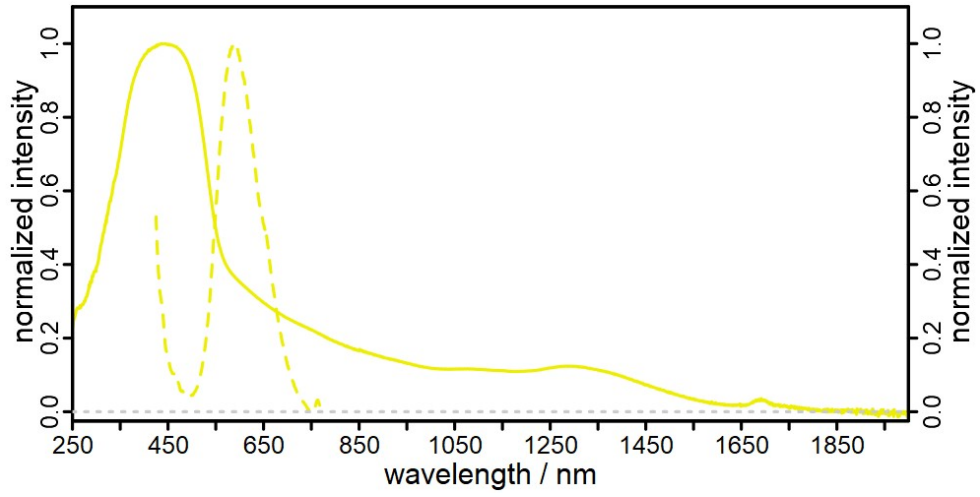

Figure S61: Solid-state steady-state absorption (solid) and uncorrected emission ($\lambda_{exc.}$ = 400 nm, dashed) of **10**.

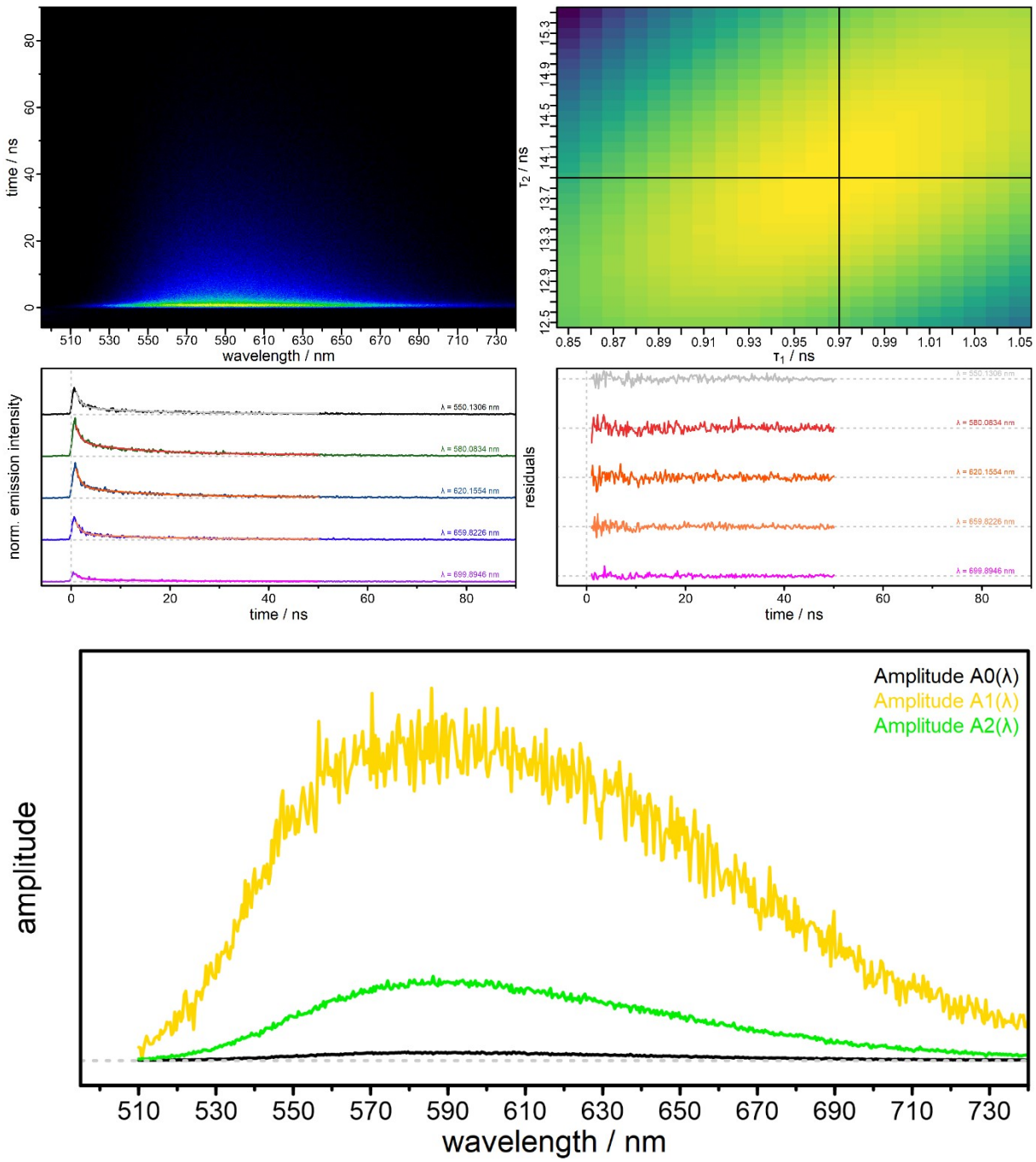

Figure S62: Time-resolved measurement ($\lambda_{exc.}$ = 400 nm) of the KBr solid-state luminescence of **10** showing the streak image (top left), the residual sum of squares summed up over the fitted wavelengths (top right), yellow lowest and purple highest. Selected kinetics (middle left, offset for visual clarity) with biexponential decays and the residuals of the fits with lowest residual sum of squares (middle right, offset for visual clarity). The biexponential fit has the following lifetimes: τ_1 = 0.97 ns and τ_2 = 13.9 ns. The decay-associated spectrum (bottom) shows the amplitude distribution of the lifetimes at each wavelength. The DAS of τ_1 shows a peak at 591.7 nm and the DAS for τ_2 at 591.9 nm.

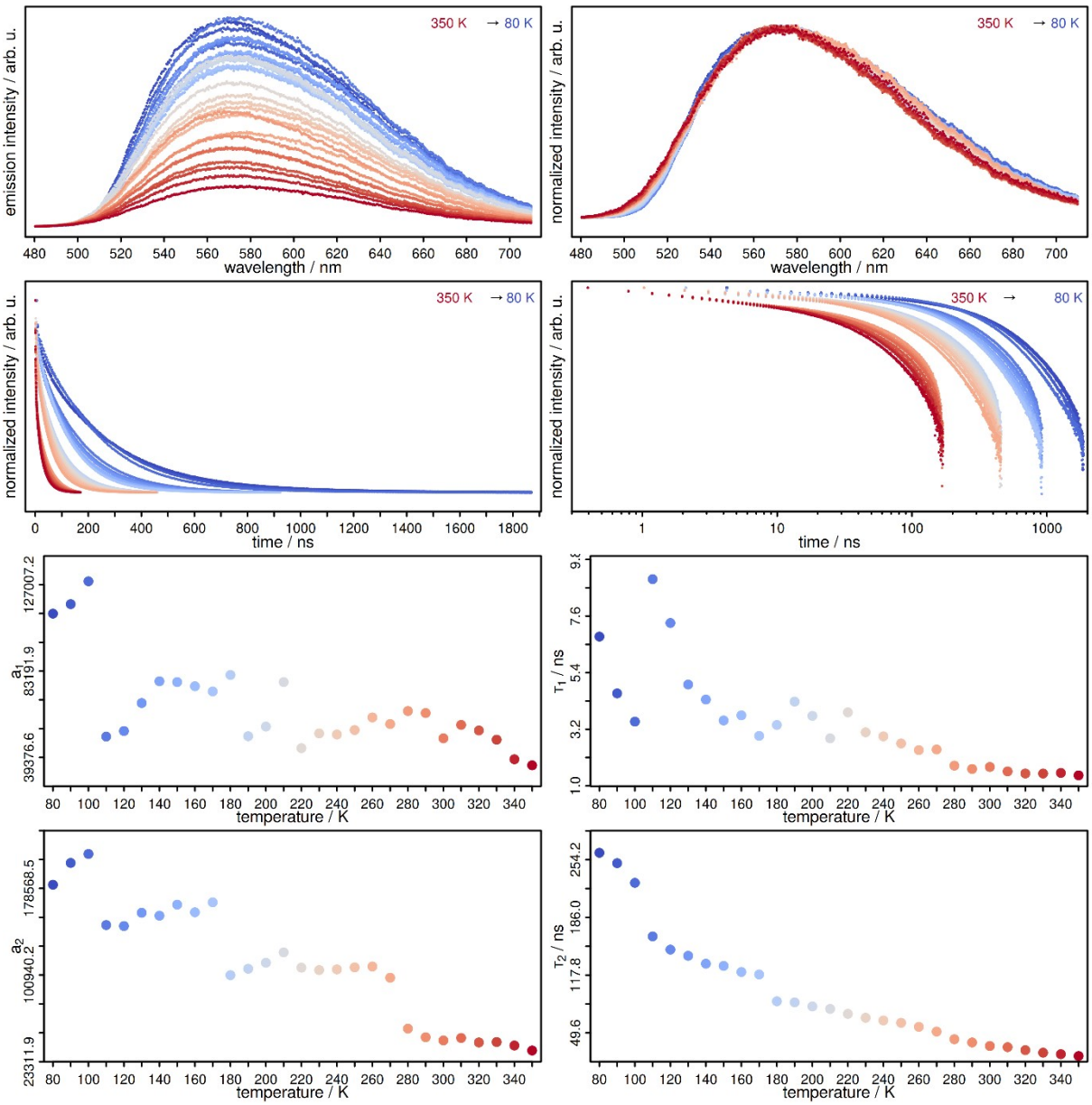

Figure S63: Temperature-dependent time-resolved emission measurement of **9**. The top row shows the emission spectrum with decreasing temperature (left) and normalised (right). The second row shows the normalised emission intensity vs. time linearly (left) and in a double logarithm plot (right). The third and fourth row show the trajectory of the amplitudes (left) and lifetimes (right) versus temperature. Component 1 is almost temperature-independent whereas component 2 becomes more intense (amplitude) and longer-lived (lifetime). The discontinuities inbetween some of the fits is an artifact from changing the time window length.

6. Electrochemistry

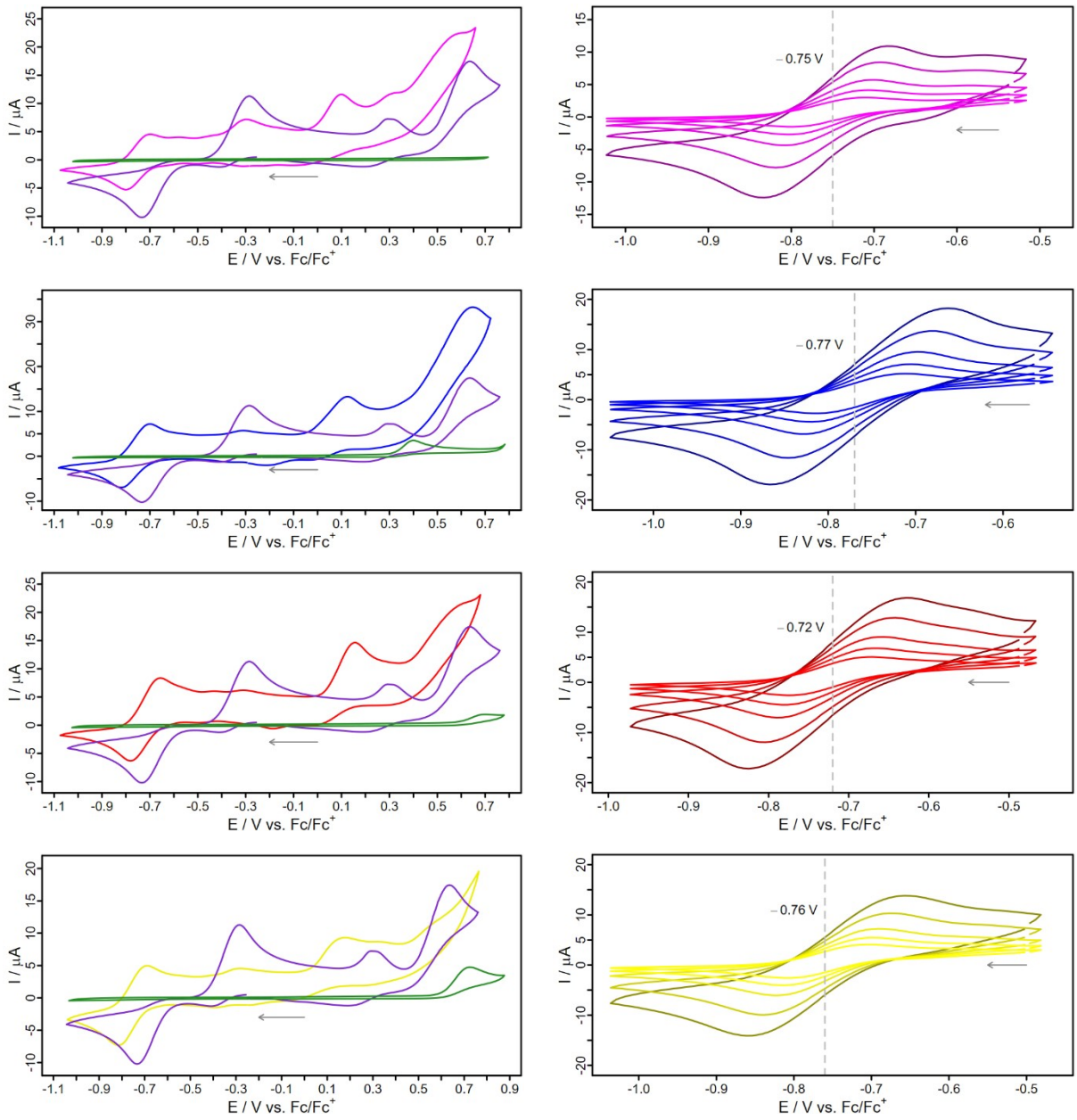

Figure S64: Left: Full cyclic voltammograms of **7** (1st row, magenta), **8** (2nd row, blue), **9** (3rd row, red) and **10** (4th row, yellow) including the respective phosphine ligands **L2** (1st row, green), **L3** (2nd row, green), **L4** (3rd row, green) and **L5** (4th row, green) and the HAmIm ligand (purple). Right: First reduction events of the complexes **7**, **8**, **9** and **10** (top to bottom) determined with scan rates of 0.5, 0.25, 0.1, 0.05 and 0.025 V/s (dark to light colour).

7. References

References

1 N. Kuhn and T. Kratz, Synthesis of Imidazol-2-ylidenes by Reduction of Imidazole-2(3 H)-thiones, *Synthesis*, 1993, 561–562.

2 R. A. Kunetskiy, L. Císařová, D. Šaman and L. M. Lyapkalo, New Lipophilic 2-Amino-N,N'-dialkyl-4,5-dimethylimidazolium Cations: Synthesis, Structure, Properties, and Outstanding Thermal Stability in Alkaline Media, *Chem. Eur. J.*, 2009, **15**, 9477–9485.

3 L. Denker, B. Trzaskowski and R. Frank, "Give me five" - an amino imidazoline-2-imine ligand stabilises the first neutral five-membered cyclic triel(I) carbenoides, *Chem. Comm.*, 2021, **57**, 2816–2819.

4 L. Denker, D. Wullschläger, J. P. Martínez, S. Świerczewski, B. Trzaskowski, M. Tamm and R. Frank, Cobalt(I)-Catalyzed Transformation of Si–H Bonds: H/D Exchange in Hydrosilanes and Hydrosilylation of Olefins, *ACS Catal.*, 2023, **13**, 2586–2600.

5 R. Robinson and P. R. Sharp, Syntheses, Structures, and Reductive Elimination Studies of Six-Membered Diaryl Platinacycle Complexes, *Organometallics*, 2010, **29**, 1388–1395.

6 D. Dodds, M. Boele, G. van Strijdonck, J. de Vries, P. van Leeuwen and P. Kamer, Design, Testing and Kinetic Analysis of Bulky Monodentate Phosphorus Ligands in the Mizoroki–Heck Reaction, *Eur. J. Inorg. Chem.*, 2012, **2012**, 1660–1671.

7 A. Oukhrib, L. Bonnafoux, A. Panossian, S. Waifang, D. H. Nguyen, M. Urrutigoity, F. Colobert, M. Gouygou and F. R. Leroux, Novel C1-symmetric dibenzophosphole ligands: application in hydroformylation reactions, *Tetrahedron*, 2014, **70**, 1431–1436.

8 F. Neese, Software update: The ORCA program system—Version 5.0, *WIREs Comput. Mol. Sci.*, 2022, **12**.

9 C. Adamo and V. Barone, Toward reliable density functional methods without adjustable parameters: The PBE0 model, *J. Chem. Phys.*, 1999, **110**, 6158–6170.

10 F. Weigend and R. Ahlrichs, Balanced basis sets of split valence, triple zeta valence and quadruple zeta valence quality for H to Rn: Design and assessment of accuracy, *Phys. Chem. Chem. Phys.*, 2005, **7**, 3297–3305.

11 E. Caldeweyher, C. Bannwarth and S. Grimme, Extension of the D3 dispersion coefficient model, *J. Chem. Phys.*, 2017, **147**, 34112.

12 E. Caldeweyher, S. Ehlert, A. Hansen, H. Neugebauer, S. Spicher, C. Bannwarth and S. Grimme, A generally applicable atomic-charge dependent London dispersion correction, *J. Chem. Phys.*, 2019, **150**, 154122.

13 F. Neese, An improvement of the resolution of the identity approximation for the formation of the Coulomb matrix, *J. Comput. Chem.*, 2003, **24**, 1740–1747.

14 F. Neese, F. Wennmohs, A. Hansen and U. Becker, Efficient, approximate and parallel Hartree–Fock and hybrid DFT calculations. A 'chain-of-spheres' algorithm for the Hartree–Fock exchange, *Chem. Phys.*, 2009, **356**, 98–109.

15 R. Izsák and F. Neese, An overlap fitted chain of spheres exchange method, *J. Chem. Phys.*, 2011, **135**, 144105.

16 B. Helmich-Paris, B. de Souza, F. Neese and R. Izsák, An improved chain of spheres for exchange algorithm, *J. Chem. Phys.*, 2021, **155**, 104109.
17 F. Weigend, Accurate Coulomb-fitting basis sets for H to Rn, *Phys. Chem. Chem. Phys.*, 2006, **8**, 1057–1065.
18 M. Garcia-Ratés and F. Neese, Effect of the Solute Cavity on the Solvation Energy and its Derivatives within the Framework of the Gaussian Charge Scheme, *J. Comput. Chem.*, 2020, **41**, 922–939.
19 F. Neese and G. Olbrich, Efficient use of the resolution of the identity approximation in time-dependent density functional calculations with hybrid density functionals, *Chem. Phys. Lett.*, 2002, **362**, 170–178.
20 T. Petrenko, S. Kossmann and F. Neese, Efficient time-dependent density functional theory approximations for hybrid density functionals: analytical gradients and parallelization, *J. Chem. Phys.*, 2011, **134**, 54116.
21 E. C. Meng, T. D. Goddard, E. F. Pettersen, G. S. Couch, Z. J. Pearson, J. H. Morris and T. E. Ferrin, UCSF ChimeraX: Tools for structure building and analysis, *Protein Sci.*, 2023, **32**, e4792.
22 E. F. Pettersen, T. D. Goddard, C. C. Huang, E. C. Meng, G. S. Couch, T. I. Croll, J. H. Morris and T. E. Ferrin, UCSF ChimeraX: Structure visualization for researchers, educators, and developers, *Protein Sci.*, 2021, **30**, 70–82.
23 T. D. Goddard, C. C. Huang, E. C. Meng, E. F. Pettersen, G. S. Couch, J. H. Morris and T. E. Ferrin, UCSF ChimeraX: Meeting modern challenges in visualization and analysis, *Protein Sci.*, 2018, **27**, 14–25.
24 A. J. Schaefer, V. M. Ingman and S. E. Wheeler, SEQCROW: A ChimeraX bundle to facilitate quantum chemical applications to complex molecular systems, *J. Comput. Chem.*, 2021, **42**, 1750–1754.
25 V. M. Ingman, A. J. Schaefer, L. R. Andreola and S. E. Wheeler, QChASM : Quantum chemistry automation and structure manipulation, *WIREs Comput. Mol. Sci.*, 2021, **11**.
26 M. Hesse, H. Meier and B. Zeeh, *Spektroskopische Methoden in der organischen Chemie*, Thieme, Stuttgart, 7th edn., 2005.
27 Rigaku Oxford Diffraction, *"CrysAlisPRO Softw. Syst. version 1.171.3846"*, Rigaku, 2018.
28 G. M. Sheldrick, SHELXT - integrated space-group and crystal-structure determination, *Acta Cryst.*, 2015, **A71**, 3–8.
29 G. M. Sheldrick, A short history of SHELX, *Acta Cryst. Section A, Found. of Crystallogr.*, 2008, **64**, 112–122.
30 O. V. Dolomanov, L. J. Bourhis, R. J. Gildea, J. A. K. Howard and H. Puschmann, OLEX2 : a complete structure solution, refinement and analysis program, *J Appl Crystallogr*, 2009, **42**, 339–341.
31 A. L. Spek, Structure validation in chemical crystallography, *Acta Cryst*, 2009, **65**, 148–155.